UNIVERSITY OF CALIFORNIA

Los Angeles

# Three-Dimensional Structures at Atomic Resolution: Electron Tomography

A dissertation submitted in partial satisfaction of the requirements for the degree Doctor of Philosophy in Physics

by

Chien-Chun Chen

2013

ABSTRACT OF THE DISSERTATION

Three-Dimensional Structures at Atomic Resolution:

Electron Tomography

By

Chien-Chun Chen

Doctor of Philosophy in Physics

University of California, Los Angeles, 2013

Professor Jianwei Miao, Chair

Electron microscopy has found wide application in material science and biology with the nanometer / angstrom resolution in planar images. Tomography has also made a revolutionary impact of non-destructively visualizing inner three-dimensional structures, especially in the field of clinical medical imaging. Digital signal processing is used in a broad range of electrical engineering to separate the signal from the noise; hence extracting true information embedded from the noisy data. In the past century, imperfections inside the crystalline structures have caught material scientists' eyes due to the capability of significantly changing physical properties of materials. In this dissertation, a remarkable stride in the field of electron tomography has been made by combining several novel techniques: scanning transmission electron microscopy to obtain high resolution two-dimensional images, the

center of mass alignment method to solve the mis-alignment problem, the equally sloped tomography method to achieve best spatial resolution by dramatically alleviating the missing wedge problem, and the three-dimensional Fourier filtering method to enhance the signal-to-noise ratio. With these combinations, a 2.4 angstrom resolution in the tomographic reconstruction is demonstrated. Furthermore, atomic steps at the boundary between two grains, edge dislocations, and screw dislocations inside a 10nm platinum particle are observed, atom-by-atom.

The dissertation of Chien-Chun Chen is approved.

Tomas G. Mason

Brian C. Regan

Yu Huang

Jianwei Miao, Committee Chair

University of California, Los Angeles

2013

TABLE OF CONTENTS

LIST OF FIGURES AND TABLES

ACKNOWLEDGEMENTS

For the four years of my studying at UCLA, it was the best of my time because I learnt and completed a lot in both academic and personal life. Undoubtedly, my advisor, Prof. Jianwei Miao, who I deeply appreciate, is the most important person during these years. With his support, guidance, and mentorship, I not only learnt useful theoretical and experimental skills, but also learnt the attitude of doing research and the instruction of publishing top journals, which I think are precious and rare to most graduate students. I will cherish the memory with my advisor and outstanding committee members, Prof. Mason, Prof. Regan, and Prof. Huang, who generously provided their valuable suggestions and collaborations.

Chapter 2 is a published paper in *Nature*. I would like to thank the co-authors for their contributions: M. C. Scott, M. Mecklenburg, C. Zhu, R. Xu, P. Ercius, U. Dahmen, B. C. Regan, and J. Miao.

Chapter 3 is my second published paper in *Nature*. I would like to thank the co-authors for their contributions: C. Zhu, E. R. White, C. -Y. Chiu, M. C. Scott, B. C. Regan, L. D. Marks, Y. Huang, and J. Miao.

Chapter 4 is a published paper in *Phys. Rev. B*. I would like to thank the co-authors for their contributions: H. Jiang, L. Rong, S. Salha, R. Xu, T. G. Mason and J. Miao.

I would like to dedicate this dissertation to my parents and thank them for their long-term support, especially for their understanding of reluctantly parting from their only son. Finally,

I would like to thank my wife, Yi-Hsuan Lee, who always company with me and encourage me when I undergo disappointment and failure before experiencing success.

# VITA

| | |
|---|---|
| 2009 - 2013 | Graduate Student Researcher<br>Department of Physics and Astronomy<br>University of California, Los Angeles |
| 2004 - 2013 | Visiting Scientist<br>RIKEN (Institute of Physics and Chemical Research)<br>Hyogo, Japan |
| 2004 - 2009 | Research Assistant<br>Academia Sinica (Institute of Physics)<br>Taipei, Taiwan |
| 2000 - 2003 | Master of Science in Physics<br>Nation Taiwan University<br>Taipei, Taiwan |
| 1996 - 2000 | Bachelor of Science in Physics<br>National Taiwan University<br>Taipei, Taiwan |

## PUBLICATIONS AND PRESENTATIONS

Publications

1. H. Jiang, R. Xu, **C. -C. Chen**, W. Yang, J. Fan, X. Tao, C. Song, Y. Kohmura, T. Xiao, Y. Wang, Y. Fei, T. Ishikawa, W. L. Mao, and J. Miao, "Three-dimensional coherent x-ray diffraction imaging of molten iron in mantle olivine at nanoscale resolution", *Phys. Rev. Lett.* 110, 205501 (2013)
2. **C. -C. Chen**, C. Zhu, E. R. White, C. -Y. Chiu, M. C. Scott, B. C. Regan, L. D. Marks, Y. Huang, and J. Miao, "Three- dimensional imaging of dislocations in nanoparticles at atomic resolution", *Nature*, 496, 74-77 (2013).

   [ Highlighted by *Nature* News&Views,"3D imaging of crystal defects", *Nature*, 496, 37-38 (2013) ]

   [ Featured Video by Nature Video Channel, "Have you ever seen an atom?" ]
3. J. A. Rodriguez, R. Xu, **C. -C. Chen**, Y. Zhou, and J. Miao, "Oversampling smoothness (OSS): an effective algorithm for phase retrieval of noisy diffraction intensities", *J. Appl. Cryst*., 46, 312-318 (2013).
4. **C. -C. Chen**, H. Jiang, L. Rong, S. Salha, R. Xu, T. G. Mason and J. Miao, "Reply to Comment on 'Three-dimensional imaging of a phase object from a single sample orientation using an optical laser'", *Phys. Rev. B*, 86, 226102 (2012).
5. M. C. Scott*, **C. -C. Chen***, M. Mecklenburg*, C. Zhu, R. Xu, P. Ercius, U. Dahmen, B. C. Regan & J. Miao, "Electron tomography at 2.4-angstrom resolution", *Nature*, 483, 444-447 (2012). (*Co-first authors)

   [ Highlighted in *Nature Nanotech*. 7, 275 (2012) ]

6. **C. -C. Chen**, H. Jiang, L. Rong, S. Salha, R. Xu, T. G. Mason and J. Miao, "Three-dimensional imaging of a phase object from a single sample orientation using an optical laser", *Phys. Rev. B*, 84, 224104 (2011).

7. M. D. Seaberg, D. E. Adams, E. L. Townsend, D. A. Raymondson, W. F. Schlotter, Y. Liu, C. S. Menoni, L. Rong, **C. -C. Chen**, J. Miao, H. C. Kapteyn and M. M. Murnane. "Ultrahigh 22 nm resolution coherent diffractive imaging using a desktop 13 nm high harmonic source", *Opt. Express* 19, 22470-22479 (2011).

8. **C. -C. Chen**, C.-H. Lu, D. Chien, J. Miao and T.K. Lee, "Three-dimensional Image Reconstruction of Radiation-Sensitive Samples with X-ray Diffraction Microscopy", *Phys. Rev. B*, 84, 024112 (2011).

9. R. Xu, S. Salha, K. S. Raines, H. Jiang, **C. -C. Chen**, Y. Takahashi, Y. Kohmura, Y. Nishino, C. Song, T. Ishikawa, J. Miao, "Coherent Diffraction Microscopy at SPring-8: Instrumentation, Data Acquisition and Data Analysis", *J. Synch. Rad.* 18, 293-298 (2011).

10. H. Jiang, C. Song, **C. -C. Chen**, R. Xu, K. S. Raines, B. P. Fahimian, C.-H.Lu, T. K. Lee, A. Nakashima, J. Urano, T. Ishikawa, F. Tamanoi, and J. Miao, "Quantitative 3D Imaging of Whole, Unstained Cells by Using X-ray Diffraction Microscopy", *Proc. Natl. Acad. Sci. USA* 107, 11234-11239 (2010).

11. **C. -C. Chen**, J. Miao and T. K. Lee, "Tomographic Image Alignment in 3D Coherent Diffraction Microscopy", *Phys. Rev. B*. 79, 052102 (2009).

12. **C. -C. Chen**, J. Miao, C.W. Wang, and T.K. Lee, “Application of the optimization technique to non-crystalline X-ray diffraction microscopy - Guided Hybrid Input-Output Method (GHIO)”, *Phys. Rev. B*. 76, 064113 (2007).

13. C. Song, D. Ramunno-Johnson, Y. Nishino, Y. Kohmura, T. Ishikawa, **C. -C. Chen**, T.K. Lee and J. Miao, "Phase Retrieval from Exactly Oversampled Diffraction Intensity Through Deconvolution", *Phys. Rev. B*. 75, 012102 (2007).

14. J. Miao**, C. -C. Chen**, C. Song, Y. Nishino, Y. Kohmura, T. Ishikawa, D. Ramunno-Johnson, T.K. Lee and S.H. Risbud, "Three-Dimensional GaN-Ga2O3 Core Shell Structure Revealed by X-ray Diffraction Microscopy", *Phys. Rev. Lett*. 97, 215503 (2006).

15. C. Zhu, **C. -C. Chen**, J. Du, M. R. Sawaya, M. C. Scott, P. Ercius, J. W. Ciston, and J. Miao, "Towards 3D Structural Determination of Amorphous Materials at Atomic Resolution", *Phys. Rev. Lett.* (under review)

Presentations

1. "Three-Dimensional imaging of dislocations in a nanoparticle at atomic resolution", Biophysics seminar, University of California, Los Angeles, U.S.A., Apr. 19, 2013.

2. "Approach Atomic Resolution in 3D structures: Electron Tomography", National Central University, Taiwan, Feb. 21, 2013. (*invited*)

3. "Novel 3D reconstruction techniques from limited views: Equally Sloped Tomography and Ankylography",5th International Workshop on FEL Science, Gyeongju, Korea, Oct. 28 - Nov. 1, 2012. (*invited*)

# CHAPTER 1

## Introduction to Electron Tomography

As pointed out in Richard P. Feynman's classic speech, "There is plenty of room at the bottom" [1], he said "It would be very easy to make an analysis of any complicated chemical substance; all one would have to do would be to look at it and see where the atoms are.". Seeing atoms in three-dimensional structures has become an extremely important problem and a long term dream in science. Once atoms can be directly revealed in three-dimensional structures, the rough atomic positions can be input as the initial model in the theoretical ab-initial calculation, thus simulating and understanding the properties and the mechanisms of all kinds of materials.

To date, even with significant advancements of all other novel imaging techniques [2-8], crystallography still plays the unique role to peer into three-dimensional structures at an atomic scale [9]. With intense and coherent x-ray sources from synchrotron radiation facilities illuminating on the millimeter- or micrometer-sized crystalline samples, the Bragg peaks, formed by interference of scattered photons from millions or thousands periodic unit cells, provide scientists with meaningful information to calculate the corresponding arrangements of atoms [10,11]. Under the assumption that periodic unit cells are all identical, an averaged atomic model from those copies is able to be extracted from the macro-measured data.

However, a solved averaged model with atom position doesn't mean the atomic resolution is indeed achieved. For example, a prototype of a human can be obtained by averaging millions of persons. Even the position of each tooth can be mapped by the model of a human, the imperfections, such as some individuals lost their teeth, will never be observed in this human model. It is for sure that small imperfections may cause some diseases or malfunctions in a human's body, and interestingly, the micro-world has the same scenario. Although valuable information regarding lattice parameters inside the crystal can be obtained from crystallography, the crystal imperfections, so called the defects, turn out to be much more attractive to material scientists with the capability of dramatically changing the physical properties of materials.

To investigate defects inside the perfect crystal, using beams of electrons becomes a better choice than photons due to the intrinsic difference that the scattering cross-section of an electron is much larger than a photon. With a much stronger interaction by an electron source, it would be possible to obtain enough signals to retrieve individual atoms. Recent advancements in imaging techniques via electron sources has verified this possibility [12]. Through scanning electron microscopy (SEM) and transmission electron microscopy (TEM), scientists demonstrate the atomic resolution of both surface and projection in two-dimensional images. Moreover, the atomic arrangement at interfaces between grains of a single layer graphene unraveled through a scanning transmission electron microscope (STEM) shows the astonishing power of the electron microscope [13].

There is no doubt that the electron microscope provides amazingly detailed information of the most fundamental scale; however, three-dimensional atomic resolution is still not achievable. Instead of using a two-dimensional image to infer the inner three-dimensional structures, performing computed tomography (CT) from several two-

dimensional projections is definitely a better approach to obtain correct three-dimensional information.

Tomography [14-18] has found its widespread applications in seeing inner structures non-destructively and also has a distinguished history during the past half century, especially in the clinical medical imaging. As the first x-ray computed tomography machine was built in 1961 [19] , numbers of famous reconstruction methods such as filtered back-projection (FBP) [20] , algebraic reconstruction technique (ART) [21,22], and simultaneous iterative reconstructive technique (SIRT) [14] have been developed and worked successfully in the field of medical imaging. The problem remains unsolved in the field of electron tomography and even scientists have applied those reconstruction methods since 1968; therefore, performing tomographic reconstruction at the atomic resolution has been proven to be a challenge [23-25].

In contrast to medical computed tomography, the main difference of electron tomography is the limited number of projections. It should be noted that the number of projections is proportional to the resolution desired. Different sample size such as, looking into organs or tumors in the human body, locating atoms needs a much smaller (*i.e.,* nanometer-sized) sample. The reason for not using a larger sample size is that the number of atoms included inside a nanometer particle can be estimated over several tens of thousands. When the sample is larger, too many atoms may significantly increase the complexity of locating atoms. Furthermore, because of the multiple scattering effect from a thick sample, the non-linearity of the projection may result in lots of artifacts when performing tomographic reconstruction. Under the constraint of the small-sized sample, when the high energy electron source ( 80~300 keV ) is used to achieve the atomic resolution, the sample

would be destroyed by a high dose of electrons. As a result of radiation damage, the number of projection turns out to be only a few.

Due to the fact that the number of projections is limited, the following issues of data analysis and reconstruction are three-fold: the alignment problem, the interpolation problem, and the missing wedge problem.

First, in order to keep the selected sample always inside the field of view during data acquisition, experimentalists manually rotate the sample holder, shift the stage and take projections. Those projections consequently do not correspond to the same rotation axis. Although finding the exact rotation axis is theoretically not necessary, aligning all projections to an unique common rotation axis is required to perform the correct reconstruction. Since the nearby projections with small angular increments should be similar, scientists usually align neighboring projections to the common rotation axis by using the cross-correlation method. Nevertheless, as the limited number of projections mentioned above, the angular increment between two nearby projections is no longer small, and thus the relation of similarity does not hold any more. Some numerical tests have been done to simulate the effect of misalignment from the cross-correlation method when the angular increment is large. The banana-shaped distortions in the reconstruction caused by this kind of misalignment is studied. The reason for this shape of distortion is that the accumulated errors from sequentially using cross-correlation method to align nearby projections [29].

Second, the acquired projections are digital two-dimensional images formed by pixels so that the distribution of all data points can be considered as grid points in the cylindrical coordinate. Unlike the data points on the cylindrical grids, the three-dimensional reconstruction is on Cartesian grids, thus giving another problem, the interpolation problem

from polar grids to Cartesian grids. Usually, the interpolation might be a small factor in the reconstruction process, the number of projections being large and the corresponding angular difference being small. Conversely, especially in electron tomography, the limited projections cause much larger errors, and unfortunately, those errors may deteriorate the reconstruction and prohibit scientists from revealing three-dimensional structures at high resolution.

Third, a more severe problem exists because of the experimental setup, the data set is incomplete. For the single tilted data set, the incident electron beam is blocked by the sample holder when the rotation angle goes higher than 75 degrees. Although more advanced instruments may be rotated up to 80 degrees, it is not avoidable to have some angles lost. As the sample is supported by the membrane, the thickness of the membrane becomes much thicker at higher angles such that the background of the acquired image from the thick membrane is much more severe compared to low angles. This effect will deteriorate the quality of taken images, especially the resolution. One would observe this effect by Fourier transferring the projections to reciprocal space and observing the Bragg peaks become weaker and weaker, which indicates that the resolution is increasingly worse.

Even if one could solve the three issues mentioned above and obtain the correct reconstruction, the signal from single atom is extremely weak and the signal-to-noise ratio (SNR) of the reconstruction is still too low to reveal individual atoms. If one can not see individual atoms to figure out three-dimensional structures inside the sample, then it becomes impossible to make meaningful measurements.

A recent technique, atom probe tomography, uses a needle-shaped sample and provides a path to overcome the missing wedge problem. Due to the low signal-to-noise ratio, only ~60% atom can be detected and visualizing embedded structures at an atomic

resolution is still not possible [26]. Another novel approach called discrete tomography [27] based on the assumption that the inner structure is a perfect single crystal, provides the resolution to unveil all atoms inside the sample, while a perfect crystal is less informative to material scientists. There is also an approach named big bang tomography [28]. By calculating the phases of electro-magnetic waves propagated at different two positions, the distance information between two single-layer graphene can be obtained. Those methods provide scientists new ways to see atoms under specific conditions; unfortunately, a general method is still needed to bypass all those conditions.

In this dissertation, a couple new imaging techniques [29-32] are developed to solve or dramatically alleviate major issues in data analysis, reconstruction, and signal-to-noise ratio: the center of mass alignment method (CM alignment), three-dimensional equally sloped tomography (3D EST), and three-dimensional Fourier filtering.

The center of mass alignment method is completely different from conventional alignment methods. In the parallel beam case, any arbitrary common rotation axis can be selected if that axis is parallel to the exact rotation axis. So that we can utilize the special geometry when the selected common rotation axis passes through the center of mass. Assuming the common rotation axis is on the center of mass, for each two-dimensional projection, the center of mass is always on the axis during whole rotation. If we selected the center of a two-dimensional image to be the origin and shift the image to make the calculated center of mass at the origin in every two-dimensional image, this special treatment of the image set corresponds exactly to the projection set with the rotation axis on both the origin and the center of mass; hence this special alignment can be easily done with high accuracy and without any accumulated errors from other projections. The feasibility of

this method is also verified by using the multislice simulation to generate projective images with 20% Poisson noise [30].

The second breakthrough is the 3D EST method. Based on the Fourier slice theorem, a projection in real space is mathematically equal to a slice in reciprocal space. If one could have enough number of slices to fulfill the reciprocal space, a three-dimensional reconstruction can be very easily obtained by applying inverse Fourier transform to the reciprocal space. The critical issues are the number of slices is limited and the interpolation from polar grids to Cartesian grids in reciprocal space is highly unreliable. Although there is no forward and backward fast Fourier transform between polar and Cartesian grids, a special Fourier transform called pseudopolar Fourier transform may convert grids between pseudopolar and Cartesian coordinates without any interpolation. The main features of pseudopolar grids are the grids form concentric squares and the angular distribution is equally sloped. To satisfy the special angular distribution, it is mandatory to take data at specific calculated angles followed by $\pm\tan^{-1}(n/N)$ and $\pm(\pi/2-\tan^{-1}(n/N))$ , where n is a positive integer and not larger than N. Once projections are acquired at equally sloped angles, the Fourier slices on pseudopolar grids can then be exactly calculated by the fractional Fourier transform. In addition, due to the limited number of projections, those Fourier slices are not sufficient to fulfill the reciprocal space so that the iterative algorithm is combined in the 3D EST method to refine the reconstruction using constraints in both real and reciprocal spaces. When the process converges, those missing slices, because of the limited number of slices and the missing wedge, are interpolated from all known information. This tomographic method has demonstrated its powerful ability of retrieving missing data not only in electron tomography but also in medical imaging, biological imaging, and coherent diffraction imaging [33-37]. Of cause the missing data problem can

not be completely solved, but the reconstruction obtained by 3D EST method has significantly alleviated the effect from the missing data.

The third breakthrough is the three-dimensional Fourier filtering. As a result that the signal from a single atom is very weak, applying a specific filter to separate the signal from the noise, thus extracting the useful information from the noisy data, is the most common way in digital signal processing. For the special case such as poly-crystalline samples, the Bragg peaks can be considered as the useful signals. Generating a three-dimensional filter that only keeps the distribution of Bragg peaks but removes all other irrelevant information in reciprocal space may have a great help to see atomic fringes. Although a two-dimensional Fourier filtering is well-known that generates artifacts in two-dimensional images, the three-dimensional Fourier filtering is studied that the filtered image has much higher accuracy regarding atom positions because three-dimensional Fourier filtering has more correlated information then two-dimensional [32].

Another part of this dissertation introduces a state-of-art reconstruction method, so called Ankylography [38,39] (derived from the Greek words ankylos meaning curved and graphein meaning writing), which allows scientists obtain three-dimensional structure from single two-dimensional diffraction pattern. This method is demonstrated in both theory and experiment with its capability of significantly reducing two-dimensional patterns needed. It is anticipated that that a wide application could be found with the radiation-sensitive samples.

# References


1. R. P. Feynman, "There's plenty of room at the bottom (data storage)", *Journal of Microelectromechanical Systems* **1**, 60–66 (1992) (A reprint of the talk).
2. L. Gross, F. Mohn, N. Moll, P. Liljeroth; G. Meyer, "The Chemical Structure of a Molecule Resolved by Atomic Force Microscopy", *Science* **325**, 1110–1114 (2009).
3. F. Christine, *et al.*, "Peeking into Pit Fields: A Multiple Twinning Model of Secondary Plasmodesmata Formation in Tobacco". *Plant Cell* **20**, 1504–18 (2008).
4. L. B. Rad, I. Downes, J. Ye, D. Adler, R. F. W. Pease, "Economic approximate models for backscattered electrons". *J. Vac. Sci. Technol. B* **25**, 2425 (2007).
5. R. V. Lapshin, "Feature-oriented scanning probe microscopy", *In H. S. Nalwa. Encyclopedia of Nanoscience and Nanotechnology* **14**. *USA: American Scientific Publishers.* 105–115 (2011).
6. G. Schitter, M. J. Rost, "Scanning probe microscopy at video-rate", *Materials Today* **11**, 40–48 (2008).
7. J. C. Meyer, C. O. Girit, M. F. Crommie, A. Zettl, (2008). "Imaging and dynamics of light atoms and molecules on graphene", *Nature* **454**, 319–22 (2008).
8. A. Amzallag, C. Vaillant, M. Jacob, M. Unser, J. Bednar, J. Kahn, J. Dubochet, A. Stasiak and A. J. H. Maddocks, "3D reconstruction and comparison of shapes of DNA minicircles observed by cryo-electron microscopy", *Nucleic Acids Research* **34**, e125 (2006).
9. J. C. Kendrew, G. Bodo, H. M. Dintzis, R. G. Parrish, H. Wyckoff, D. C. Phillips, "A three-dimensional model of the myoglobin molecule obtained by x-ray analysis", *Nature* **181**, 662–6 (1958).
10. H. P. Whitlock, *Am. Miner.* **3**, 92–98 (1918).

11. W. Friedrich, P. Knipping, and M. V. Laue, *Sitzungsber. Bayer. Akad. Wiss. München* 303–322 (1912).

12. S. Helveg, C. Lopez-Cartes, J. Sehested, P. L. Hansen, B. S. Clausen, "Atomic-scale imaging of carbon nanofibre growth", *Nature* **427**, 426–29 (2004).

13. P. Y. Huang, C. S. Ruiz-Vargas, A. M. van der Zande, W. S. Whitney, M. P. Levendorf, J. W. Kevek, S. Garg, J. S. Alden, C. J. Hustedt, Y, Zhu, J. Park, P. L. McEuen, and D. A. Muller, "Grains and Grain Boundaries in Single-Layer Graphene Atomic Patchwork Quilts", *Nature* **469***,* 389-392 (2011).

14. A. C. Kak and M. Slaney, *Principles of computerized tomographic imaging*, IEEE Press, New York, 1988.

15. J. Radon, "Uber die Bestimmung von Funktionen durch ihre Integralwerte Langs Gewisser Mannigfaltigkeiten". *Ber. Saechsische Akad. Wiss.* **29**, 262 (1917).

16. J. Radon, " On the determination of functions from their integrals along certain manifolds", *IEEE Trans. Med. Imaging.* **5**, 170–6 (1993).

17. H. Hornich, "A Tribute to Johann Radon", *IEEE Trans. Med. Imaging.* **5**, 169–9 (1986).

18. S. Kaczmarz, "Angenäherte Auflösung von Systemen linearer Gleichungen", *Bulletin International de l'Académie Polonaise des Sciences et des Lettres. Classe des Sciences Mathématiques et Naturelles. Série A, Sciences Mathématiques.* **35**, 355–7 (1937).

19. W. H. Oldendorf, :Isolated flying spot detection of radiodensity discontinuities – displaying the internal structural pattern of a complex object", *Ire Trans Biomed Electron*. **8**, 68–72 (1961).

20. S. R. Deans, "The Radon Transform and Some of Its Applications", *New York: John Wiley & Sons.* (1983)

21. R. Gordon, R. Bender, G. T. Herman, "Algebraic reconstruction techniques (ART) for three-dimensional electron microscopy and x-ray photography", *Journal of theoretical biology* **29**, 471–81 (1970).

22. F. Natterer, *The mathematics of computerized tomography* (1986)

23. W. Ludwig, *et al*, "Three-dimensional imaging of crystal defects by `topo-tomography'", *J. Appl. Crystallogr*. **34**, 602-607 (2001).

24. J. S. Barnard, J. Sharp, J. R. Tong, and P. A. Midgley, "High-Resolution Three-Dimensional Imaging of Dislocations", *Science* **313**, 319 (2006).

25. P. A. Midgley, and M. Weyland, "STEM Tomography", In *Scanning Transmission Electron Microscopy: Imaging and Analysis*. 353-392 (2011).

26. T. F. Kelly, and M. K. Miller, "Atom probe tomography", *Rev. Sci. Instrum*. **78**, 031101 (2007).

27. A. S. Van, K. J. Batenburg, M. D. Rossell, R. Erni, and T. G. Van, "Three-dimensional atomic imaging of crystalline nanoparticles", *Nature* **470**, 374–7 (2011).

28. D. V. Dyck, J. R. Jinschek and F.-R. Chen "`Big Bang' tomography as a new route to atomic-resolution electron tomography", *Nature* **486**, 243 (2012)

29. C. -C. Chen, J. Miao and T. K. Lee, "Tomographic Image Alignment in 3D Coherent Diffraction Microscopy", *Phys. Rev. B*. **79**, 052102 (2009)

30. M. C. Scott, C. -C. Chen, M. Mecklenburg, C. Zhu, R. Xu, P. Ercius, U. Dahmen, B. C. Regan, and J. Miao, "Electron tomography at 2.4-angstrom resolution", *Nature*, **483**, 444-447 (2012).

31. J. Miao, F. Frster, and O. Levi, "Equally Sloped Tomography with Oversampling Reconstruction", *Phys. Rev. B.* **72**, 052103 (2005).

32. C. -C. Chen, C. Zhu, E. R. White, C. -Y. Chiu, M. C. Scott, B. C. Regan, L. D. Marks, Y. Huang, and J. Miao, "Three- dimensional imaging of dislocations in nanoparticles at atomic resolution", *Nature* **496**, 74-77 (2013).

33. J. Miao, C. -C. Chen, C. Song, Y. Nishino, Y. Kohmura, T. Ishikawa, D. Ramunno-Johnson, T. K. Lee and S. H. Risbud, "Three-Dimensional GaN-$Ga_2O_3$ Core Shell Structure Revealed by X-ray Diffraction Microscopy", *Phys. Rev. Lett.* **97**, 215503 (2006).

34. E. Lee, B.P. Fahimian, C. V. Iancu, C. Suloway, G. E. Murphy, E. R. Wright, G. J. Jensen and J. Miao, "Radiation Dose Reduction and Image Enhancement in Biological Imaging through Equally Sloped Tomography", *J. Struct. Biol.* **164**, 221-227 (2008)

35. H. Jiang, C. Song, C.-C. Chen, R. Xu, K. S. Raines, B. P. Fahimian, C.-H. Lu, T. K. Lee, A. Nakashima, J. Urano, T. Ishikawa, F. Tamanoi, and J. Miao, "Quantitative 3D Imaging of Whole, Unstained Cells by Using X-ray Diffraction Microscopy", *Proc. Natl. Acad. Sci. USA* **107**, 11234-11239 (2010).

36. B. P. Fahimian, Y. Mao, P. Cloetens, and J. Miao, "Low Dose X-ray Phase-Contrast and Absorption CT Using Equally-Sloped Tomography", *Phys. Med. Bio.* **55**, 5383-5400 (2010).

37. Y. Zhao, E. Brun, P. Coan, Z. Huang, A. Sztrokay, P. C. Diemoz, S. Liebhardt, A. Mittone, S. Gasilov, J. Miao and A. Bravin, "High resolution, low dose phase contrast x-ray tomography for 3D diagnosis of human breast cancers", *Proc. Natl. Acad. Sci. USA* **109**, 18290-18294 (2012)

38. K. S. Raines, S. Salha, R. L. Sandberg, H. Jiang, J. A. Rodriguez, B. P. Fahimian, H. C. Kapteyn, J. Du and J. Miao. "Three-dimensional structure determination from a single view", *Nature* **463**, 214-217 (2010).

39. C.-C. Chen, H. Jiang, L. Rong, S. Salha, R. Xu, T. G. Mason and J. Miao. "Three-dimensional imaging of a phase object from a single sample orientation using an optical laser", *Phys. Rev. B* **84**, 224104 (2011).

# CHAPTER 2

## Electron Tomography at 2.4 Å Resolution

M. C. Scott[1*], Chien-Chun Chen[1*], Matthew Mecklenburg[1*], Chun Zhu[1], Rui Xu[1], Peter Ercius[2], Ulrich Dahmen[2], B. C. Regan[1] & Jianwei Miao[1]

[1]*Department of Physics and Astronomy and California NanoSystems Institute, University of California, Los Angeles, CA 90095, USA.*

[2]*National Center for Electron Microscopy, Lawrence Berkeley National Laboratory, Berkeley, CA 94720, USA.*

Published in *Nature* **483**, 444-447 (2012).

[*]*These authors contributed equally to this work.*

**Transmission electron microscopy (TEM) is a powerful imaging tool that has found broad application in materials science, nanoscience and biology[1-3]. With the introduction of aberration-corrected electron lenses, both the spatial resolution and image quality in TEM have been significantly improved[4,5] and resolution below 0.5 Å has been demonstrated[6]. To reveal the 3D structure of thin samples, electron tomography is the method of choice[7-11], with resolutions of ~1 nm$^3$ currently achievable[10,11]. Recently, discrete tomography has been used to generate a 3D atomic reconstruction of a silver nanoparticle of 2-3 nm in diameter[12], but this statistical method requires prior knowledge of the particle's lattice structure and requires that the atoms fit rigidly on that lattice. Here we report the experimental demonstration of a general electron tomography method that achieves atomic scale resolution without initial assumptions about the sample structure. By combining a novel projection alignment and tomographic reconstruction method with scanning transmission electron microscopy, we have determined the 3D structure of a ~10 nm gold nanoparticle at 2.4 Å resolution. While we cannot identify all the atoms inside the nanoparticle, individual atoms are observed in some regions of the particle and several 3D grains are identified at atomic scale resolution. The 3D surface morphology and internal lattice structure revealed are consistent with a distorted icosahedral multiply-twinned particle. We anticipate that this general method can be applied to not only determine the 3D structure of nanomaterials at atomic scale resolution[13-15], but also improve the resolution and image quality in other tomography fields[7,9,16-20].**

Since its introduction in 1968, electron tomography has been primarily used to determine the 3D structure of biological samples[7,9]. In the last decade, electron tomography has been increasingly applied in materials science and nanoscience through the use of

scanning transmission electron microscopy (STEM)[8,10,11] The highest resolution presently achieved by STEM tomography is around 1 nm in three dimensions[10,11], although slightly higher resolution has been obtained in a study of fullerene-like nanostructures with bright-field electron tomography[21]. A general electron tomography method with atomic scale resolution, however, has not been demonstrated for several reasons. First, aligning the projections of a tomographic tilt series to a common axis with atomic scale precision is technically challenging. Second, radiation damage limits the number of projections that can be acquired from a single object[13,22]. Finally, specimens cannot usually be tilted beyond ±79°, preventing acquisition of data from the "missing wedge"[7-11]. Here we demonstrate that these limitations can be overcome or alleviated by applying a novel alignment approach and an iterative tomographic reconstruction method to a tilt series obtained via annular dark field (ADF)-STEM.

The conventional alignment approach used in electron tomography either relies on fiducial markers such as colloidal gold beads or is based on the cross-correlation between neighboring projections[7,9]. To our knowledge, neither of these approaches can achieve atomic scale alignment accuracy. To overcome this limitation, we have developed a method based on the center of mass (CM), which is able to align the projections of a tilt series at atomic scale accuracy even with relatively high noise (Methods). To address the other two difficulties, we have implemented a data acquisition and tomographic reconstruction method, termed equally sloped tomography (EST)[23,16,18-20]. Compared to conventional tomography that reconstructs a 3D object from a tilt series of projections with constant angular increments, EST acquires a tilt series with equal slope increments, and then iterates back and forth between real and reciprocal space (Methods). In each iteration, constraints such as the sample boundary (*i.e.* support) and positivity of the Coulomb potential are

applied in real space, while the measured projectional slices (*i.e*. the Fourier transform of the real space projections) are enforced in reciprocal space. Each iteration is monitored by an error metric, and the algorithm is terminated after reaching a maximum number of iterations.

To test the feasibility of achieving an atomic scale resolution tomographic reconstruction by the CM and EST methods, we first conducted numerical simulations on a ~5 nm gold nanoparticle with icosahedral symmetry and a total of 3871 atoms (Supplementary Figs. 3a, 4a, c and e). A tilt series of 55 projections was obtained from the particle using multislice STEM calculations[24] (energy: 300 keV, spherical aberration: 1.2 mm, illumination semi-angle: 7.98 mrad, defocus: 48.6 nm, detector inner and outer angles: 13 and 78 mrad). To minimize non-linear intensity contributions caused by dynamical scattering and the electron channeling[25], projections along zone axis orientations were avoided. The tilt angles range from -72.6° to +72.6° with equal slope increments. To simulate experimental conditions, the tilt angles were continuously shifting from 0° to 0.5° over the process of the tilt series and the magnification of the images was continuously changing from 0 to 0.2%. Each projection in the tilt series was arbitrarily shifted along the X- and Y-axes, where the electron beam direction is parallel to the Z-axis. Poisson noise was added to each projection in the tilt series with a total electron dose of $6.1\times10^6$ e/Å$^2$. Supplementary Fig. 3 shows a linear projection of the model at 0° and the corresponding multislice STEM projection. The increase of the atom size in the multislice projection was observed, which was caused by diffraction and dynamical scattering effects in the nanoparticle.

The 55 projections were aligned to a common tilt axis with the CM method, and were then reconstructed with the EST algorithm. Supplementary Figs. 4b, d, and f show

three 2.5 Å thick central slices of the 3D reconstruction in the XY, ZX and ZY planes. Although the missing wedge problem was not completely solved (the top and bottom parts in Supplementary Fig. 4f), and the size of the reconstructed atoms was somewhat increased due to the non-linear and diffraction effects, the overall atomic positions and grain boundaries in the 3D reconstruction are consistent with the model. The simulation results indicate that the CM and EST methods can be used to achieve an atomic scale resolution reconstruction from a tilt series of 55 projections with a missing wedge, non-linear effects, Poisson noise and experimental errors.

Next, the CM and EST methods were applied to experimental tilt series acquired from gold nanoparticles. Nanoparticles are an important class of materials with properties different from either molecules or bulk solids[13-15], and nano-gold is among the most widely studied of this class of material due to its broad applications in chemistry, biology, materials science, nanoscience and nanotechnology[26]. In this study, we imaged gold particles with a diameter of ~10 nm as smaller particles are not as stable under an electron beam[13,22]. To reduce the electron dose, we used a low exposure data acquisition scheme with a 300 keV ADF-STEM (Methods). When focusing an image, a nearby nanoparticle was first viewed (not the particle of interest), thus reducing the unnecessary radiation dose to the particle under study. Using this scheme, we acquired several tomographic tilt series of gold nanoparticles. Supplementary Fig. 5 shows a tilt series of 69 projections and their Fourier transforms, with a total electron dose of ~$7.6\times10^6$ e/Å$^2$. Supplementary Fig. 6 shows three 0° projections and their Fourier transforms measured during the acquisition of this tilt series to monitor the effects of radiation damage. While some minor shape changes occurred, the crystal lattice structure of the particle remained reasonably consistent throughout the experiment. To investigate the non-linear effects in the experiment, we simulated a 10 nm

gold particle with icosahedral symmetry and obtained a 11.5 Å thick portion of the 0° projection by using multislice STEM calculations[24] (Supplementary Fig. 7). Although the size of the atom size was increased due to the non-linear diffraction and dynamical scattering effects, the multislice STEM projection exhibits consistent crystal lattice structure with the model. We then calculated a tilt series for a 2.5 Å central slice using the multislice simulations. The tilt series consists of 69 projections with a tilt range of ±72.6°. Supplementary Fig. 8 shows the model and reconstructed slices. The atomic positions and the internal grain boundaries are reasonably well resolved except in very few places (including the origin) which are mainly caused by the non-linear effects in the projections.

After investigating the non-linear effects, we performed post data analysis of the experimental tilt series (Methods), and aligned the projections with the CM method. To reconstruct the 3D structure, we first estimated a loose 3D support, defined to be larger than the particle boundary. After 500 iterations of the EST algorithm, the reconstruction was used to determine a tight support (*i.e.*, close to the true boundary of the particle). Using the tight support, we ran another 500 iterations and obtained a final 3D structure. To examine the quality of the reconstruction, we calculated 69 projections from the final 3D structure and found the average normalized discrepancy with the measured projections to be 6.7% (Supplementary Methods and Supplementary Tab. 1). Three representative measured and calculated projections at different particle orientations are shown in Fig. 1 and Supplementary Fig. 9. While minor shape changes occurred in few areas, the overall shape and lattice structure agree well between measured and calculated projections. To more rigorously examine the accuracy of the reconstruction, an EST reconstruction was performed from 68 experimental projections by removing the 7.1° projection. The 3D reconstruction was then projected back to calculate the projection at 7.1°, which is

reasonably consistent with the experimentally measured one (Supplementary Fig. 10).

To estimate the resolution achieved in the reconstruction, we chose a 3.36 Å thick central slice in the XY plane. Figs. 2a and b show the slice and its Fourier transform in which the distance between two neighboring atom columns and the location of the Bragg peaks indicate that a resolution of 2.4 Å was achieved in the X and Y directions. To estimate the resolution along the Z-axis (beam direction), we selected a 3.36 Å thick slice with the horizontal axis along the Z-axis (Figs. 2c and d). The resolution close to the Z-axis was determined to be 2.4 Å. Individual atoms are visible in some regions of the slices, but not all atoms can be identified in the slices. Supplementary Fig. 11 shows two 3.36 Å thick slices in a different orientation, exhibiting crystal lattice structure not visible in Fig. 2. The apparent flattening of the particle along the beam axis was also observed in the 3D reconstructions (Fig. 2 and Supplementary Movie 1), and was likely caused by the interaction between the nanoparticle and the Si substrate.

To visualize the internal structure and the morphology of the gold nanoparticle, we generated 3D volume and iso-surface renderings of the reconstruction, in which both surface and internal lattice structures are visible (Supplementary Movies 1 and 2). Fig. 3a and b show volume renderings of the nanoparticle and their Fourier transforms (insets) at the 2- and 3-fold symmetry orientations. The corresponding iso-surface renderings at the same orientations are shown in Figs. 3c and d. The overall 3D shape and facets of the nanoparticle are consistent with an icosahedron (insets in Figs. 3c and d). To identify internal 3D grains, we applied the 3D Fourier transform to the reconstruction. By identifying the Bragg peaks of each major grain and applying the 3D inverse Fourier transform to the selected Bragg peaks, we determined four major 3D grains inside the gold nanoparticle (Methods). Fig. 4 and Supplementary movie 3 show a volume rendering of the

four 3D grains at atomic scale resolution, in which grains 1, 2 and grains 3, 4 are related by mirror-reflection across the horizontal interfaces marked by dotted lines. The angle enclosed by close-packed planes across these interfaces was measured to be 69.9°±0.8° between grains 1 and 2, and 71.3°±0.8° between grains 3 and 4, both of which are consistent with the angle for an fcc twin boundary (70.53°). By applying the same method to some other Bragg peaks, we identified 3D grains in the top and bottom parts of the particle (Supplementary Fig. 12). The surface morphology (facets) and the internal atomic structures (grains) suggest that this is a distorted icosahedral multiply-twinned particle, typically found for nano-gold in the size range above 10 nm[27].

By combining the CM alignment technique and the EST reconstruction method with an ADF-STEM, we have determined the 3D structure of a ~10 nm gold nanoparticle at 2.4 Å resolution from a tilt series of 69 projections with a missing wedge. Several 3D grains are identified inside the nanoparticle at atomic scale resolution. While individual atoms are visible in some regions of the nanoparticle, we cannot determine all the atomic positions inside the particle. In order to identify all the atoms (estimated to be ~23800) without using atomicity and bond information, a resolution higher than 2.4 Å is needed, which requires future developments. With aberration-corrected STEM[4,28,29], better 3D resolution and image quality should be achievable, but extended depth-of-field techniques may have to be applied to the tilt series before the EST reconstruction can be performed. Compared to atom-probe tomography[30], this non-destructive technique can not only handle isolated nanoparticles, but also provide 3D local structure of complex nanomaterials at atomic scale resolution.

# Methods Summary

Gold nanoparticles with size of ~10 nm (Ted Pella) were supported on 5 nm thick Si membranes (TEMwindows.com) which can withstand plasma cleaning for a longer period than carbon substrates to alleviate carbon contamination. Tomographic tilt series with equal slope increments were acquired from the gold nanoparticles by using an ADF-STEM (FEI Titan 80-300). The tilt angles ($\theta$) were determined by[23,16] $\theta = -\tan^{-1}[(N+2-2n)/N]$ for $n$ = 1, … ,$N$ and $\theta = \pi/2 - \tan^{-1}[(3N+2-2n)/N]$ for $n = N$+1, …, 2$N$ with $N$ = 32 or 64 in this experiment. The angles beyond ±72.6° were not accessible due to the geometry of the support grid. To monitor the radiation induced stability effect, several projections at the same particle orientation were measured during the acquisition of each tilt series (Supplementary Fig. 6). To improve the 3D reconstruction and enhance the signal to noise ratio, the background of the projections was subtracted and 2×2 pixel binning was performed for each projection. After post data analysis, the tilt series was aligned with the CM method (Methods). The reconstruction of the aligned tilt series was conducted using the EST method, which iterated back and forth between real and reciprocal space with constraints enforced in real space and measured data in reciprocal space (Methods, Supplementary Methods and Supplementary Fig. 2). To examine the reconstruction quality, the reconstructed 3D structure was projected back to obtain 69 projections, which were compared to the corresponding measured ones. An average $R_{real}$ (Supplementary Methods) was calculated to be 6.7%, indicating a good quality reconstruction (Fig. 1, Supplementary Tab. 1).

# References


1. Williams, D. B. & Carter, C. B. *Transmission Electron Microscopy: A Textbook for Materials Science* 2nd ed. (Springer, 2009).
2. Spence, J. C. H. *Experimental High-Resolution Electron Microscopy* 3rd ed. (Oxford University Press, New York, 2003).
3. Frank, J. *Three-Dimensional Electron Microscopy of Macromolecular Assemblies.* (Oxford University Press, USA, 2006).
4. Batson, P. E., Dellby, N. & Krivanek, O. L. Sub-ångstrom resolution using aberration corrected electron optics. *Nature* **418**, 617-620 (2002).
5. Haider, M., *et al.* Electron microscopy image enhanced. *Nature* **392**, 768-769 (1998).
6. Erni, R., Rossell, M. D., Kisielowski, C. & Dahmen, U. Atomic-resolution imaging with a sub-50-pm electron probe. *Phys. Rev. Lett.* **102**, 096101(2009).
7. Frank, J. *Electron Tomography* (Plenum, New York, 1992).
8. Midgley, P. A. & Weyland, M. 3D electron microscopy in the physical sciences: the development of Z-contrast and EFTEM tomography. *Ultramicroscopy* **96**, 413–431 (2003).
9. Lu i , V., Förster, F. & Baumeister, W. Structural studies by electron tomography: from cells to molecules. *Annu. Rev. Biochem.* **74**, 833-865 (2005).
10. Midgley, P. A. & Dunin-Borkowski, R. E. Electron tomography and holography in materials science. *Nature Materials* **8**, 271-280 (2009).
11. Arslan, I., Yates, T. J. V., Browning, N. D. & Midgley, P. A. Embedded nanostructures revealed in three dimensions. *Science* **309**, 2195-2198 (2005).

12. Van Aert, S., Batenburg, K. J., Rossell, M. D., Erni, R. & Van Tendeloo, G. Three-dimensional atomic imaging of crystalline nanoparticles. *Nature* **470**, 374–377 (2011).

13. Marks, L. D. Experimental studies of small particle structures. *Rep. Prog. Phys*. **57**, 603-649 (1994).

14. Billinge, S. J. L. & Levin, I. The problem with determining atomic structure at the nanoscale. *Science* **316**, 561-565 (2007).

15. Yacaman, M. J., Ascencio, J. A., Liu, H. B. & Gardea-Torresdey, J. Structure shape and stability of nanometric sized particles. *J. Vac. Sci. Technol. B* **19**, 1071-1023 (2001).

16. Lee, E. *et al*. Radiation dose reduction and image enhancement in biological imaging through equally sloped tomography. *J. Struct. Biol.* **164**, 221–227 (2008).

17. Kak, A.C. & Slaney, M. *Principles of Computerized Tomographic Imaging* (SIAM, Philadelphia, 2001).

18. Fahimian, B. P., Mao, Y., Cloetens, P., & Miao, J. Low dose X-ray phase-contrast and absorption CT using equally-sloped tomograph. *Phys. Med. Bio.* **55**, 5383-5400 (2010).

19. Mao, Y., Fahimian, B. P., Osher, S. J., & Miao, J. Development and optimization of regularized tomographic reconstruction algorithms utilizing equally-sloped tomography. *IEEE Trans. Image Processing* **19**, 1259-1268 (2010).

20. Jiang, H. *et al*. Quantitative 3D imaging of whole, unstained cells by using X-ray diffraction microscopy. *Proc. Natl. Acad. Sci. USA* **107**, 11234–11239 (2010).

21. Bar Sadan, M. *et al.* Toward atomic-scale bright-field electron tomography for the study of fullerene-like nanostructures. *Nano Lett*. **8**, 891-896 (2008).

22. Bovin, J. -O., Wallenberg, R. & Smith, D. J. Imaging of atomic clouds outside the surfaces of gold crystals by electron microscopy. *Nature* **317**, 47-49 (1985).

23. Miao, J., Föster, F. & Levi, O. Equally sloped tomography with oversampling reconstruction. *Phys. Rev. B* **72**, 052103 (2005).

24. Kirkland, E. J. *Advanced Computing in Electron Microscopy* 2nd ed. (Springer, 2010).

25. Howie, A. Diffraction channelling of fast electrons and positrons in crystals. *Phil. Mag.* **14**, 223-237 (1966).

26. Daniel, M. C. & Astruc, D. Gold nanoparticles: assembly, supramolecular chemistry, quantum-size-related properties, and applications toward biology, catalysis, and nanotechnology. *Chem. Rev*. **104**, 293-346 (2004).

27. Barnard, A. S., Young, N. P., Kirkland, A. I., van Huis, M. A. & Xu, H. Nanogold: a quantitative phase map. *ACS Nano* **3**, 1431–1436 (2009).

28. D. A. Muller. Structure and bonding at the atomic scale by scanning transmission electron microscopy. *Nature Materials* **8**, 263-270 (2009).

29. Pennycook, S. J. & Nellist, P. D. *Scanning Transmission Electron Microscopy: Imaging and Analysis* 1st ed. (Springer, 2011).

30. Arslan, I., Marquis, E.A., Homer, M., Hekmaty, M. & Bartelt, N.C. Towards better 3-D reconstructions by combining electron tomography and atom-probe tomography. *Ultramicroscopy* **108**, 1579-1585 (2008).

# Methods

**Sample preparation.** Gold nanoparticle solution with an average particle size of ~10 nm (Ted Pella) was sonicated for ~10 minutes to prevent aggregation. The solution was then dropcast onto 5 nm thick Si membranes (TEMwindows.com). The thin membrane with size of 100×1500 μm is supported on a 100 μm thick Si frame, allowing for a tilt range of ±83°. To avoid breaking the membrane, a micromanipulator was used to place a small drop of solution onto the outer frame of the Si grid. After gently moving the drop onto the membrane, it was removed and not allowed to dry and leave excessive gold particles and contaminants. The Si grids were cleaned pre-deposition in a Gatan Solarus plasma cleaner (Model 950) for 20s using a standard $H_2/O_2$ recipe. To further ensure removal of contaminant sources, the sample holder (Fischione Model 2020) was plasma cleaned for an hour prior to data acquisition using the same recipe.

**ADF-STEM**. STEM images of gold nanoparticles were acquired on a FEI Titan 80-300 (energy: 300 keV, spherical aberration: 1.2 mm, illumination semi-angle: 7.98 mrad and defocus: 48.6 nm). The electron beam, at spot 8 with a 50 μm C2 aperture, was focused to a probe and rastered over the sample. The scattered electrons were captured by a Fischione Model 3000 ADF detector with angles between 10 and 50 mrad from the optical axis. ADF angles were used to improve the signal to noise ratio with a low current electron beam. The maximum tilt angles were limited by the holder to ±75°.

**Low-exposure acquisition of tomographic tilt series**. In order to reduce vibration and drift during data acquisition, the sample holder was allowed to settle for one hour after insertion into the microscope, and also for several minutes after moving to each new angle. Tilt series were acquired by manually changing the angle with equal slope increments. The tilt angles (θ) were determined by[23,16] $\theta = -\tan^{-1}[(N+2-2n)/N]$ for $n$ = 1, … ,$N$ and $\theta = \pi/2 - \tan^{-1}[(3N+2-2n)/N]$ for $n = N+1, \ldots, 2N$ with $N$ = 32 or 64 in this experiment. To focus each projectional image during data acquisition, a nearby particle was used (rather than the particle of interest) to reduce the radiation dose to the particle. By using this low-exposure data acquisition scheme, we have obtained several tomographic tilt series. Supplementary Fig. 5 shows the tilt series used in this reconstruction with 69 projections and a tilt range of ±72.6°. A representative sinogram of the tilt series is shown in Supplementary Fig. 13. The probe current was ~70 pA with a dwell time of 45 μs per pixel, and the magnification of each projection was 5.2 M×. Since the pixel size in STEM mode can vary, a calibration image of the particle was taken in TEM mode, and the STEM pixel size was determined to be 0.42 Å. The total electron dose of the tilt series was estimated to be ~$7.6\times10^6$ e/Å$^2$. Supplementary Fig. 6 shows three 0° projections measured during the acquisition of this tilt series. Although some minor shape changes occurred, the crystal lattices of the particle remained reasonably consistent throughout the experiment.

**Post data analysis.** In order to apply the EST method, the background surrounding the nanoparticle in each projection has to be subtracted. To systematically eliminate the background, we first projected all the projections onto the tilt axis and obtained a set of 1D curves. We then determined the optimal cut-off value for background subtraction in each projection by maximizing the cross-correlation among these 1D curves. After background

subtraction, we binned 2×2 pixels into 1 pixel, which was used to enhance the signal to noise ratio in the projections and improve the EST reconstruction. The background subtracted and binned projections with pixel size of 0.84 Å were aligned using the CM approach and reconstructed with the EST method.

**The CM alignment method.** To achieve an atomic scale resolution reconstruction, the projections in a tilt series have to be aligned to a common axis (not necessarily the true tilt axis) with atomic scale precision in both the X- and Y-axes where the Y-axis represents the tilt axis and Z-axis the beam direction. To align the tilt series along the Y-axis, the projections were first projected onto the Y-axis and a set of 1D curves was generated. We then chose a 1D curve at 0° as a reference, and aligned the remaining curves to the reference. To align the projections along the X-axis, we developed a method based on the center of mass (CM). When a 3D object is tilted around the Y-axis from 0° to 360°, the CM of the object forms a circle. However, in the special geometry where the CM coincides with the origin of the X-axis, this circle becomes a point. To determine the CM in this special geometry, we projected each 2D projection onto the X-axis and calculated the CM along the X-axis, $x_{CM} = \sum_i x_i \rho(x_i) \Big/ \sum_i \rho(x_i)$, where $\rho(x_i)$ the Coulomb potential at position $x_i$. By varying $x_i$, we calculated a sequence of $x_{CM}$. The position of $x_j$, corresponding to $x_{CM} = 0$ or closest to 0, was the origin of the X-axis in this special geometry. We shifted this projection to set $x_j$ as the origin. Through repeating this process for all projections, we aligned the tilt series to the common axis. Both our simulation and experimental results indicate that the CM alignment is a general method and can align the projections of a tilt series at atomic scale accuracy, even with reasonably high noise and non-linear effects (Fig. 1, Supplementary Figs. 4, 8 and Tab. 1).

**The EST method**. When the projections of a tilt series are acquired with equal slope increments, it has been shown that a direct fast Fourier transform, the pseudopolar fast Fourier transform (PPFFT)[31], exists between a pseudopolar grid and a Cartesian grid. Supplementary Fig. 1 shows a pseudopolar grid and the PPFFT. For an $N \times N$ Cartesian grid, the corresponding pseudopolar grid is defined by a set of $2N$ lines, each line consisting of $2N$ grid points mapped out on $N$ concentric squares. The $2N$ lines are subdivided into a horizontal group (in blue) defined by $y = sx$, where $s$ is the slope and $|s| \leq 1$, and a vertical group (in red) defined by $x = sy$, where $|s| \leq 1$; the horizontal and vertical groups are symmetric under the interchange of $x$ and $y$, and $\Delta s = 2/N$. When these conditions are met, the PPFFT and its inverse algorithm are mathematically faithful[31]. Note that the PPFFT and its inverse algorithm were originally developed to interpolate tomographic projections from a polar to a Cartesian grid in reciprocal space. The idea of acquiring tomographic tilt-series at equal slope increments and then combining the PPFFT with iterative algorithms for 3D image reconstructions was first suggested in 2005 [23].

Compared to other data acquisition approaches such as the Saxton scheme[32], the EST data acquisition approach is different in that it acquires projections with equal slope increments in order to use the PPFFT. Although the PPFFT and its inverse provide an algebraically faithful way to do fast Fourier transform between the Cartesian and pseudopolar grids, three difficulties limit its direct application to electron tomography. First, the tilt range has to be from -90° to +90°. Second, the number of projections in a tilt series needs to be 2N for an N × N object. Third, the grid points past the resolution circle (dashed circle in Supplementary Fig. 1) cannot be experimentally determined. We overcame these limitations by combining the PPFFT with an iterative process[23,16,18-20]. Supplementary Fig. 2

shows the schematic layout of the iterative EST method. We first convert the electron micrograph projections to Fourier slices in the pseudopolar grid. As illustrated in Supplementary Fig. 1, the distance between the sampling points on the individual 2N lines of the pseudopolar grid varies from line to line. In order to calculate the Fourier slices from the projections, the fractional Fourier transform (FrFT) is used to vary the output sampling distance of the Fourier slices[33]. By applying the inverse PPFFT, we obtain a 3D image in real space. A 3D support is defined to separate the object from a zero region where the size of the zero region is proportional to the oversampling of the projections[34]. The negative-valued voxels inside the support and the voxel values outside the support are set to zero, and a new 3D image is obtained. The forward PPFFT is applied to the new image and a set of calculated Fourier slices is obtained. We then replace the corresponding calculated Fourier slices with the measured ones, and the remaining slices are kept unchanged. The iterative process is then repeated with each iteration monitored by an $R_{recip}$ (Supplementary Methods). The algorithm is terminated after reaching a maximum number of iterations. A more detailed description of the EST method is presented in Supplementary Methods. Compared to phase retrieval in coherent X-ray/electron diffraction imaging[20,35-37], the EST method aims for solving the missing data by combining an iteration process with the PPFFT algorithm.

**Identification of major 3D grains at atomic scale resolution**. The following procedures were used to determine the major 3D grains inside the gold nanoparticle. (i) Apply the 3D Fourier transform to the reconstructed nanoparticle and identify the Bragg peaks corresponding to a major grain. (ii) Use small spheres with soft edges to select these Bragg peaks and set other values to zero. (iii) Apply the 3D inverse Fourier transform to the

selected Bragg peaks and obtain a 3D image. (iv) Convolve the 3D image with a Gaussian filter and choose a cut-off value to determine the 3D shape of the grain. (v) Use the 3D shape to identify the corresponding 3D grain in the reconstructed nanoparticle. (vi) Repeat steps (i-v) to determine other major grains.


31. Averbuch, A., Coifman, R. R., Donoho, D. L., Israeli, M. & Shkolnisky, Y. A framework for discrete integral transformations I—the pseudopolar Fourier Transform. *SIAM J. Sci. Comput*. **30**, 785–803 (2008).
32. Saxton, W. O., Baumeister, W. & Hahn, M. Three-dimensional reconstruction of imperfect two-dimensional crystals. *Ultramicroscopy* **13**, 57-70 (1984).
33. Bailey, D. H. & Swarztrauber, P. N. The fractional Fourier transform and applications. *SIAM Rev.* **33**, 389–404 (1991).
34. Miao, J., Sayre, D. & Chapman, H. N. Phase retrieval from the magnitude of the Fourier transform of non-periodic objects. *J. Opt. Soc. Am. A.* **15**, 1662-1669 (1998).
35. Miao, J., Charalambous, P, Kirz, J. & Sayre, D. Extending the methodology of X-ray crystallography to allow imaging of micrometre-sized non-crystalline specimens. *Nature* **400**, 342-344 (1999).
36. Miao, J., Ohsuna, T., Terasaki, O., Hodgson, K. O. & O'Keefe, M. A. Atomic resolution three-dimensional electron diffraction microscopy. *Phys. Rev. Lett*. **89**, 155502 (2002).
37. Zuo, J. M., Vartanyants, I., Gao, M., Zhang, R. & Nagahara, L. A. Atomic resolution imaging of a carbon nanotube from diffraction intensities. *Science* **300**, 1419-1421 (2003).

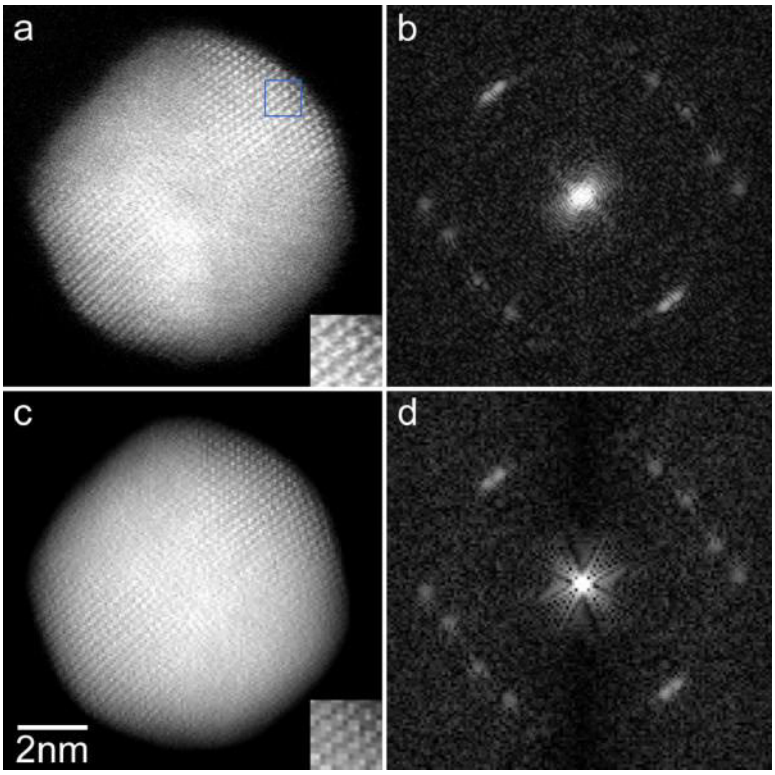


**Figure 1**. Representative measured (**a**) and calculated (**c**) projections and their Fourier transforms (**b,d**) at 7.1°, where insets show the projected atomic positions inside the blue square. The overall shape of the nanoparticle and the location of the Bragg peaks agree well, indicating a good quality 3D reconstruction.

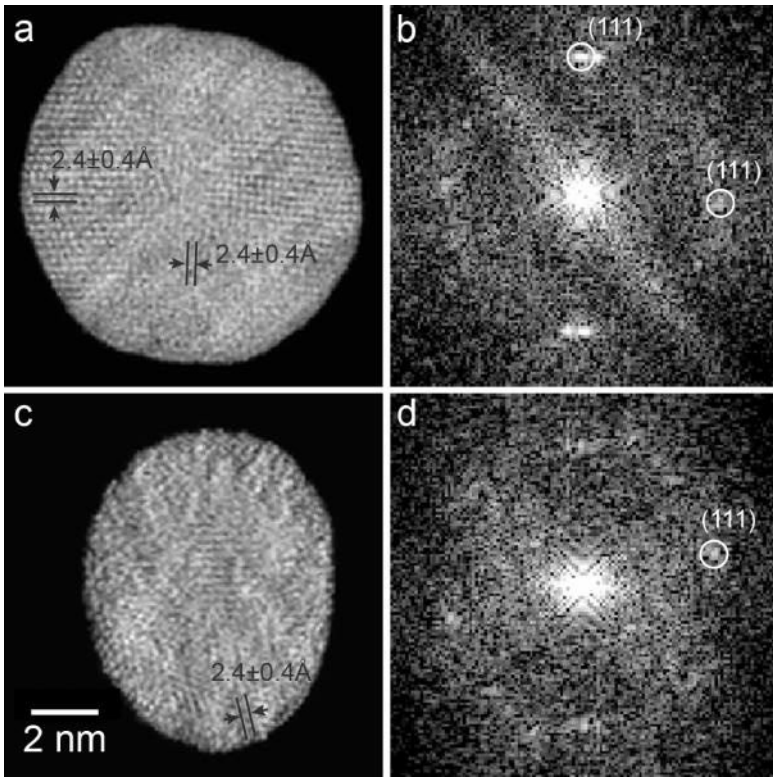


**Figure 2**. 3D resolution estimation of the reconstruction. **a** and **b**, A 3.36 Å thick central slice in the XY plane and its Fourier transform, indicating 2.4 Å resolution was achieved along the X- and Y-axes. **c** and **d**, A 3.36 Å thick slice in the ZY plane and its Fourier transform where the horizontal axis is along the Z-axis (beam direction). The resolution in the Z-axis was estimated to be 2.4 Å. Individual atoms are visible in some regions of the slices, but not all atoms can be identified in the slices.

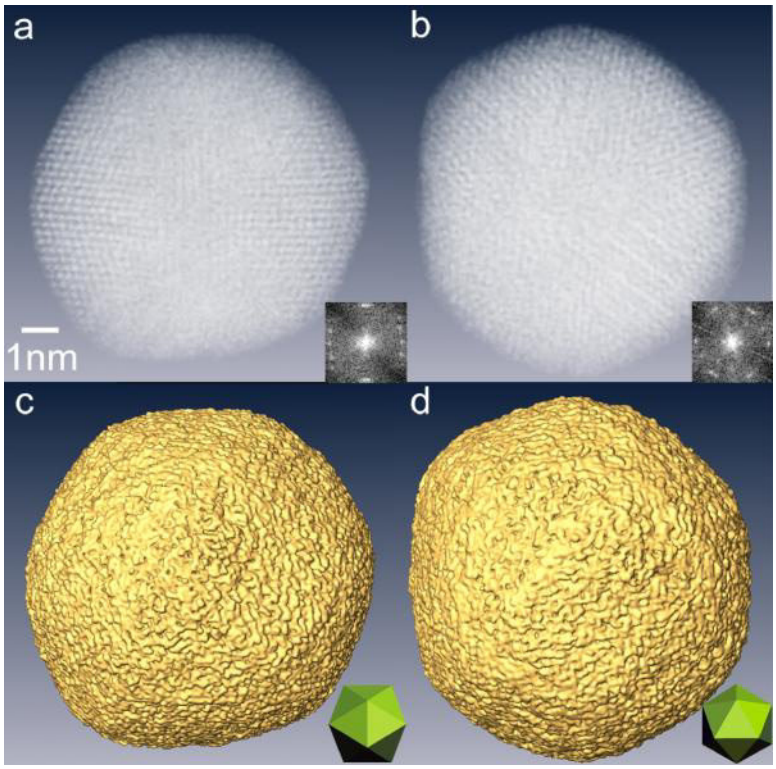


**Figure 3**. 3D structure of the reconstructed gold nanoparticle. **a** and **b**, 3D volume renderings of the nanoparticle and their Fourier transforms (insets) at the 2- and 3-fold symmetry orientations. **c** and **d**, Iso-surface renderings of the nanoparticle at the 2- and 3-fold symmetry orientations, compared to a model icosahedron at the same orientation (insets).

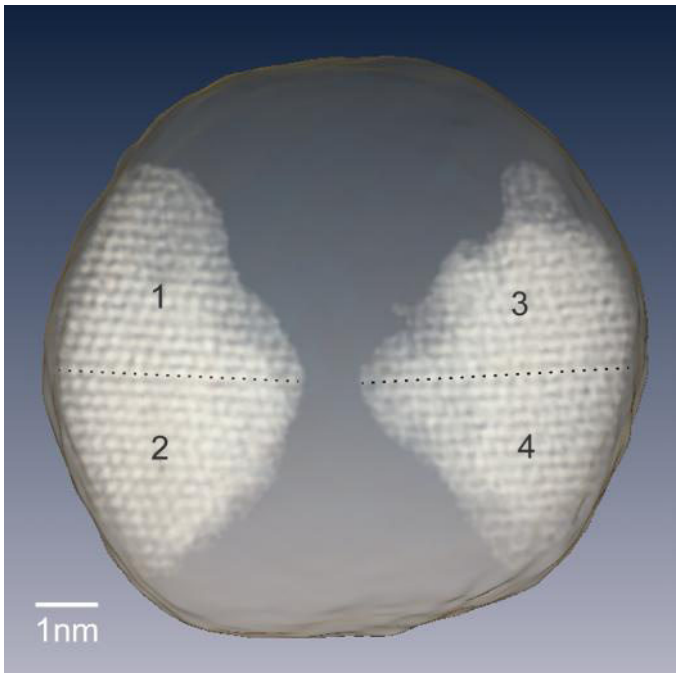


**Figure 4**. Identification of four major 3D grains inside the gold nanoparticle at atomic scale resolution. Grains 1, 2 and grains 3, 4 are related by mirror-reflection across the horizontal interfaces marked by dotted lines. The angle enclosed by close-packed planes across these interfaces was measured to be 69.9°±0.8° between grains 1 and 2, and 71.3°±0.8° between grains 3 and 4, both of which are consistent with the angle for an fcc twin boundary (70.53°).

# Supplementary Information

## Supplementary Methods

**Mathematical implementation of the EST method.** Before the iterative algorithm begins, EST requires that the projectional data be mapped onto the pseudopolar grid in reciprocal space. The EST method therefore begins with padding each projection with zeros (*i.e.,* embedding the experimental projection into a larger array of zeros) and calculating its oversampled Fourier slice on a pseudopolar grid (blue planes in Supplementary Fig.2 ) using the fractional Fourier transform (FrFT)[34]. The FrFT varies the output sampling distance of the Fourier transform and is defined in the 1D case by

$$F_{\alpha}(k) = \sum_{x=N}^{N-1} f(x) \exp(-\frac{i\pi\alpha kx}{N}) \qquad (1)$$

Eq. (1) is equivalent to the standard 1D FFT but with an extra factor of in the exponent. By choosing an appropriate value for , the projection data can be mapped on to the grid points of any line on the pseudopolar grid. The oversampling concept (*i.e.* sampling the Fourier slice at a frequency finer than the Nyquist interval)[34] has been widely used to solve the phase problem in coherent diffraction imaging[20,35-37]. In the EST method, oversampling does not provide extra information about the object, but allows the use of iterative algorithms to extract the correlated information within the projections. In the first iteration, the grid points outside the resolution circle (dashed line in Supplementary Fig. 1 left) and on the missing projections are set to zero. We also note that the reconstruction can sometimes be improved by supplying each missing projection with the average of its two neighboring projections as an initial input. Once this preprocessing step has occurred, the algorithm iterates back and forth between real and

Fourier space, shown in Supplementary Fig. 2. The $j^{th}$ iteration consists of the following 5 steps:

i) Apply the inverse PPFFT to the Fourier-space slices $F_j(\vec{k})$, and obtain a real-space image, $f_j(\vec{r})$. Our recent work has shown that the inverse PPFFT can be replaced by the adjoint PPFFT, allowing for faster convergence without compromising the accuracy[19].

ii) A support (S) is determined based on the oversampling of the projections[35]. Outside the support, $f_j(\vec{r})$ is set to zero and inside the support, the negative values of $f_j(\vec{r})$ are set to zero. A new image, $f'_j(\vec{r})$, is obtained,

$$f'_j(\vec{r}) = \begin{cases} 0 & \text{if } \vec{r} \notin S \text{ or } f_j(\vec{r}) < 0 \\ f_j(\vec{r}) & \text{if } \vec{r} \in S \text{ and } f_j(\vec{r}) \geq 0 \end{cases} \quad (2)$$

iii) Apply the PPFFT to $f'_j(\vec{r})$ and obtain new Fourier slices, $F'_j(\vec{k})$.

iv) Calculate the Fourier slices for the $(j+1)^{th}$ iteration,

$$F_{j+1}(\vec{k}) = \begin{cases} F'^{\phi}_j(\vec{k}) & \text{for the missing projection angles } (\phi) \\ F^{\theta}_m(\vec{k}) & \text{for the measured projection angles } (\theta) \end{cases} \quad (3)$$

where $F'^{\phi}_j(\vec{k})$ and $F'^{\theta}_m(\vec{k})$ represent the missing and measured Fourier slices, and $\phi \cup \theta$ forms a complete set of angles for the pseudopolar grid.

v) An $R_{recip}$ is calculated,

$$R_{recip} = \frac{\sum \left| \left| F^{\theta}_m(\vec{k}) \right| - \left| F'^{\theta}_j(\vec{k}) \right| \right|}{\sum \left| F^{\theta}_m(\vec{k}) \right|} \quad (4)$$

where $F^{\theta}_m(\vec{k})$ and $F'^{\theta}_j(\vec{k})$ represent the measured and $j^{th}$ calculated Fourier slices.

In our reconstructions, the algorithm is terminated after reaching a maximum number

of iterations. To quantify the method, we project back the final 3D reconstruction to calculate a series of projections, which are quantified by an $R_{real}$,

$$R_{real} = \frac{\sum \left\| f_c^i(x,y) \right| - \left| f_m^i(x,y) \right\|}{\sum \left| f_m^i(x,y) \right|} \tag{5}$$

where $f_c^i(x,y)$ and $f_m^i(x,y)$ represent the calculated and measured projections in real space at tilt angle $i$.

# Supplementary figures

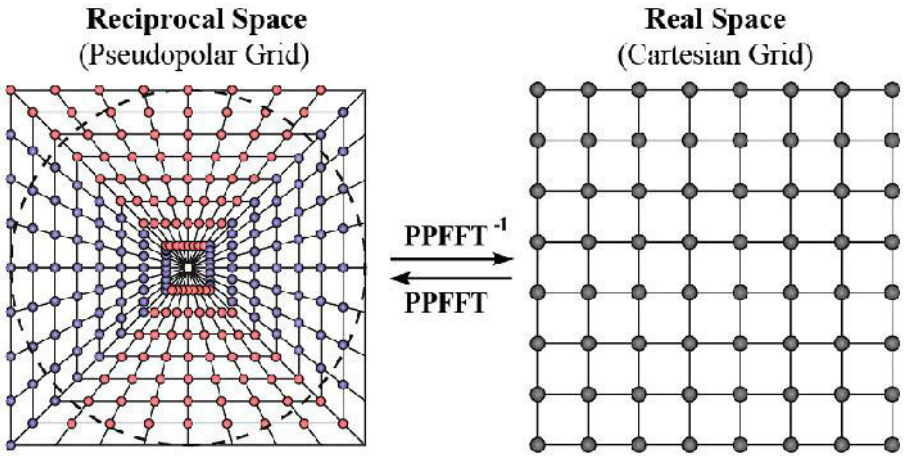


**Supplementary Fig. 1** Graphical relationship between the pseudopolar and Cartesian grids. For an $N \times N$ Cartesian grid, the corresponding pseudopolar grid is defined by a set of $2N$ lines, each line consisting of $2N$ grid points mapped out on $N$ concentric squares (left) where $N = 8$ in this case. The $2N$ lines are subdivided into a horizontal group (in blue) defined by $y = sx$, where $|s| \quad 1$, and a vertical group (in red) defined by $x = sy$, where $|s| \quad 1$; the horizontal and vertical groups are symmetric under the interchange of $x$ and $y$, and $s=2/N$ [31].The dashed circle on the pseudopolar grid represents the resolution circle. The grid points outside of the resolution circle cannot be obtained by applying the Fourier transform of the experimental projections[23].

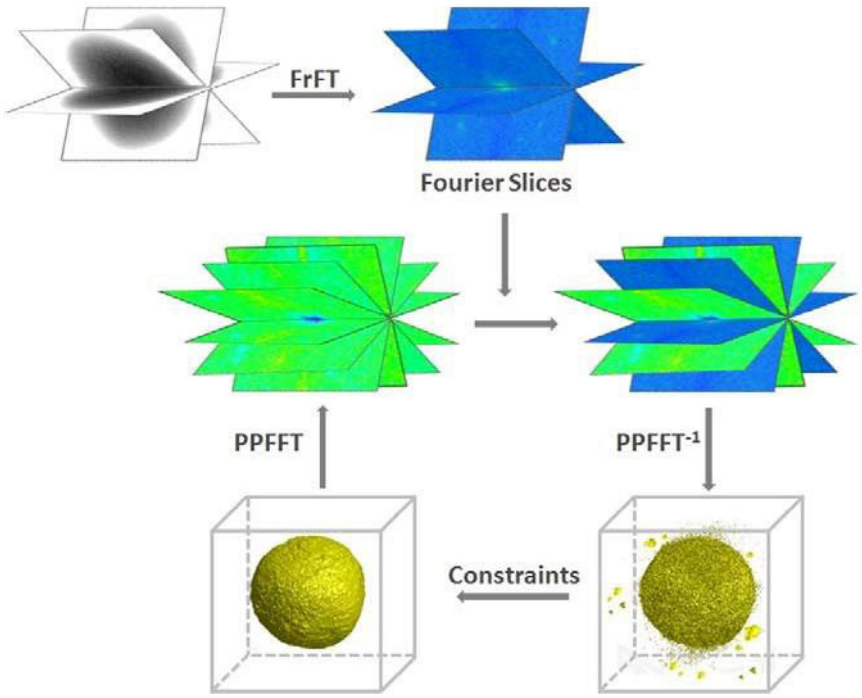


**Supplementary Fig. 2** Schematic layout of the iterative EST method. The measured projections are first converted to Fourier slices by the fractional Fourier transform (FrFT)[33]. The algorithm iterates back and forth between real and reciprocal space using the PPFFT and its inversion (Supplementary Fig. 1). In real space, the negative-valued voxels inside the support and the voxel values outside the support are set to zero (*i.e.* constraints are applied). In reciprocal space, the corresponding calculated slices are updated with the measured ones (in blue) and the remaining slices (in green) are unchanged. The algorithm is terminated after reaching a maximum number of iterations[23,16,18-20].

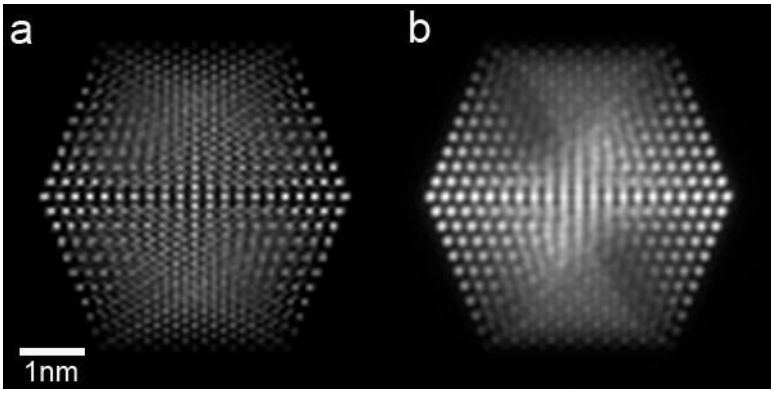


**Supplementary Fig. 3** Multislice calculations for a ~5 nm simulated Au nanoparticle with ideal icosahedral symmetry and a total of 3871 atoms. **a,** A 0° projection of the Coulomb potential. **b,** The 0° projection calculated by multislice STEM simulations (energy: 300 keV, spherical aberration: 1.2 mm, illumination semi-angle: 7.98 mrad, defocus: 48.6 nm, detector inner and outer angles: 13 and 78 mrad, pixel size: 0.37 Å). The particle was rotated by 1° each around the horizontal (X) and tilt (Y) axes to avoid the zone axis orientations and reduce the non-linear effects. The resolution in (**b**) was limited by the probe size (~1.5 Å), and the increase of atom size in the multislice projection was caused by diffraction and dynamical scattering effects in the nanoparticle.

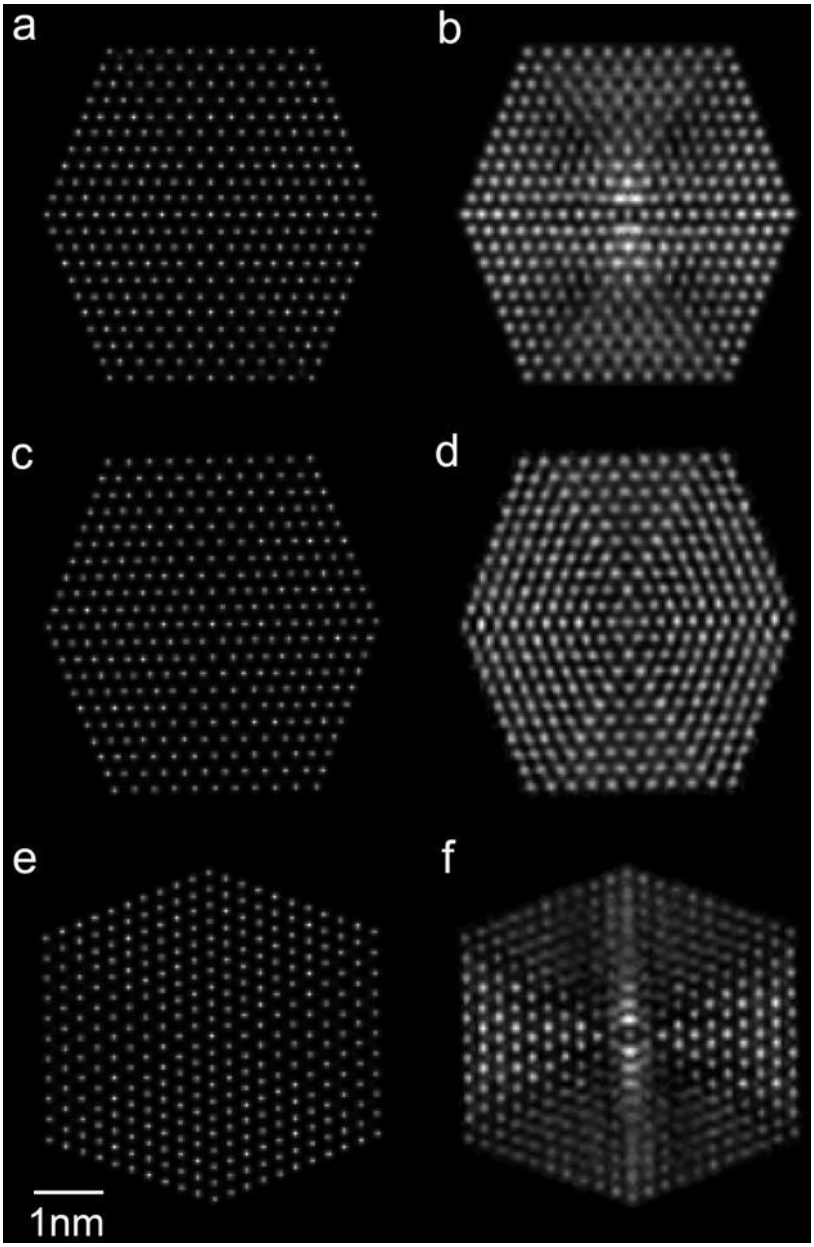


**Supplementary Figure 4.** EST reconstructions of the simulated Au nanoparticle (~5 nm) from a tilt series calculated by multislice STEM simulations (energy: 300 keV, spherical aberration: 1.2 mm, illumination semi-angle: 7.98 mrad, defocus: 48.6 nm, detector inner and outer angles: 13 and 78 mrad, pixel size: 0.5 Å). To avoid the zone axis orientations and reduce the non-linear effects, the nanoparticle was rotated by 1° each around the horizontal (X) and tilt (Y) axes. The tilt series consists of 55 projections with a tilt range of ±72.6° and equal slope increments. To simulate experimental conditions, the tilt angles

were continuously shifting from 0° to 0.5° over the process of the tilt series and the magnification of the images was continuously changing from 0 to 0.2%. The total dose of the tilt series is $6.1 \times 10^6$ e/Å$^2$ and Poisson noise was added to each projection. **a, c** and **e,** Three 2.5 Å thick central slice of the potential of the simulated nanoparticle in the XY, XZ and YZ planes, where the Z-axis is the electron beam direction. **b, d** and **f**, The corresponding 2.5 Å thick slices in the XY, XZ and YZ planes reconstructed from 55 multislice STEM projections. Although the missing wedge problem was not completele solved (the top and bottom parts in (**f**)) and the size of the reconstructed atoms was increased due to the non-linear and diffraction effects, the overall atomic positions and grain boundaries in the 3D reconstruction are consistent with the model.

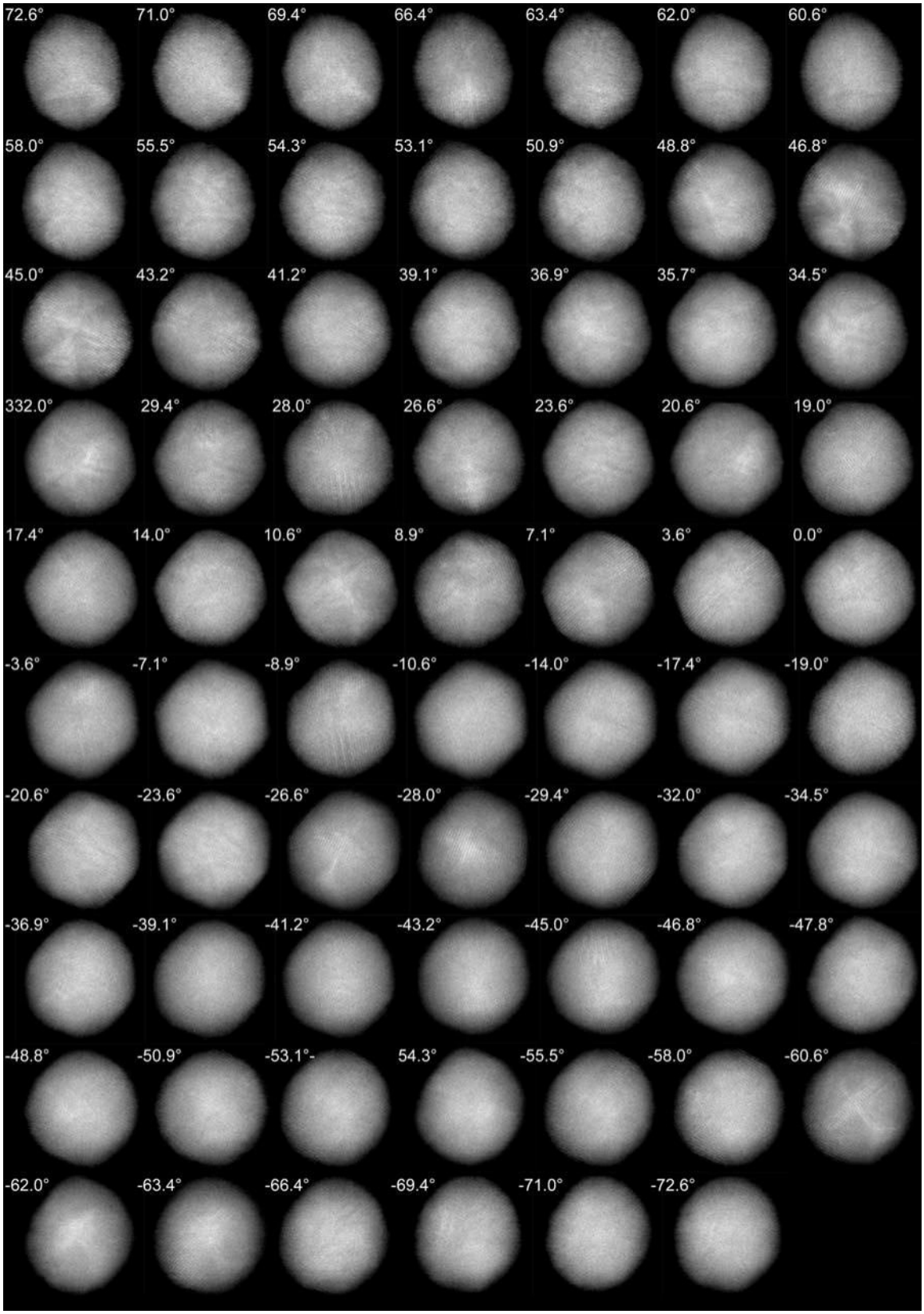
72.6° 71.0° 69.4° 66.4° 63.4° 62.0° 60.6°
58.0° 55.5° 54.3° 53.1° 50.9° 48.8° 46.8°
45.0° 43.2° 41.2° 39.1° 36.9° 35.7° 34.5°
332.0° 29.4° 28.0° 26.6° 23.6° 20.6° 19.0°
17.4° 14.0° 10.6° 8.9° 7.1° 3.6° 0.0°
-3.6° -7.1° -8.9° -10.6° -14.0° -17.4° -19.0°
-20.6° -23.6° -26.6° -28.0° -29.4° -32.0° -34.5°
-36.9° -39.1° -41.2° -43.2° -45.0° -46.8° -47.8°
-48.8° -50.9° -53.1°- 54.3° -55.5° -58.0° -60.6°
-62.0° -63.4° -66.4° -69.4° -71.0° -72.6°

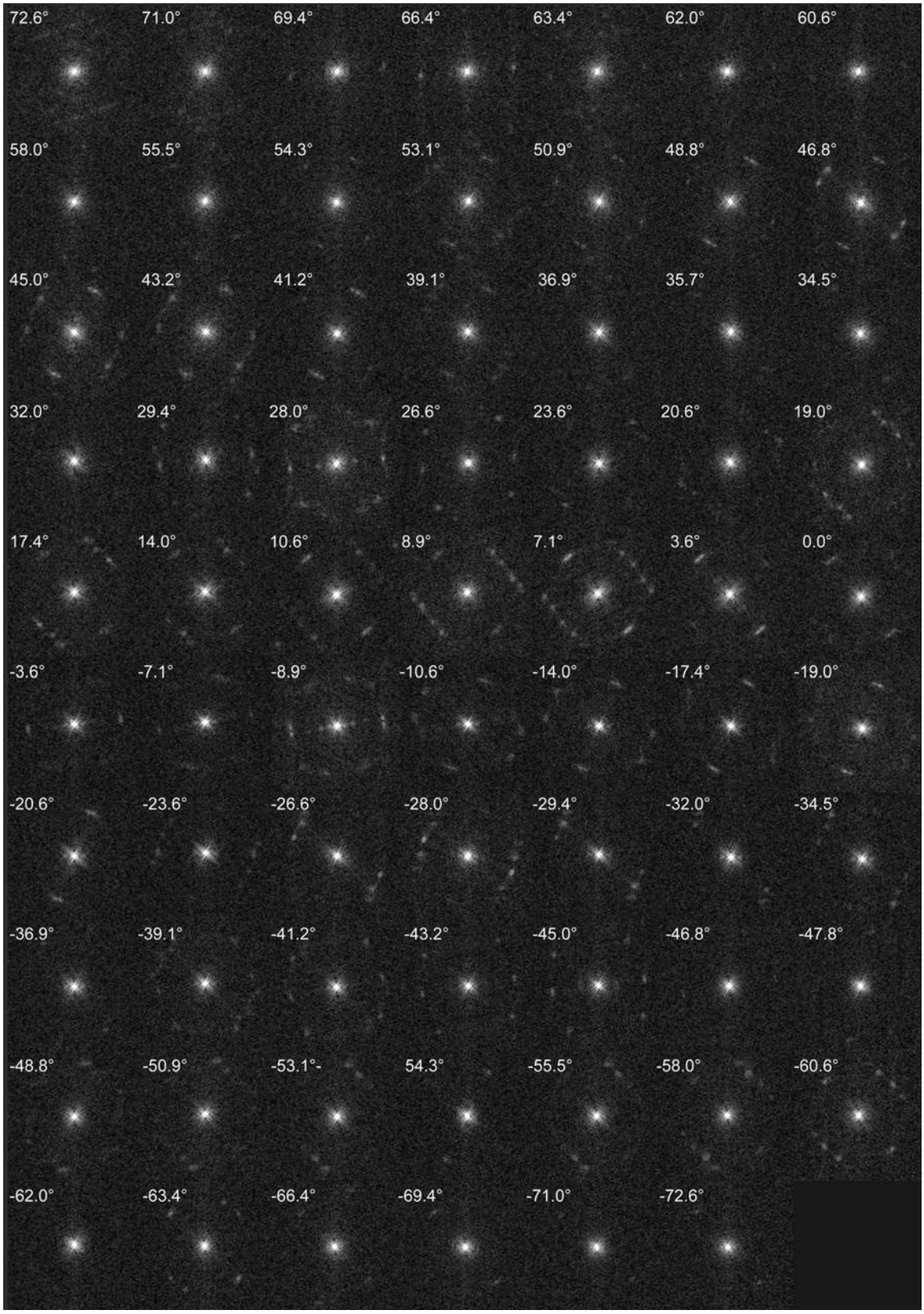
72.6° 71.0° 69.4° 66.4° 63.4° 62.0° 60.6°
58.0° 55.5° 54.3° 53.1° 50.9° 48.8° 46.8°
45.0° 43.2° 41.2° 39.1° 36.9° 35.7° 34.5°
32.0° 29.4° 28.0° 26.6° 23.6° 20.6° 19.0°
17.4° 14.0° 10.6° 8.9° 7.1° 3.6° 0.0°
-3.6° -7.1° -8.9° -10.6° -14.0° -17.4° -19.0°
-20.6° -23.6° -26.6° -28.0° -29.4° -32.0° -34.5°
-36.9° -39.1° -41.2° -43.2° -45.0° -46.8° -47.8°
-48.8° -50.9° -53.1°- 54.3° -55.5° -58.0° -60.6°
-62.0° -63.4° -66.4° -69.4° -71.0° -72.6°

**Supplementary Figure 5.** Experimental tilt series of 69 projections and their Fourier transforms, acquired from a ~10 nm gold nanoparticle with the tilt axis along the vertical axis. Crystal lattices of the nanoparticle are visible in at least 58 projections. The projections were acquired on an FEI Titan 80-300. The 300 keV electron beam, at spot 8 with a 50 μm C2 aperture, was focused to a probe with a probe current of ~70 pA, and rastered over the nanoparticle with a dwell time of 45 μs per pixel. The scattered electrons were captured by a Fischione Model 3000 ADF detector with angles between 10 and 50 mrad from the optical axis. The electron dose of this tilt series was estimated to be ~$7.6 \times 10^6$ e/Å$^2$. Among all the 69 projections, the one at 7.1° is closest to a zone-axis orientation (about 17 mrad away from the 2-fold zone axis).

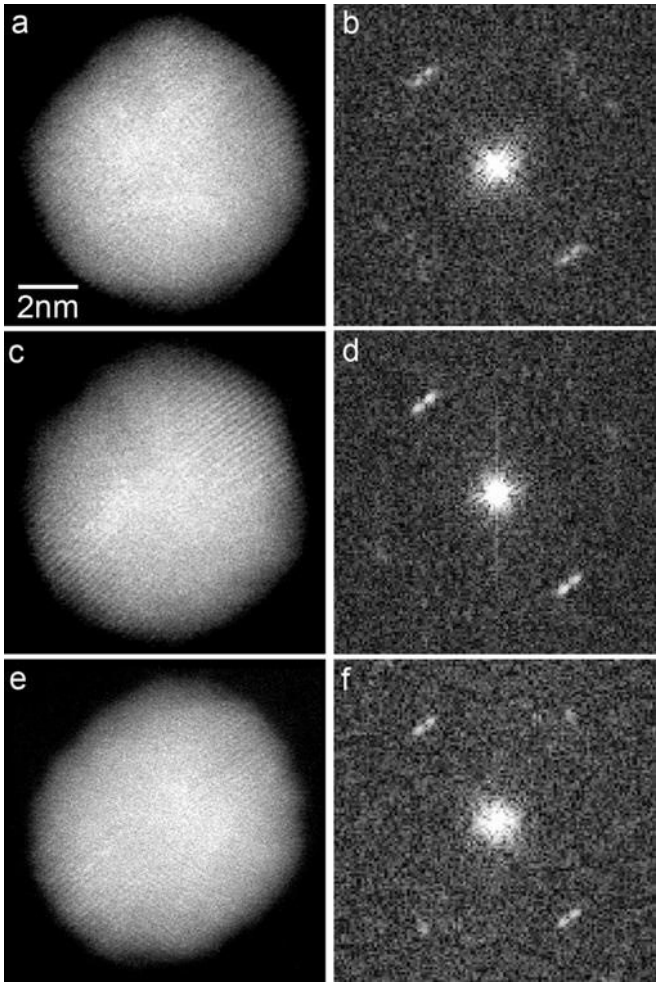


**Supplementary Figure 6.** Three 0° projections (**a**,**c**,**e**) and their Fourier transforms (**b**,**d**,**f**) measured during the acquisition of the tilt series (Supplementary Fig. 5) to monitor the effects of radiation damage. Although minor shape changes occurred, the overall crystal lattice structure of the gold nanoparticle remained reasonably consistent throughout the experiment. The minor shape change may contribute to a small degree of uncertainty in the overall shape of the reconstructed nanoparticle.

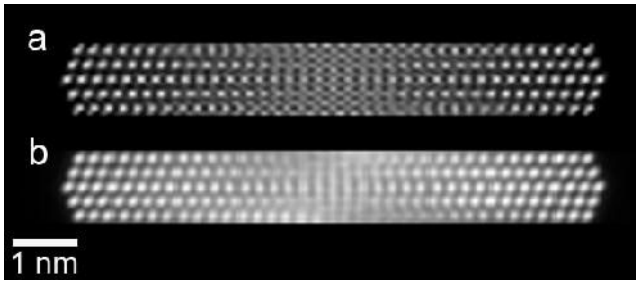


**Supplementary Fig. 7.** Multislice calculations for a ~10 nm simulated gold nanoparticle with ideal icosahedral symmetry and a total of 21127 atoms. **a,** A 11.5 Å thick portion of the projected Coulomb potential at 0°. **b,** The 11.5 Å thick portion of the 0° projection calculated by multislice STEM simulations (energy: 300 keV, spherical aberration: 1.2 mm, illumination semi-angle: 7.98 mrad, defocus: 48.6 nm, detector inner and outer angles: 13 and 78 mrad, pixel size: 0.37 Å). The particle was rotated by 1° each around the horizontal (X) and tilt (Y) axes to avoid the zone axis orientations and reduce the non-linear effects. The resolution in (**b**) was limited by the probe size (~1.5 Å), and the increase of the atom size was caused by diffraction and dynamical scattering effects in the nanoparticle. As a proof of principle, we simulated only a 11.5 Å thick portion of the 0° projection because calculating a full multislice STEM projection for a 10 nm gold particle would take enormous computational power.

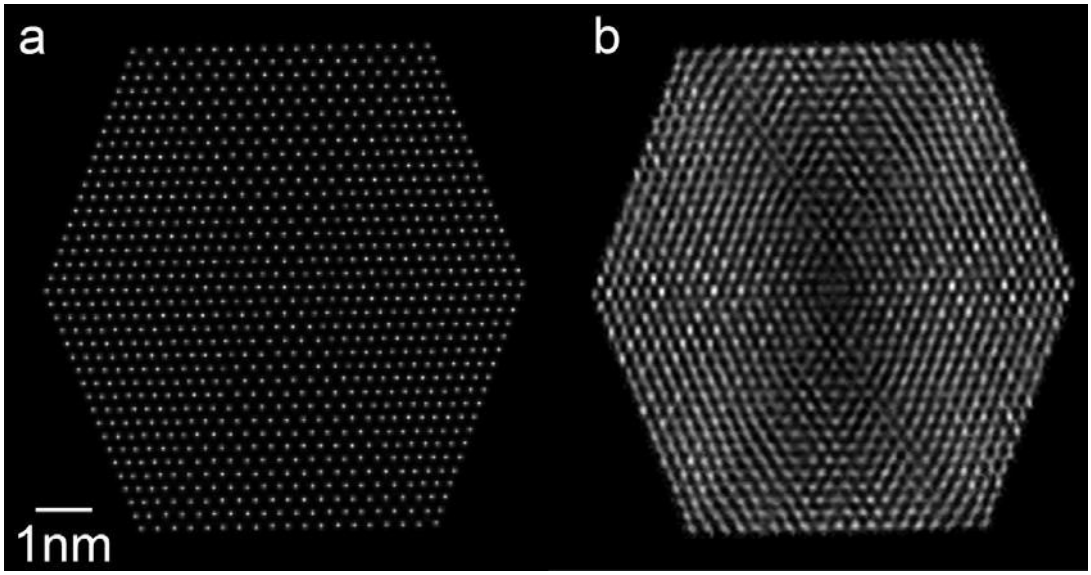


**Supplementary Fig. 8.** EST reconstruction of the ~10 nm simulated gold nanoparticle from a tilt series calculated by multislice STEM simulations (energy: 300 keV, spherical aberration: 1.2 mm, illumination semi-angle: 7.98 mrad, defocus: 48.6 nm, detector inner and outer angles: 13 and 78 mrad, pixel size: 0.5 Å). The tilt series consists of 69 projections with a tilt range of ±72.6° and equal slope increments. To avoid the zone axis orientations and reduce the non-linear effects, the nanoparticle was rotated by 1° each around the horizontal (X) and tilt (Y) axes. To simulate experimental conditions, the tilt angles were continuously shifting from 0° to 0.5° over the process of the tilt series and the magnification of the images was continuously changing from 0 to 0.2%. The total dose of the tilt series is $7.6 \times 10^6$ e/Å$^2$ and Poisson noise was added to each projection. **a,** A 2.5 Å thick central slice of the Coulomb potential in the XZ plane, where the Z-axis is the beam direction. **b,** The 2.5 Å thick slice in the XZ plane reconstructed from 69 multislice STEM projections. The atomic positions and the internal grain boundaries are reasonably well resolved except in very few places (including the origin) which are mainly caused the non-linear effects in the projections. As a proof of principle, we only

used a 2.5 Å thick slice to illustrate the EST reconstruction. Calculating a full tilt series for the ~10 nm gold nanoparticle by multislice STEM simulations would take enormous computational power.

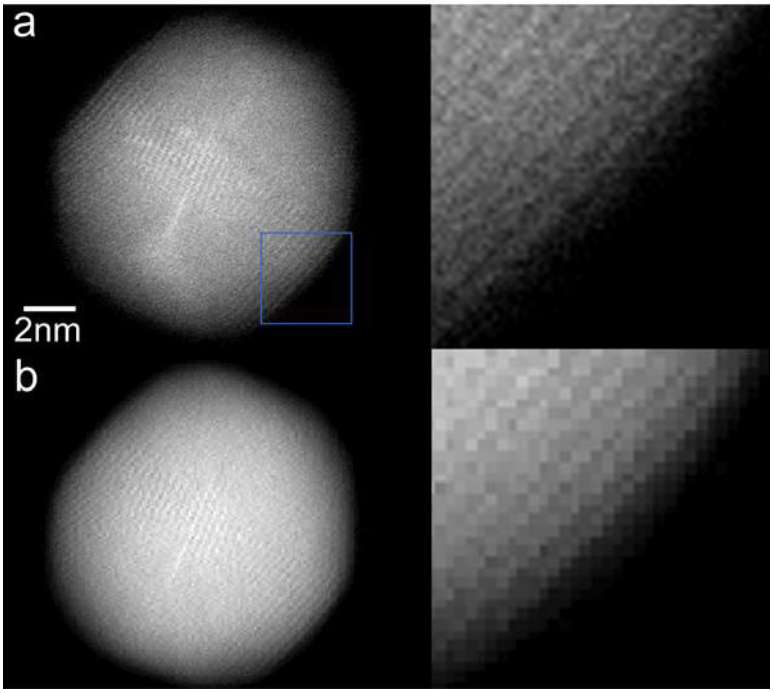


**Supplementary Figure 9.** Measured (**a**) and calculated (**b**) projections at -26.6° for the ~10 nm gold nanoparticle. The calculated projection was obtained from the 3D reconstruction of 69 projections. The zoomed images indicate that, while there are some minor differences between the two projections, the overall shape and lattice structure agree well.

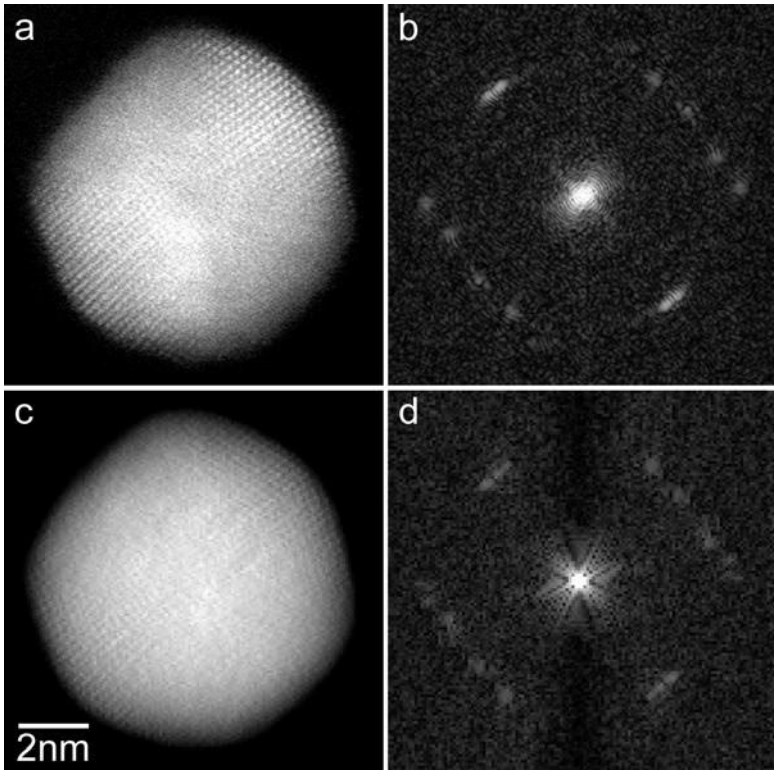


**Supplementary Figure 10.** Measured (**a**) and calculated (**c**) projections and their Fourier transforms (**b,d**) at 7.1°, where the calculated projection (**b**) was obtained from a 3D reconstruction without using the measured projection (**a**). While the contrast of the lattice fringes and the Bragg peak intensity are different between (**a**), (**b**) and (**c**), (**d**), the overall shape and the lattice structure are in reasonably good agreement. In the reconstruction, the average of two neighboring projections at 3.6° and 8.9° was input as an initial guess for the projection at 7.1°, but was not used as a constraint in each iteration.

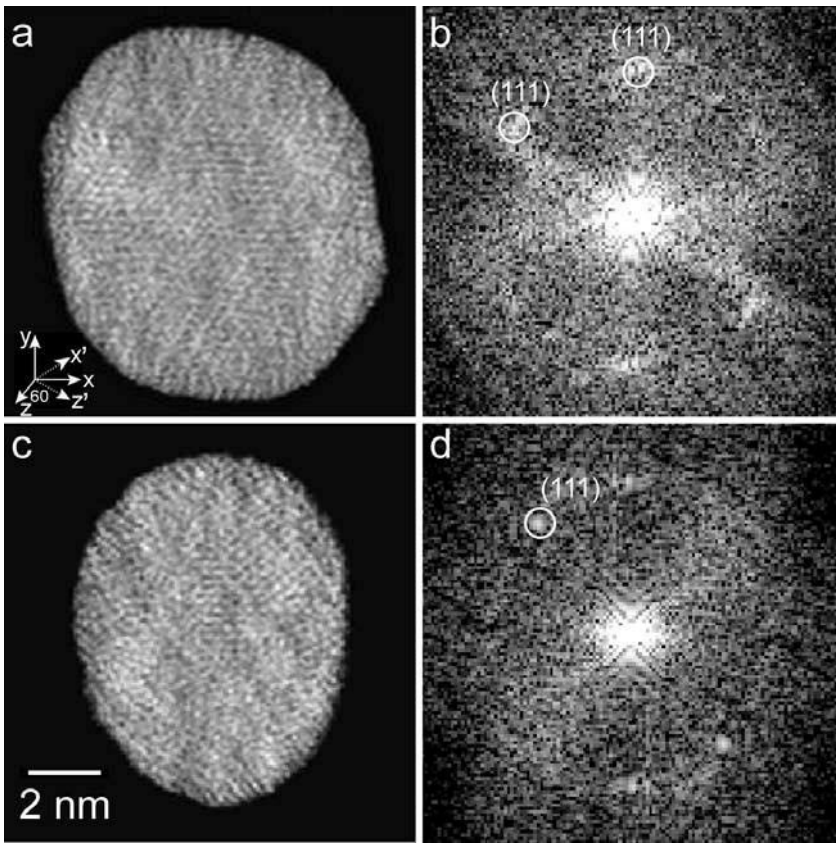


**Supplementary Figure 11. a** and **b**, A 3.36 Å slice in the X Y plane and its Fourier transform, obtained from the experimentally reconstructed Au nanoparticle. **c** and **d**, A 3.36 Å slice in the Z Y plane and its Fourier transform. The inset shows the direction of the X, Y, Z and X , and Z axes, and the angle between planes ZY and Z Y is 60°. The slices shown in Fig. 2a and c are in the XY and ZY planes, respectively. The crystal lattice structure is visible in the top and bottom areas in (**a**) and the top-right area in (**c**), but is not present in Figs. 2a and c.

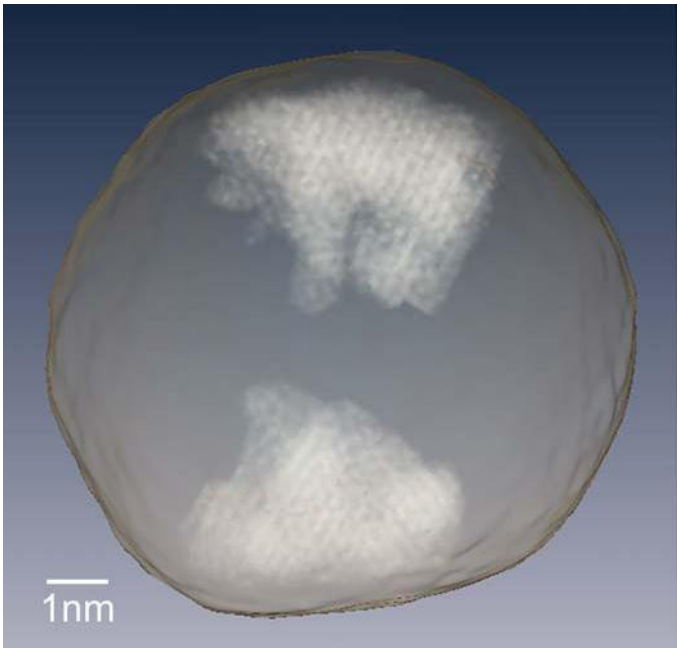


**Supplementary Figure 12.** 3D grains were identified at the atomic scale resolution in the top and bottom parts of the particle that is oriented at the 3-fold symmetry direction, whereas the particle in Fig. 4 is in the 2-fold symmetry orientation.

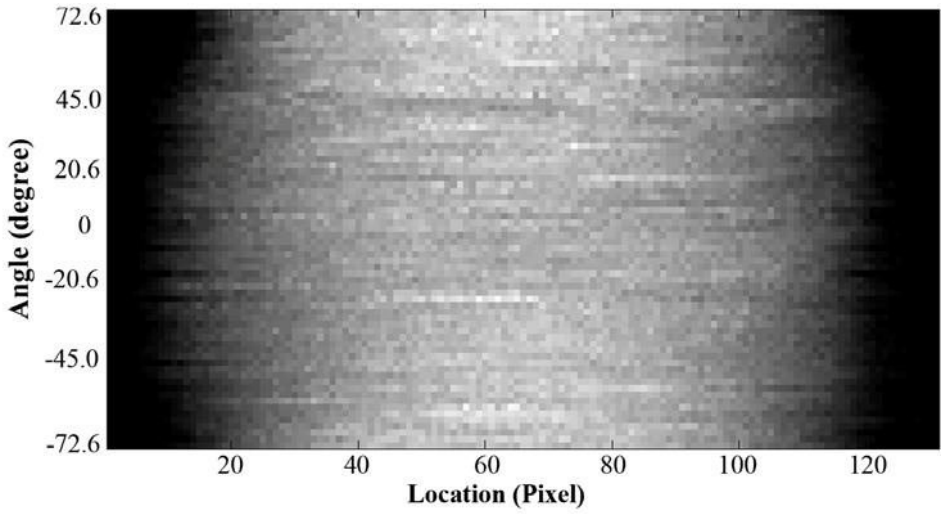


**Supplementary Figure 13.** A representative sinogram for the experimental tilt series of 69 projections acquired from the ~10 nm gold nanoparticle. The X-axis represents the pixel location with pixel size of 0.84 Å, and the Y-axis corresponds to the tilt angles of the projections. Unlike conventional tomography, the angular increments in EST are not constant. Thus the angles along the Y-axis are not equally distributed. The sudden horizontal intensity jumps are due to the lattice structure in the projections, and the rough edge is likely due to the background and noise in the projections.

# Supplementary Tables

| | | | | | | | |
|---|---|---|---|---|---|---|---|
| Angles (°) | 72.6 | 71.0 | 69.4 | 66.4 | 63.4 | 62.0 | 60.6 |
| $R_{real}$ (%) | 7.1 | 6.2 | 6.4 | 10.8 | 10.2 | 5.9 | 6.2 |
| Angles (°) | 58.0 | 55.5 | 54.3 | 53.1 | 50.9 | 48.8 | 46.8 |
| $R_{real}$ (%) | 5.8 | 6.0 | 6.5 | 6.1 | 6.5 | 6.8 | 11.6 |
| Angles (°) | 45.0 | 43.2 | 41.2 | 39.1 | 36.9 | 35.7 | 34.5 |
| $R_{real}$ (%) | 14.0 | 11.4 | 8.0 | 5.8 | 6.1 | 6.9 | 6.4 |
| Angles (°) | 32.0 | 29.4 | 28.0 | 26.6 | 23.6 | 20.6 | 19.0 |
| $R_{real}$ (%) | 7.3 | 6.5 | 6.8 | 6.6 | 5.7 | 7.6 | 5.9 |
| Angles (°) | 17.4 | 14.0 | 10.6 | 8.9 | 7.1 | 3.6 | 0 |
| $R_{real}$ (%) | 5.6 | 5.0 | 7.4 | 7.7 | 10.5 | 5.7 | 5.3 |
| Angles (°) | -3.6 | -7.1 | -8.9 | -10.6 | -14.0 | -17.4 | -19.0 |
| $R_{real}$ (%) | 5.8 | 5.7 | 6.9 | 5.1 | 5.5 | 5.3 | 6.9 |
| Angles (°) | -20.6 | -23.6 | -26.6 | -28.0 | -29.4 | -32.0 | -34.5 |
| $R_{real}$ (%) | 5.4 | 6.1 | 6.9 | 8.6 | 5.6 | 5.0 | 4.8 |
| Angles (°) | -36.9 | -39.1 | -41.2 | -43.2 | -45.0 | -46.8 | -47.8 |
| $R_{real}$ (%) | 4.7 | 4.9 | 5.9 | 6.1 | 5.6 | 6.5 | 6.0 |
| Angles (°) | -48.8 | -50.9 | -53.1 | -54.3 | -55.5 | -58.0 | -60.6 |
| $R_{real}$ (%) | 7.4 | 6.7 | 5.9 | 6.5 | 6.0 | 6.6 | 7.2 |
| Angles (°) | -62.0 | -63.4 | -66.4 | -69.4 | -71.0 | -72.6 | Average |
| $R_{real}$ (%) | 6.9 | 7.8 | 5.6 | 6.6 | 5.5 | 6.6 | 6.7 |

**Supplementary Table 1.** To examine the reconstruction quality, we projected back the reconstructed 3D structure at the same experimental tilt angles to calculate 69 projections. An $R_{real}$ (Supplementary Methods) was calculated for each tilt angle. The average $R_{real}$ for all tilt angles is 6.7%.

# CHAPTER 3

# Three-Dimensional Imaging of Dislocations in Nanoparticles at Atomic Resolution

Chien-Chun Chen[1,2*], Chun Zhu[1,2*], Edward R. White[1,2], Chin-Yi Chiu[2,3], M. C. Scott[1,2], B. C. Regan[1,2], Laurence D. Marks[4], Yu Huang[2,3] & Jianwei Miao[1,2]

[1]*Department of Physics and Astronomy,* [2]*California NanoSystems Institute, and* [3]*Departments of Materials Science and Engineering, University of California, Los Angeles, CA 90095, USA.*

[4]*Department of Materials Science and Engineering, Northwestern University, Evanston, IL 60201, USA.*

Published in *Nature* **496**, 74-77 (2013).

[*]*These authors contributed equally to this work.*

**Dislocations and their interactions strongly influence many of the properties of materials, ranging from the strength of metals and alloys to the efficiency of light-emitting diodes and laser diodes[1-4]. Presently there are several experimental methods to visualize dislocations. Transmission electron microscopy (TEM) has long been used to image dislocations in materials[5-9], and high resolution electron microscopy can reveal dislocation core structures with increasing detail[10], particularly in annular dark field (ADF)[11]. A TEM image, however, represents a 2D projection of a 3D object, although stereo TEM provides limited information about 3D dislocations[4]. X-ray topography can observe dislocations in three dimensions but with a reduced resolution[12]. Using weak-beam dark-field[13] and scanning transmission electron microscopy (STEM)[14], electron tomography has been used to image 3D dislocations at a resolution of ~5 nm[15,16]. Atom probe tomography can offer higher resolution 3D characterization of dislocations, but requires needle-shaped specimens and can detect only ~60% of the atoms in the sample[17]. A 3D technique for locating all the atoms in a dislocation has not previously been demonstrated. Here we report 3D imaging of dislocations in materials at atomic resolution with electron tomography. By identifying 3D Bragg peaks in a tomographic reconstruction, we observe nearly all the atoms in a polycrystalline Pt nanoparticle. We find the existence of atomic steps at 3D twin boundaries of the Pt nanoparticle. We have also imaged the 3D core structure of edge and screw dislocations in the nanoparticle at atomic resolution. These dislocations and the atomic steps at the twin boundaries are hidden in conventional 2D projections, and appear to be a significant stress-relief mechanism. The ability to image 3D disordered structures such as dislocations at atomic resolution is expected to find application in materials sciences, nanoscience, solid state physics and chemistry.**

Crystallography is currently the primary methodology to determine the 3D atomic structure of crystals where atomic positions are located by averaging a large number of unit cells. As a complementary to crystallography, electron tomography is an ideal technique to image the 3D local structure of materials at high resolution[15,16,18-20]. In a combination of ADF-STEM with the center of mass (CM) and equally sloped tomography (EST) methods, electron tomography has recently achieved a highest resolution of 2.4 Å[20]. However, due to dynamical scattering effects[21], the missing wedge problem[16,18,20] and Poisson noise in the tilt series, noise exists among the Bragg peaks in the 3D Fourier transform of the EST reconstruction. As a result, while lattice structure and some individual atoms are visible in the reconstruction[20], electron tomography has not been able to reveal 3D dislocations in materials at atomic resolution. Here we overcome this obstacle by combining 3D Bragg peak filtering with high angle annular dark field (HAADF)-STEM tomography, and achieve 3D imaging of dislocations in a nanoparticle at atomic resolution.

Pt nanoparticles were synthesized with selectively exposed crystal surfaces and particular shapes (Methods)[22]. To make the nanoparticles more stable under an electron beam, a thin layer of carbon (~1-2 nm) was deposited on the nanoparticles (Methods). Using HAADF-STEM[14], we acquired a tilt series of projections from a Pt nanoparticle (Methods). Supplementary Figs. 1 and 2 shows the tilt series of 104 projections with equal sloped increments and a tilt range of ±72.6°. To monitor beam induced changes to the Pt nanoparticle, three 0° projections were measured during the acquisition of the tilt series (Supplementary Fig. 3). The consistency of these projections indicates that the lattice structure of the nanoparticle was stable throughout the experiment.

After background subtraction and CM alignment (Methods), the tilt series was reconstructed by the EST method[20,23-26] (Methods). Figs. 1a and c show the 3D Fourier transform of the reconstruction and a 2.6 Å thick central slice in the XY plane, where the

electron beam is along the Z-axis. However, due to the low signal to noise ratio (SNR) in the EST reconstruction (Fig. 1c) and noise among the Bragg peaks (Fig. 1a), 3D dislocations within the nanoparticle cannot be identified at atomic resolution. To enhance the SNR of the reconstruction, we developed a 3D Bragg peak filtering method to identify all the measurable 3D Bragg peaks and their distributions (Methods). Fig. 1b shows the 3D Fourier transform of the reconstruction after 3D Bragg peak filtering, in which the red and black dots represent the {111} and {200} peaks of the Pt nanoparticle, respectively. By applying an inverse Fourier transform to the identified 3D Bragg peaks and multiplying it by the 3D boundary of the Pt nanoparticle determined from the EST reconstruction, we obtained the 3D structure of the nanoparticle with a size of ~11.2×10.7×7.1nm $nm^3$. Supplementary Movie 1 and Fig. 1d show 3D volume renderings and a 2.6 Å thick central slice in the XY plane of the Pt nanoparticle, in which nearly all the atoms are visible.

To verify the 3D Bragg peak filtering method, we performed a comparison with a 3D Wiener filter using the same experimental data. The Wiener filter is well established for reducing the amount of noise present in a signal and is applied to TEM images[27]. Supplementary Figs. 5b-d show the 2.6 Å thick central slice in the XY plane of the reconstruction after applying a 3D Wiener filter $S^2/(S^2+\lambda n^2)$ where S is an estimate of the signal, n the noise with $\lambda$ = 1, 2 and 3. Supplementary Figs. 5f-j show zoomed views of four regions for the raw reconstruction, and the reconstructions with the 3D Wiener filter ($\lambda$ = 1, 2 and 3) and the 3D Bragg peak filter. While the result with the $\lambda$ = 1 Wiener filter is nosier, the atomic positions in the reconstructions using the $\lambda$ = 2 and 3 Wiener filter and the 3D Bragg peak filter are consistent.

To further examine the 3D Bragg peak filtering method, we performed numerical simulations on a 7.3×7.0×4.5 $nm^3$ decahedral Pt nanoparticle with multislice calculations.

The Pt particle consists of a total of 4015 atoms with edge and screw dislocations (Supplementary Figs. 6a-c, 7a and b). A tilt series of 63 projections with a tilt range of ±72.6° and equal slope increments was calculated by multislice STEM simulations (Supplementary Fig. 8). Two levels of Poisson noise were added to the projections of the tilt series with a total electron dose of $2.52\times10^5$ e/Å$^2$ and $5.67\times10^4$ e/Å$^2$, corresponding to $R_{noise}$ (Methods) of 10% and 20%, respectively. The two tilt series were aligned and reconstructed by the CM and EST methods[20,23-26] (Methods, Supplementary Figs. 6d-f and j-l). Due to the low SNR in the reconstructions, not all the atoms or dislocations are visible in the raw 3D reconstructions, especially with $R_{noise}$ = 20% (Supplementary Figs. 6j-l). After applying a 3D Bragg peak filter to the raw reconstructions (Methods), we obtained the 3D structure of the simulated Pt nanoparticle with all the atoms resolved (Supplementary Figs. 6g-i and m-o). Furthermore, 3D grain boundaries, as well as edge and screw dislocation core structures were determined at atomic resolution and are consistent with those in the model (Supplementary Figs. 6g-i, 6m-o and 7c-f).

After verifying 3D Bragg peak filtering with a 3D Wiener filter and multislice simulation data, we analyzed 3D dislocations of the Pt nanoparticle obtained from the experimental tilt series. Fig. 2 shows grain boundary comparisons between a 2D experimental projection and 2.6 Å thick internal slices of the reconstructed particle. The experimental projection in the XY plane suggests that this is a decahedral multiply-twinned nanoparticle[28] and twin boundaries are flat (Fig. 2a and Supplementary Fig. 9). However, a 2.6 Å thick internal slice in the XY plane and a zoomed view indicate the existence of atomic steps at the twin boundaries (Figs. 2b and 2c) that are hidden in the projection (Fig. 2a). Figs. 2d and 2e show zoomed views of a twin boundary in a 2.6 Å thick slice above and below the slice of Fig. 2b, revealing that the atomic steps vary in consecutive atomic layers. These atomic steps are also independently verified by applying 3D Wiener filtering

to the same experimental data (Supplementary Fig. 10). In addition, subgrain boundaries in the 2.6 Å thick internal slice (Fig. 2b) are widened by two lattice spacings relative to those in the projection (Fig. 2a). Fig. 2f shows a zoomed view of a stacking fault in the 2.6 Å thick internal slice ending at a twin boundary, which is in good agreement with the classical model for an extrinsic stacking fault[1] (inset in Fig. 2f).

Besides twin boundaries, subgrain boundaries and stacking faults, we also observed the 3D core structure of edge and screw dislocations at atomic resolution in the Pt nanoparticle. Figs. 3a and b show a 7.9 Å thick internal slice of the nanoparticle and a zoomed view of an edge dislocation, where red dots label the position of atoms. By computationally 'sectioning' through the 7.9 Å thick slice, we obtained three consecutive atomic layers each with 2.6 Å thick (Figs. 3c-e). The three consecutive atomic layers indicate the dislocation line is in the $[10\bar{1}]$ direction, and the Burgers vector of the edge dislocation was determined to be $\frac{1}{2}[101]$ (Fig. 3c). To visualize a screw dislocation, a 5.3 Å thick slice (two atomic layers) in the $(\bar{1}11)$ plane was selected (Supplementary Fig. 11b) and then tilted to the $[011]$ direction (Fig. 4a). Fig. 4b shows a zoomed view of the slice where the zigzag pattern, a characteristic feature of a screw dislocation, is visible. To better visualize the screw dislocation, we display surface renderings of the zoomed region (Fig. 4c) where the atoms in green are on the top layer and those in red in the bottom layer. The zigzag pattern is more clearly visualized in the surface renderings, in which the green line connects the atoms on the top layer and the red line for the atoms in the bottom layer. The Burgers vector of the screw dislocation was determined to be $\frac{1}{2}[01\bar{1}]$, and the width of the screw dislocation was estimated to be ~8.9 Å which is consistent with the high resolution TEM results for Au and Ir[29]. Careful analysis of the position of the screw dislocation inside

the Pt nanoparticle suggests that the screw dislocation is associated with atomic steps at a twin boundary (Supplementary Fig. 11)

While it is often thought that nanoparticles cannot support dislocations, this is not the case for multiply-twinned particles such as the decahedral one imaged here. These contain a ~2% angular strain, a disclination and at larger sizes this can in principle be relieved by dislocations[28]. A recent analysis implied that about 1/3 of this strain is accommodated at the twin boundaries[30], but as a 2D projection method was not able to explain this further. Our results strongly suggest that the twin boundaries are not flat, and dislocations associated with atomic steps at the boundaries account for the strain relaxation (Supplementary Fig. 11).

In conclusion, by combining a 3D Bragg peak filtering method with an EST reconstruction, we determined the 3D structure of a polycrystalline Pt nanoparticle at atomic resolution. We observed the existence of atomic steps along twin boundaries in three dimensions that are hidden in the projections of the Pt nanoparticle. We also imaged the 3D core structure of edge and screw dislocations in the nanoparticle at atomic resolution. The significance of this work is twofold. First, 3D atomic resolution imaging of dislocations allows us to observe new structural information that is not visible in conventional 2D projections, which is expected to advances our fundamental understanding of dislocations in materials. Second, while discrete tomography, through the use of *a priori* information, has been applied to reconstruct 3D surface morphology of a small crystalline nanoparticle at atomic resolution[31], EST based electron tomography in combination with 3D Bragg peak filtering represents a general method for 3D atomic resolution imaging of the local structure in nanomaterials. Furthermore, although nanoparticles are used in this study, this method can, in principle, be applied to 3D imaging of thin materials at high resolution whereas the thickness of the materials is only limited by dynamical electron scattering.

# Methods Summary

Pt nanoparticles were synthesized by using facet-specific peptide sequences[22] and supported on 5 nm thick silicon nitride membranes. To stabilize the nanoparticles under a STEM beam, a thin layer of carbon was deposited on the Pt nanoparticles and the electron energy was kept below the knock-on radiation damage threshold of Pt. Using HAADF-STEM (energy: 200 keV; spherical aberration: 1.2 mm; illumination semi-angle: 10.7 mrad; detector inner and outer angles: 35.2 and 212.3 mrad), a tilt series of 104 projections was acquired from a Pt nanoparticle with equal sloped increments[20] and a tilt range of ±72.6°. To monitor beam induced changes to the nanoparticle, three 0° projections were measured during the acquisition of the tilt series, indicating the Pt nanoparticle was stable throughout the experiment. After performing background subtraction and CM alignment for the tilt series, a 3D reconstruction of the nanoparticle was obtained by using the EST method[20,23-26]. However, 3D dislocations of the nanoparticle cannot be identified in the raw 3D reconstruction at atomic resolution. To enhance the SNR in the reconstruction, we developed a 3D Bragg peak filtering method to identify all the measurable 3D Bragg peaks. The 3D Fourier transform of the EST reconstruction consists of {111} and {200} Bragg peaks. We first determined a 2-shell volume with all the measurable Bragg peaks and set other voxels to zero. We then chose the highest intensity {111} Bragg peak as a reference peak. After optimizing the threshold based on the reference peak (Supplementary Fig. 4), we obtained a 3D mask to retain the 3D intensity and shape distribution of Bragg peaks and reduce noise among the peaks (Fig. 1b). After applying the inverse Fourier transform to the identified 3D Bragg peaks, the 3D structure of the Pt nanoparticle was obtained in which nearly all the atoms are visible.

# References


1. Hull, D. & Bacon, D. J. *Introduction to Dislocations* 5th ed. (Butterworth-Heinemann, 2011).
2. Smith, W. F. & Hashemi, J. *Foundations of Materials Science and Engineering* 4th ed. (McGraw-Hill Science, 2005).
3. Nakamura, S. The Roles of Structural Imperfections in InGaN-Based Blue Light-Emitting Diodes and Laser Diodes. *Science* **281**, 956-961 (1998).
4. Hua, G. C. *et al*. Microstructure study of a degraded pseudomorphic separate confinement heterostructure blue-green laser diode. *Appl. Phys. Lett.* **65**, 1331-1333 (1994).
5. Hirsch, P. B., Horne, R. W. & Whelan, M. J. LXVIII. Direct observations of the arrangement and motion of dislocations in aluminium. *Philos. Mag*. **1,** 677-684 (1956).
6. Bollmann, W. Interference Effects in the Electron Microscopy of Thin Crystal Foils. *Phys. Rev*. **103**, 1588–1589 (1956).
7. Menter, J. W. The Direct Study by Electron Microscopy of Crystal Lattices and their Imperfections. *Proc. R. Soc. Lond.* A **236**, 119-135 (1956).
8. Howie, A. & Whelan, M. J. Diffraction Contrast of Electron Microscope Images of Crystal Lattice Defects. III. Results and Experimental Confirmation of the Dynamical Theory of Dislocation Image Contrast. *Proc. R. Soc. Lond. A* **267**, 206-230 (1962).
9. Hirsch, P. B., Cockayne, D. J. H., Spence, J. C. H. & Whelan, M. J. 50 Years of TEM of Dislocations: Past, Present and Future. *Philos. Mag*. **86**, 4519–28 (2006).

10. Spence, J. C. H. *Experimental High-Resolution Electron Microscopy* 3rd ed. (Oxford University Press, New York, 2003).

11. Chisholm, M. F. & Pennycook, S. J. Structural origin of reduced critical currents at $YBa_2Cu_3O_{7-\delta}$ grain boundaries. *Nature* **351**, 47-49 (1991)

12. Ludwig, W. *et al*. Three-dimensional imaging of crystal defects by `topo-tomography'. *J. Appl. Crystallogr*. **34**, 602-607 (2001).

13. Cockayne, D. J. H., Ray, I. L. F. & Whelan, M. J. Investigations of dislocation strain fields using weak beams. *Philos. Mag*. **20**, 1265-1270 (1969).

14. Pennycook, S. J. & Nellist, P. D. *Scanning Transmission Electron Microscopy: Imaging and Analysis* 1st ed. (Springer, 2011).

15. Barnard, J. S., Sharp, J., Tong, J. R. & Midgley, P. A. High-Resolution Three-Dimensional Imaging of Dislocations. *Science* **313**, 319 (2006).

16. Midgley, P. A. & Weyland, M. STEM Tomography. In *Scanning Transmission Electron Microscopy: Imaging and Analysis*. ed. Pennycook, S. J. & Nellist, P. D. pp. 353-392 (Springer, 2011).

17. Kelly, T. F. & Miller, M. K. Atom probe tomography. *Rev. Sci. Instrum*. **78**, 031101 (2007).

18. Xin, H. L., Ercius, P., Hughes, K. J., Engstrom, J. R. & Muller, D. A. Three-dimensional imaging of pore structures inside low- dielectrics. *Appl. Phys. Lett.* **96**, 223108 (2010).

19. Bar Sadan, M. *et al.* Toward atomic-scale bright-field electron tomography for the study of fullerene-like nanostructures. *Nano Lett*. 8, 891-896 (2008).

20. Scott, M. C. *et al.* Electron tomography at 2.4 Å resolution. *Nature* 483, 444–447 (2012).

21. Howie, A. Diffraction channelling of fast electrons and positrons in crystals. *Phil. Mag.* **14**, 223-237 (1966).

22. Chiu, C. Y. *et al*. Platinum nanocrystals selectively shaped using facet-specific peptide sequences. *Nature Chem.* **3**, 393-399 (2011).

23. Miao, J., Föster, F. & Levi, O. Equally sloped tomography with oversampling reconstruction. *Phys. Rev. B* **72**, 052103 (2005).

24. Lee, E. *et al*. Radiation dose reduction and image enhancement in biological imaging through equally sloped tomography. *J. Struct. Biol.* **164**, 221–227 (2008).

25. Fahimian, B. P., Mao, Y., Cloetens, P., & Miao, J. Low dose X-ray phase-contrast and absorption CT using equally-sloped tomography. *Phys. Med. Biol.* **55**, 5383-5400 (2010).

26. Zhao, Y. *et al.* High resolution, low dose phase contrast x-ray tomography for 3D diagnosis of human breast cancers. *Proc. Natl. Acad. Sci. USA* **109**, 18290-18294 (2012).

27. Marks, L. D. Wiener-filter enhancement of noisy HREM images. *Ultramicroscopy* **62**, 43-52 (1996).

28. Howie, A. & Marks, L. D. Elastic strains and the energy balance for multiply twinned particles, *Philos. Mag.* A **49**, 95-109 (1984).

29. Balk, T. J. & Hemker, K. J. High resolution transmission electron microscopy of dislocation core dissociations in gold and iridium. *Philos. Mag.* A **81**, 1507-1531 (2001).

30. Johnson, C. L. J. *et al.* Effects of elastic anisotropy on strain distributions in decahedral gold nanoparticles. *Nature Materials* **7**, 120-124 (2008).

31. Van Aert, S., Batenburg, K. J., Rossell, M. D., Erni, R. & Van Tendeloo, G. Three-dimensional atomic imaging of crystalline nanoparticles. *Nature* **470**, 374–377 (2011).

# Methods

**Definition of $R_{noise}$.** An R-factor was used to defined the level of Poisson noise in each multislice simulation tilt series,

$$R_{noise}^{\theta} = \frac{\sum_{x,y} \left| P_{noise}^{\theta}(x, y) - P_{simulated}^{\theta}(x, y) \right|}{\sum_{x,y} P_{simulated}^{\theta}(x, y)} \qquad (1)$$

where $P_{simulated}^{\theta}(x, y)$ is the projection calculated from multislice STEM simulations at angle θ, and $P_{noise}^{\theta}(x, y)$ is the same projection with Poisson noise added. After computing $R_{noise}^{\theta}$ for each projection, we calculated $R_{noise}$ by averaging $R_{noise}^{\theta}$ for all the projections.

**Synthesis of Pt nanoparticles.** The Pt nanoparticles were synthesized by peptides in aqueous solution at room temperature as reported previously[22]. All regents were dissolved in water before using. A pre-prepared vial containing precursor (chloroplatinic acid hydrate ($H_2Pt(IV)_{Cl6}.xH_2O$, 1 mM) and S7 peptide (Ser-Ser-Phe-Pro- Gln-Pro-Asn) solution (30 mg/ ml) were mixed with ascorbic acid (2 mM) immediately before injection of fresh $NaBH_4$ (0.8 mM) where $NaBH_4$ and ascorbic acid were used as reducing agents. The final volume of the reaction solution was 5 ml, and the reaction normally required more than 30 minutes.

**Sample preparation**. Pt nanoparticles were deposited on a 5-nm-thick silicon nitride membrane. The membrane, with a size of 100 m × 1500 m, is supported on a 100 m thick silicon frame (TEMwindows.com). To dissipate charge efficiently and make the nanoparticles more stable under an electron beam, a premium high-temperature ultrathin carbon coating (TEMwindows.com) was applied to the nanoparticles based on the

following procedure. The silicon nitride membrane grid was first placed into a vacuum chamber with the temperature ramping up from 300°C to 700°C at a rate of 10°C/s. The carbon was coated during a 5 minute soak at 700°C. The chamber then naturally cooled to 450°C over the next 5 minutes before the grid being removed. The silicon nitride membrane grid was finally loaded on a tomographic sample holder (Fischione Model 2020) for data acquisition.

**Acquisition of tomographic tilt series using HAADF-STEM**. STEM images of the Pt nanoparticles were acquired on a FEI Titan 80-300 microscope (energy: 200 keV; spherical aberration: 1.2 mm; illumination semi-angle, 10.7 mrad). The 100pA electron beam was focused to a probe with a 50 m probe-forming aperture (C2) and rastered over the sample. The scattered electrons were captured by a Fischione Model 3000 HAADF detector with angles between 35.2 and 212.3 mrad from the optical axis. The use of HAADF angles was to reduce the nonlinear intensities and diffraction contrast in the images. The maximum tilt angles were limited by the holder to ±75°. To reduce vibration and drift during data acquisition, the sample holder was allowed to settle for one hour after insertion into the microscope and also for several minutes after moving to each new angle. Tilt series were manually acquired by changing the angle with equal slope increments[20,23-26]. When focusing an image, a nearby nanoparticle was first viewed (not the particle of interest), thus reducing the unnecessary radiation dose to the particle under study[19]. Using this low exposure acquisition scheme, a tomographic tilt series of 104 projections with equal sloped increments and a tilt range of ±72.6° was acquired from a Pt nanoparticle. The probe current was ~100 pA with a dwell time of 48 s per pixel, and the magnification of each projection was $3.6\times10^6$. The total electron dose of the tilt series was estimated to be ~$2.5\times10^7$ e/Å$^2$. Since the pixel size in STEM mode may vary, a calibration image of an

oriented single crystal Au foil (Ted Pella) was taken in STEM mode under the same conditions, and the STEM pixel size was characterized to be 0.35 Å. To enhance the SNR in the projections of the tilt series, 1.5×1.5 pixel binning was performed for each projection. The pixel size of the binned projections is 0.53 Å.

**Background subtraction and CM alignment.** In order to use the EST iterative algorithm, background subtraction has to be performed for each projection. We implemented background subtraction and CM alignment based on the following procedure. First, we selected the 0° projection and chose a suitable cut-off value to subtract its background. After projecting the 0° projection onto the Y axis (i.e. the tilt axis) to obtain a 1D curve, we calculated the center of mass of the 1D curve ($Y_{cm}$), and set $Y_{cm}$ as the origin of the Y-axis. This 1D curve was used as a reference curve. Second, we optimized the background subtraction for other projections based on the reference curve. We scanned the cut-off values from 0.5 to 1.5 times of the mean value of each projection with an increment of 0.01. For each cut-off value, we projected the projection onto the Y axis to obtain a 1D curve. By shifting the 1D curve pixel by pixel along the Y axis, we calculated the difference between the 1D curve and the reference curve. We recorded the smallest difference and the corresponding shift for each 1D curve. After scanning through all the cut-off values, we plotted the smallest differences verse the cut-off values which should form a U-shape curve. We picked up the minimum corresponding to the optimized cut-off value and shift of a given projection. After performing background subtraction with the optimized cut-off values, we calculated the center of mass ($Y_{CM}$) for all the 1D curves. If not all of them ( *i.e.* rounded $Y_{CM}$ ) are at the origin, we adjusted the cut-off value for the 0° projection (i.e. the reference curve) and repeated the above steps until achieving the best agreement. Finally, after performing background subtraction and aligning the projections along the Y axis, we

projected all the projections onto the X axis. We calculated the center of mass ($X_{CM}$) for all 1D curves, and set $X_{CM}$ as the origin of the X axis[20]. After repeating this process, all the projections were aligned to the tilt axis.

**EST reconstruction.** The EST iterative algorithm started with an estimated 3D rectangular loose support that is larger than the true boundary of the structure to be reconstructed. The algorithm then iterated back and forth between real and reciprocal space. In real space the voxel values outside the support and the negative voxel values inside the support were set to zero, while in reciprocal space the Fourier slices calculated from measured projections were retained in each iteration (the details of the EST algorithm can be found in refs. 20,23-26). Each iteration was monitored by an error metric, defined as the difference between the measured and calculated Fourier slices, and the algorithm was terminated after reaching a maximum number of iterations. Using the iterative EST algorithm, a preliminary 3D reconstruction was obtained after 500 iterations. An updated 3D support was determined by convolving the reconstruction with a Gaussian window and selecting a suitable cut-off. The 3D shape of the support was also double-checked by examining the reconstruction slice-by-slice to ensure the support does not crop the structure. Using the updated support, we performed another 500 iterations to obtain a new reconstruction. Besides the above mentioned procedure to improve the support, we also projected the reconstruction back to calculate projections at given angles. By computing the cross-correlation between the calculated and measured projections, we further adjusted the alignment of the projections to achieve maximum consistency in 3D reconstruction. Usually the shift should be 1 pixel or smaller in each dimension. Otherwise, the data analysis and CM alignment procedure has to be re-done. We then repeated the procedure of improving the support and backprojection

alignment. The final reconstruction was obtained when no further improvements can be made.

**3D Bragg peak filtering.** Due to dynamical scattering effects[21], the missing wedge problem[16,18,20] and Poisson noise in the tilt series, not all the atoms or dislocations are visible in the raw 3D EST reconstruction. To enhance the SNR in the reconstruction, we developed a 3D Bragg peak filtering method to identify all the measurable 3D Bragg peaks and reduce noise among the Bragg peaks. Compared to 2D Fourier filtering approaches[32-34], the atomic scale resolution EST reconstruction allowed us to develop a more accurate 3D Bragg peak filtering method with the following procedure. First, the 3D Fourier transform of the raw reconstruction of the Pt nanoparticle consist of two sets of lattice planes {111} and {200}. The intensities of the {111} peaks were estimated to be several times higher than those of the {200} peaks. We calculated the average radial distance ($d$) between the {111} and {200} peaks. Two radii were then determined by $R_{in} = R_{111} - d$ and $R_{out} = R_{200} + d$, where $R_{111}$ and $R_{200}$ are the average radial distance for the {111} and {200} peaks, respectively. By keeping those voxels in the 3D Fourier transform with their radii between $R_{in}$ and $R_{out}$, and setting other voxels to zero, we obtained a 2-shell volume including all the measurable 3D Bragg peaks. Next, we implemented a method to further reduce noise among the Bragg peaks within the 2-shell volume. We chose the highest intensity {111} Bragg peak as a reference peak and calculated thresholds based on the reference peak. We scanned through the thresholds from 1% to 20% of the reference peak with 1% per step. For each threshold, we set those voxels with values larger than the threshold to one and the other voxels to zero, and obtained a 3D mask. The 3D mask was convolved with a 3 voxel diameter sphere to compute a new 3D mask where the convolution process was to retain the 3D shape of each Bragg peak. By multiplying the new 3D mask with the Fourier transform

of the raw reconstruction, we obtained a new 3D Fourier transform. By monitoring the change of noise among the Bragg peaks, we found that a threshold with 10% of the reference peak is large enough to remove noise among the 3D Bragg peaks, while retaining all the measurable {111} and {200} peaks (Fig. 1b and Supplementary Fig. 4). Care should be taken that the optimized threshold of 10% of the reference peak obtained here may vary for different samples. Finally, by applying the inverse Fourier transform to the identified Bragg peaks and multiplying it by a 3D shape (i.e. a tight support) obtained from the EST reconstruction, we obtained the 3D structure of the Pt nanoparticle (Movie 1 and Fig. 1d). We have further confirmed the 3D Bragg peak filtering method by performing a comparison with a 3D Wiener filter on the same experimental data[35] (Supplementary Figs. 5 and 10) as well as using multislice numerical simulations[36] (Supplementary Figs. 6-8).


32. Saxton, W. O. *Computer Techniques for Image Processing in Electron Microscopy* (Academic Press, New York, 1978).
33. Hawkes P. W. *Computer Processing of Electron Microscope Images* (Springer, Berlin, 1980).
34. Möbus, G., Necker, G. & Rühle, M. Adaptive Fourier-filtering technique for quantitative evaluation of high-resolution electron micrographs of interfaces. *Ultramicroscopy* **49**, 46-65 (1993).
35. Brown, R. G. & Hwang, P. Y. C. *Introduction to Random Signals and Applied Kalman Filtering* 3rd ed. (New York: John Wiley & Sons, 1996).
36. Kirkland, E. J. *Advanced Computing in Electron Microscopy* 2nd ed. (Springer, 2010).

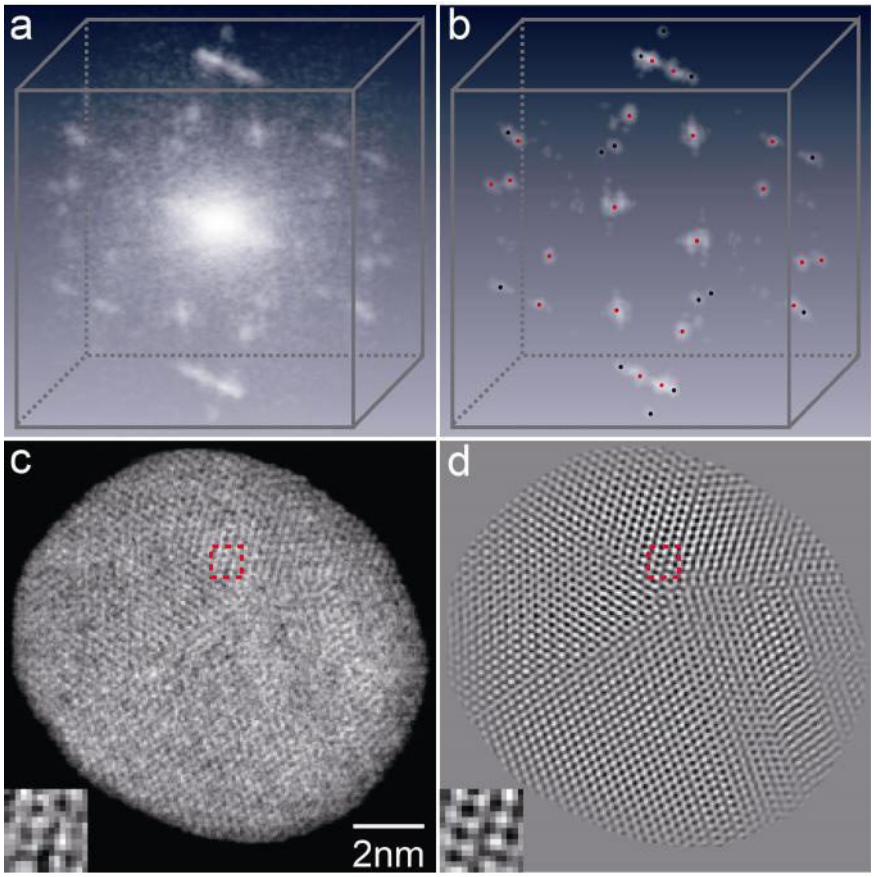


**Figure 1**. 3D reconstruction of a polycrystalline Pt nanoparticle before and after applying a 3D Bragg peak filter. **a**, 3D Fourier transform of the raw reconstruction of the nanoparticle. **b**, 3D Fourier transform of the reconstruction after 3D Bragg peak filtering where the {111} and {200} Bragg peaks are labelled with red and black dots, respectively. **c**, A 2.6 Å thick central slice in the XY plane of the raw reconstruction, where the Z-axis is along the beam direction **d**, The same slice of the 3D structure after applying a 3D Bragg peak filter, in which nearly all the atoms (in white) are visible. The clear boundary of the nanoparticle is due to the multiplication of the 3D structure with a 3D shape obtained from the EST reconstruction (Methods). The insets show a zoomed region of the atomic positions before and after applying a 3D Bragg peak filter.

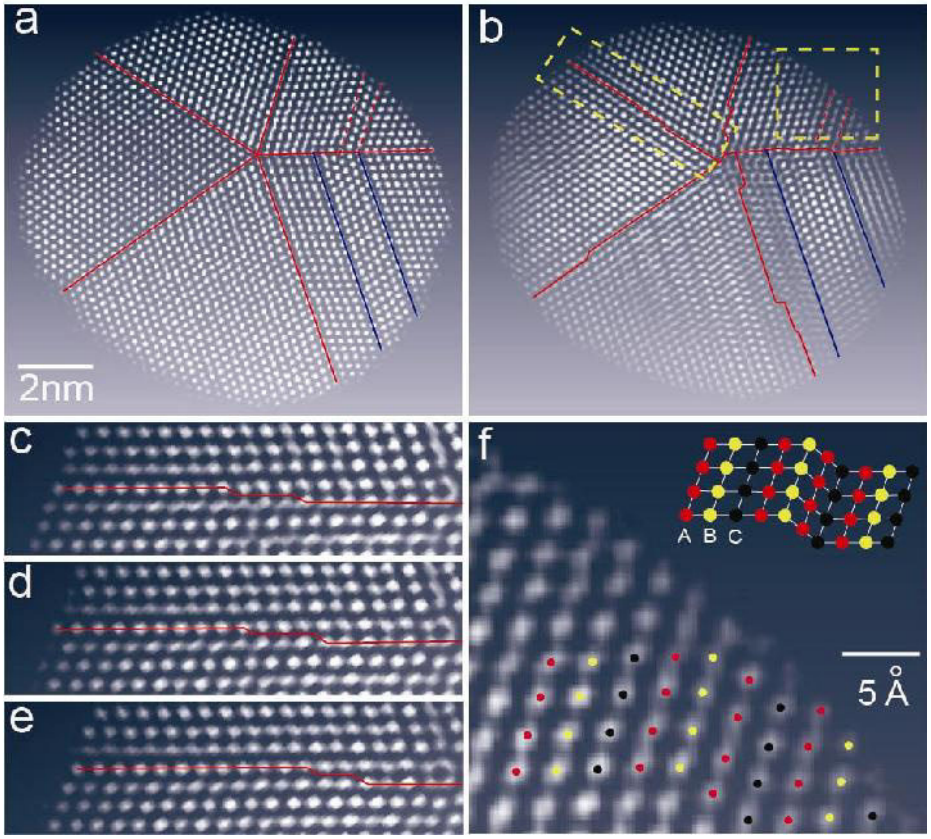


**Figure 2**. Grain boundary comparisons between a 2D experimental projection and several 2.6 Å thick internal slices of the reconstructed Pt nanoparticle. **a**, Experimental projection in the XY plane suggesting this is a decahedral multiply-twinned nanoparticle and twin boundaries (red lines) are flat. Blue lines show two subgrain boundaries. To enhance the image contrast, a 2D Fourier filter was applied to the projection. **b**, A 2.6 Å thick internal slice indicating the existence of atomic steps at the twin boundaries (red lines). The subgrain boundaries (blue lines) are widened by two lattices spacings relative to those in (**a**). **c**, Zoomed view of a twin boundary in (**b**). **d**, and **e**, a 2.6 Å thick slice above and below the slice of (**c**), revealing that the atomic steps vary in consecutive atomic layers. **f**, Zoomed view of a stacking fault in the 2.6 Å thick internal slice, which is in good agreement with the classical model for an extrinsic stacking fault (inset). The images as well as those in Figs. 3 and 4 are displayed with Amira.

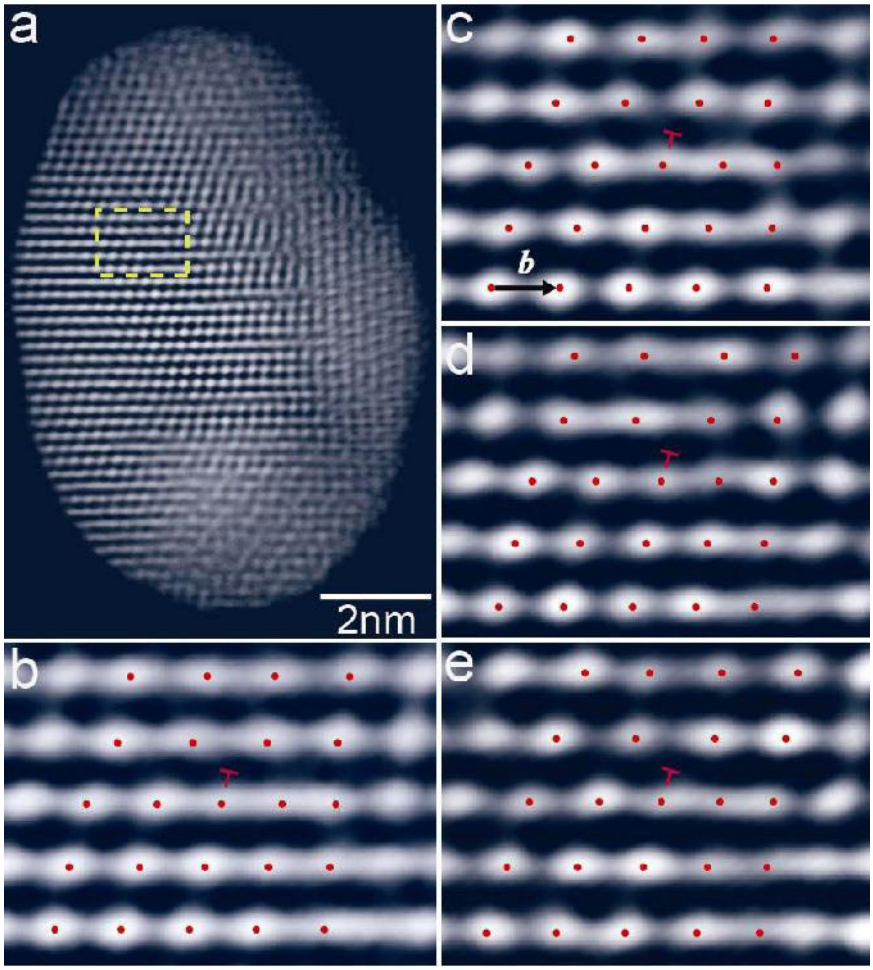


**Figure 3**. Observation of the 3D core structure of an edge dislocation at atomic resolution. **a**, A 7.9 Å thick internal slice of the nanoparticle. The lattice structure on the left and at the bottom parts of the slice is not well defined mainly because this decahedral multiply-twinned nanoparticle consists of five grains with different orientations. **b**, A zoomed view of an edge dislocation in (**a**) where red dots represent the position of the atoms. **c**, **d** and **e**, 2.6 Å atomic layers sectioning through the slice of (**b**). The three consecutive atomic layers indicate the dislocation line is in the direction of $[10\bar{1}]$. The Burgers vector (***b***) of the edge dislocation was determined to be $\frac{1}{2}[101]$.

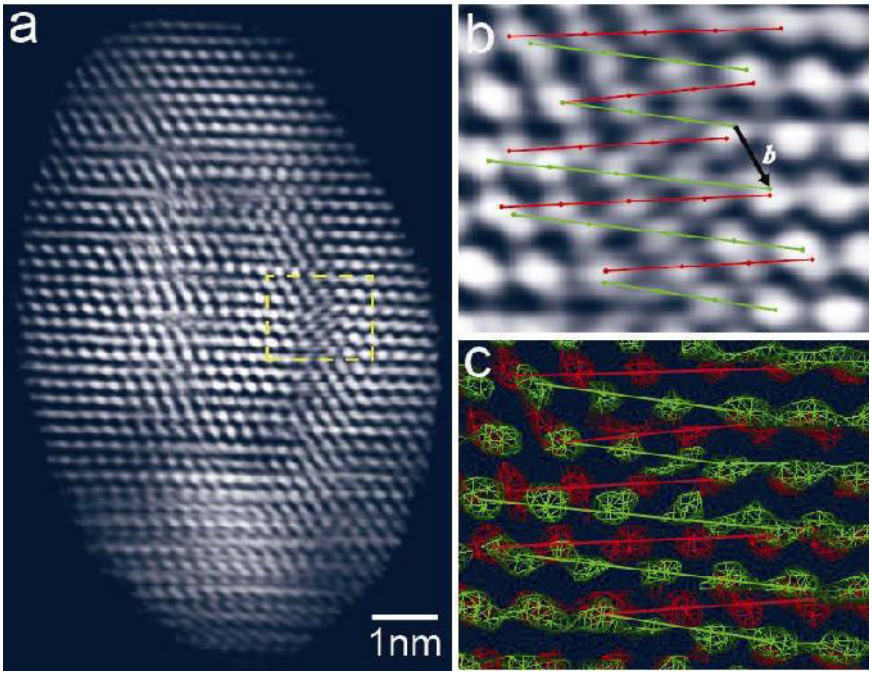


**Figure 4**. Observation of the 3D core structure of a screw dislocation at atomic resolution. **a**, Volume renderings of a 5.3 Å thick slice (two atomic layers) in the $(\bar{1}11)$ plane (Supplementary Fig. 11b), tilted to the $[011]$ direction in order to visualize the zigzag pattern, a characteristic feature of a screw dislocation. **b**, Zoomed view of a screw dislocation showing the zigzag pattern. **c**, Surface renderings of the screw dislocation where the atoms in green are on the top layer and those in red in the bottom layer. The zigzag pattern is more clearly visualized, the Burgers vector (***b***) of the screw dislocation was determined to be $\frac{1}{2}[01\bar{1}]$, and the width of the screw dislocation was estimated to be ~8.9 Å.

# Supplementary Information

## Supplementary Figures

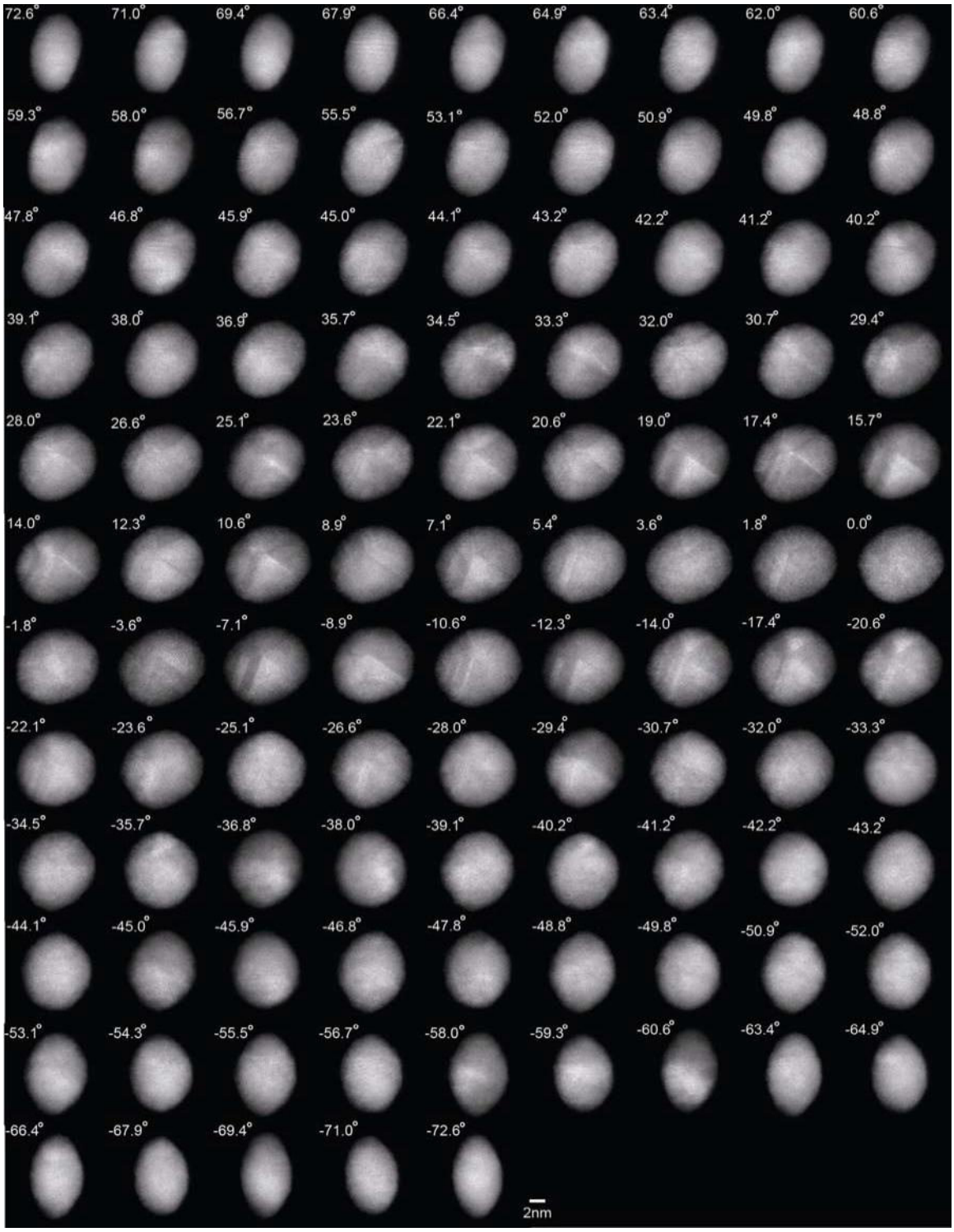

**Supplementary Figure 1.** Experimental tilt series of 104 projections with a tilt range of ±72.6° and equal slope increments, acquired from a Pt nanoparticle using HAADF-STEM (energy: 200 keV; spherical aberration: 1.2 mm; illumination semi-angle: 10.7 mrad; detector inner and outer angles: 35.2 and 212.3 mrad; pixel size: 0.35 Å). The total electron dose of the tilt series was estimated to be ~$2.5\times10^{7}$ e/Å$^{2}$. Careful examination of the projections indicates that the facets of this nanoparticle are not sharply defined


**Supplementary Figure 2.** Fourier transforms of the 104 projections (Supplementary Fig. 1), in which Bragg peaks are visible in most projections.

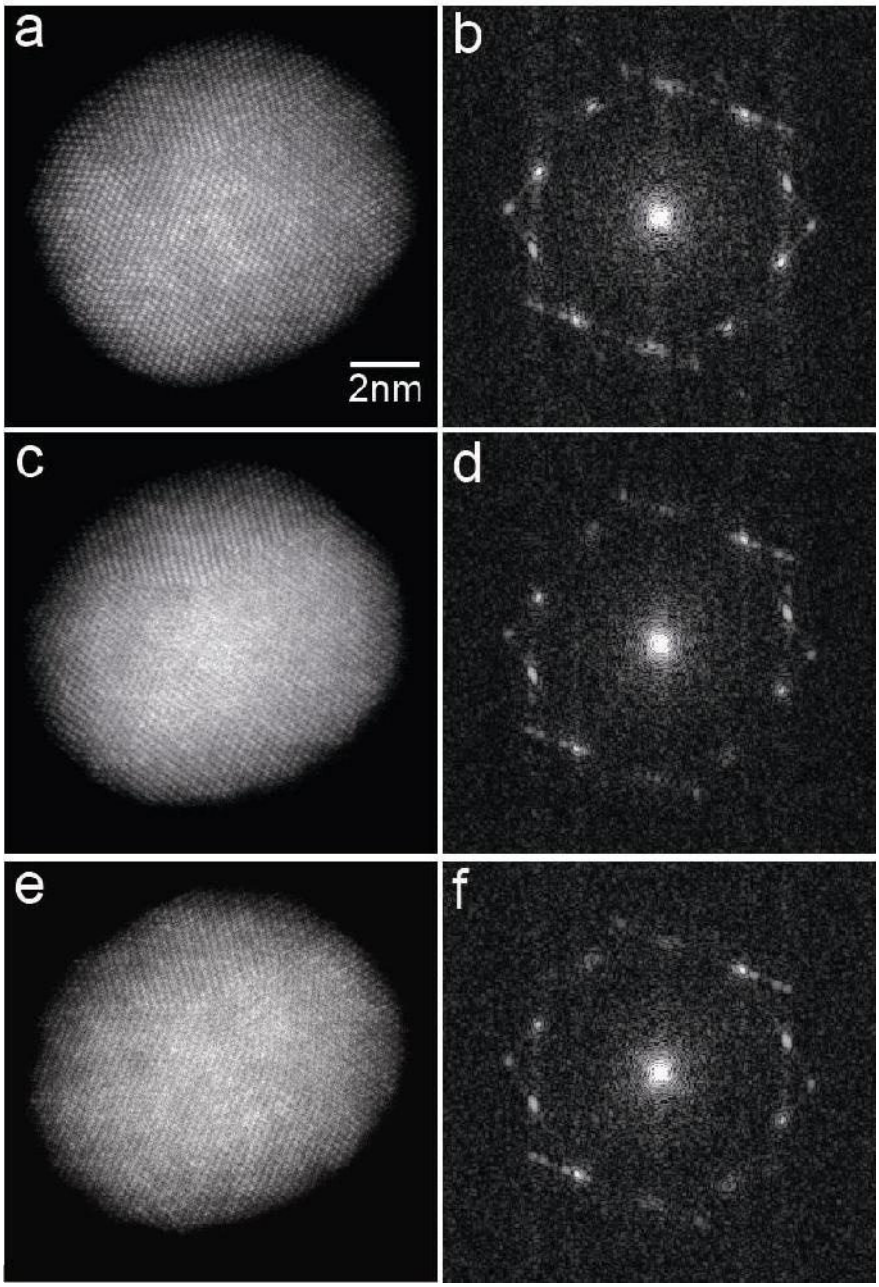


**Supplementary Figure 3.** Three 0° projections (**a**,**c**,**e**) and their Fourier transforms (**b**,**d**,**f**) measured during the acquisition of the tilt series (Supplementary Fig. 1) to monitor beam induced changes to the Pt nanoparticle. While there some small surface structural changes among the three projections, the lattice structure of the nanoparticle was consistent throughout the experiment.

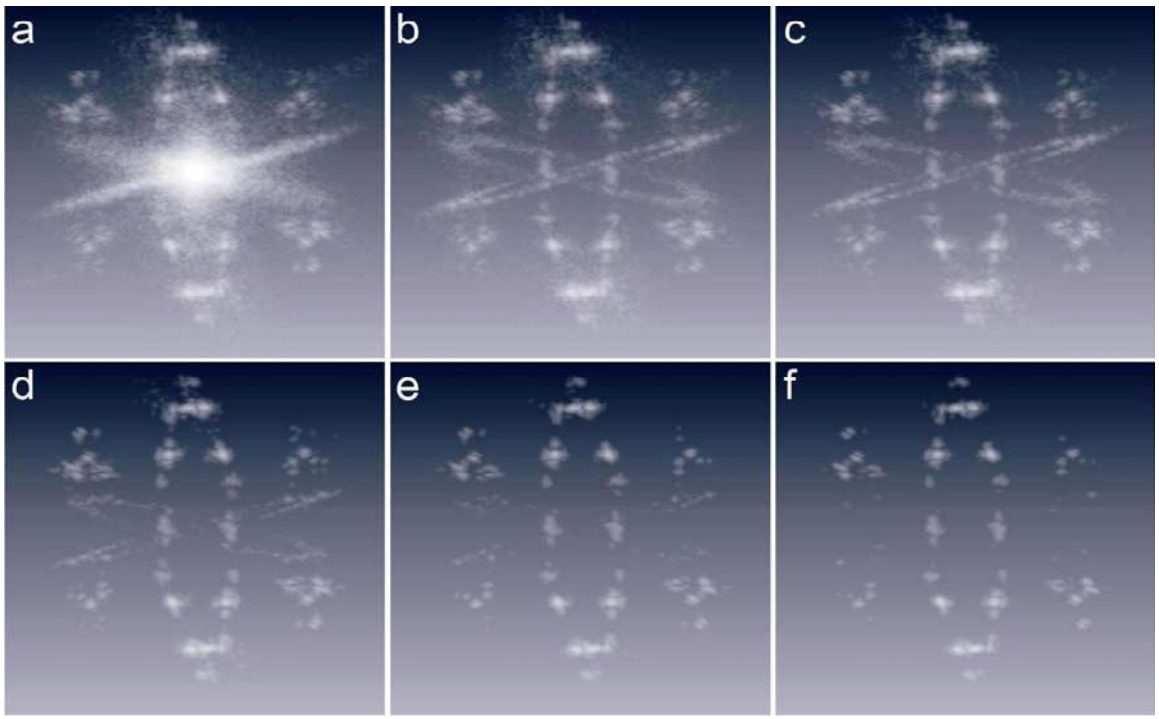


**Supplementary Figure 4.** 3D Bragg peak filtering of the EST reconstruction of the Pt nanoparticle. **a-f**, 3D Fourier transforms of the reconstruction after applying a 3D Bragg peak filter with varying thresholds: (**a**) 5%, (**b**) 6%, (**c**) 7%, (**d**) 8%, (**e**) 9% and (**f**) 10% of the highest intensity {111} Bragg peak in which the central peak has been filtered out (Methods). For each threshold, we set those voxels with values larger than the threshold to one and the other voxels to zero, and obtained a 3D mask. After convolving the 3D mask with a 3 voxel diameter sphere, we obtained a new 3D mask to identify the 3D intensity and shape distribution of the Bragg peaks. When the threshold was set to be ~10% (**f**), most of noise among the Bragg peaks is removed, while the 3D intensity and shape distribution of the Bragg peaks are retained. Cross-streak noise in the images is due to the missing wedge problem. Although the EST method can significantly alleviate the missing wedge problem, it cannot completely solve it[20]. Care should be taken that the optimized threshold of 10% of the reference peak obtained here may vary for different samples.

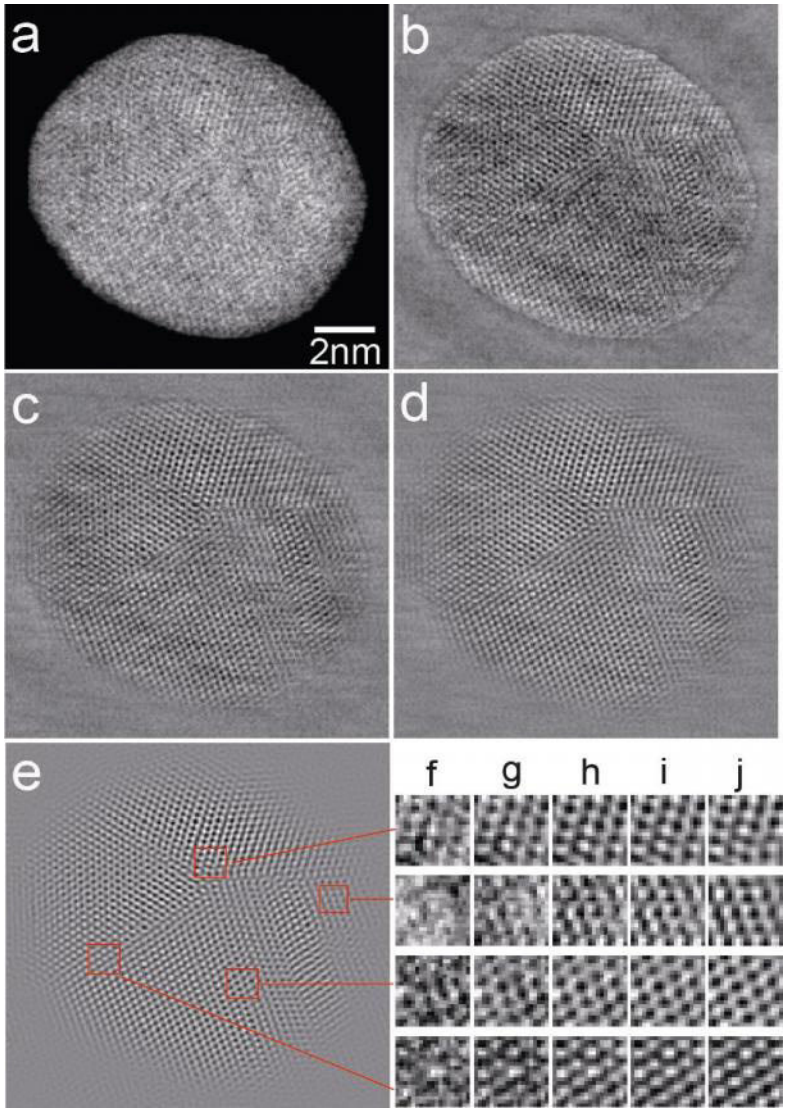


**Supplementary Figure 5.** Comparison between 3D Wiener and 3D Bragg peak filtering. **a-e**, 2.6 Å thick central slices in the XY plane of the raw reconstruction and the reconstructions with a 3D Wiener filter ( = 1, 2 and 3) and a 3D Bragg peak filter. **f-j**, Zoomed views of four regions in (**a-e**), respectively. While the result with the = 1 Wiener filter is nosier, the atomic positions with the = 2 and 3 Wiener filter and the 3D Bragg peak filter are consistent. Due to the convolution effect in applying the 3D Wiener and 3D Bragg peak filters, the boundary of the images in (**c-e**), especially in (**e**), is not well defined. By using a 3D shape (i.e. a tight support) determined from the EST reconstruction, a clear 3D boundary of the Pt nanoparticle can be obtained (see Fig. 1d).

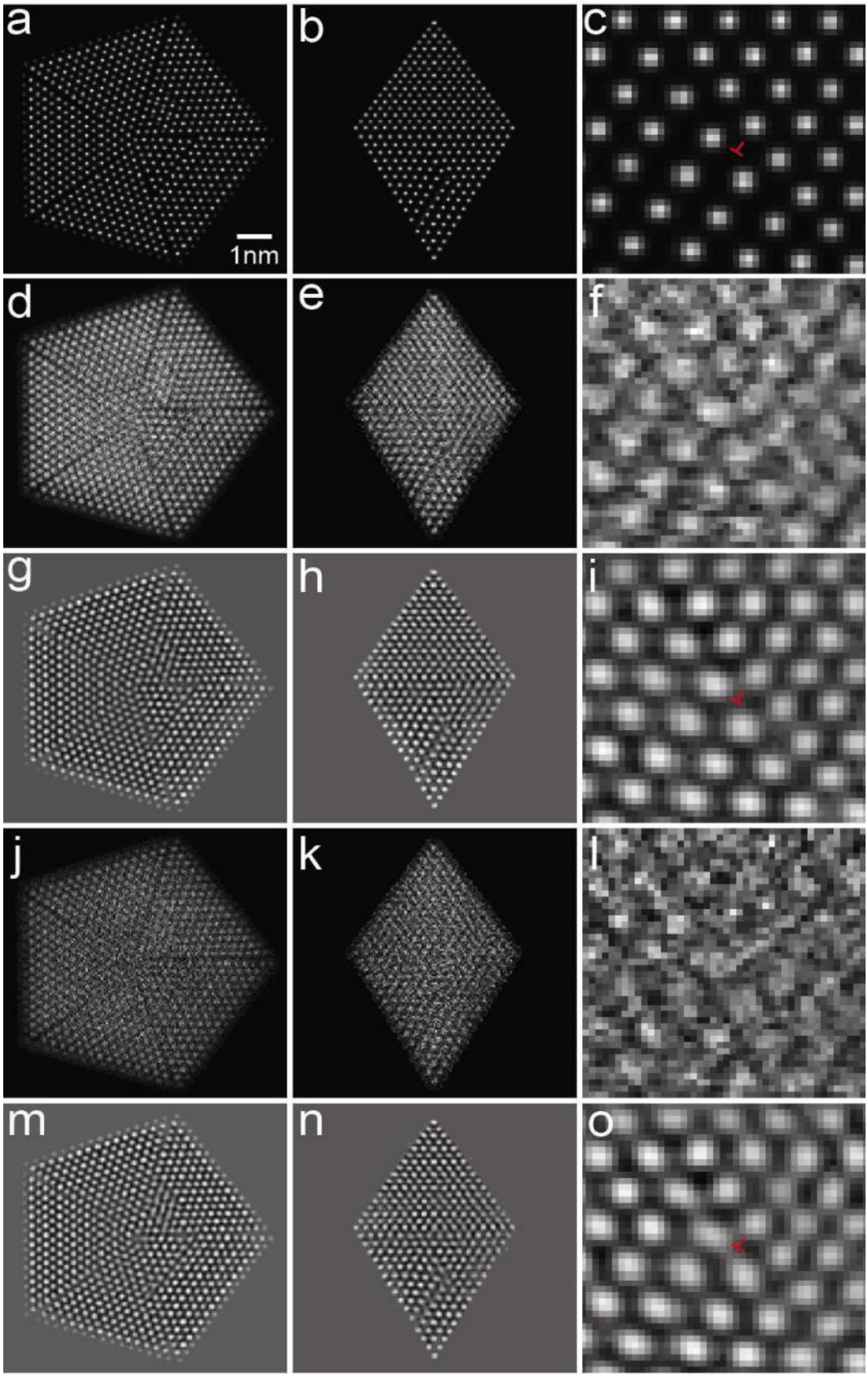
a
b
c
1nm
d
e
f
g
h
i
j
k
l
m
n
o

**Supplementary Figure 6.** EST reconstruction of a simulated decahedral Pt nanoparticle using multislice STEM calculations. The 7.3×7.0×4.5 $nm^3$ Pt particle consists of a total of 4015 atoms with edge and screw dislocations. A tilt series of 63 projections with a tilt range of ±72.6° and equal slope increments was obtained using multislice STEM calculations[36] (Supplementary Fig. 8). To simulate experimental conditions, the tilt angles were continuously shifted from 0° to 0.5° over the process of the tilt series. Two levels of Poisson noise were added to the projections of the tilt series with a total electron dose of $2.52\times10^5$ e/$Å^2$ and $5.67\times10^4$, corresponding to $R_{noise}$ (Methods) of 10% and 20%, respectively. **a** and **b,** Two 2.6 Å thick central slices of the Coulomb potential of the simulated nanoparticle in the XY and ZX planes, where the Z-axis is the beam direction. **c,** Zoomed view of an edge dislocation in a 2.6 Å thick slice, obtained after a -90° rotation of the nanoparticle around the Y-axis and another -35.3° rotation around the Z axis. **d, e** and **f**, The corresponding 2.6 Å thick slices and the edge dislocation reconstructed from 63 multislice STEM projections with $R_{noise}$ = 10%. **g, h** and **i**, The corresponding 2.6 Å thick slices and the edge dislocation with $R_{noise}$ = 10%, after applying a 3D Bragg peak filter with an optimized threshold of 5% of the highest intensity {111} Bragg peak. Compared to the threshold (10%) used for the experimental Pt nanoparticle, a smaller threshold (5%) here is because cross-streak noise in this reconstruction is lower than that in the experimental data (Supplementary Fig. 4). The clear boundary of the reconstructed nanoparticle is due to the multiplication of the filtered structure with a 3D shape obtained from the EST reconstruction. **j, k** and **l**, The corresponding 2.6 Å thick slices and the edge dislocation from the raw reconstruction with $R_{noise}$ = 20%. **m, n** and **o**, The corresponding 2.6 Å thick slices and the edge dislocation with $R_{noise}$ = 20% after applying a 3D Bragg peak filter

with a threshold of

5%. After applying the 3D Bragg peak filter, all the atoms in the 3D reconstructions (**g**, **h**, **m** and **n**) are visible. The 3D core structure of the edge dislocation is observed at atomic resolution (**i** and **o**) and consistent with the model (**c**). In our numerical simulations, we have also found that 3D Fourier filtering is more accurate than the 2D case.

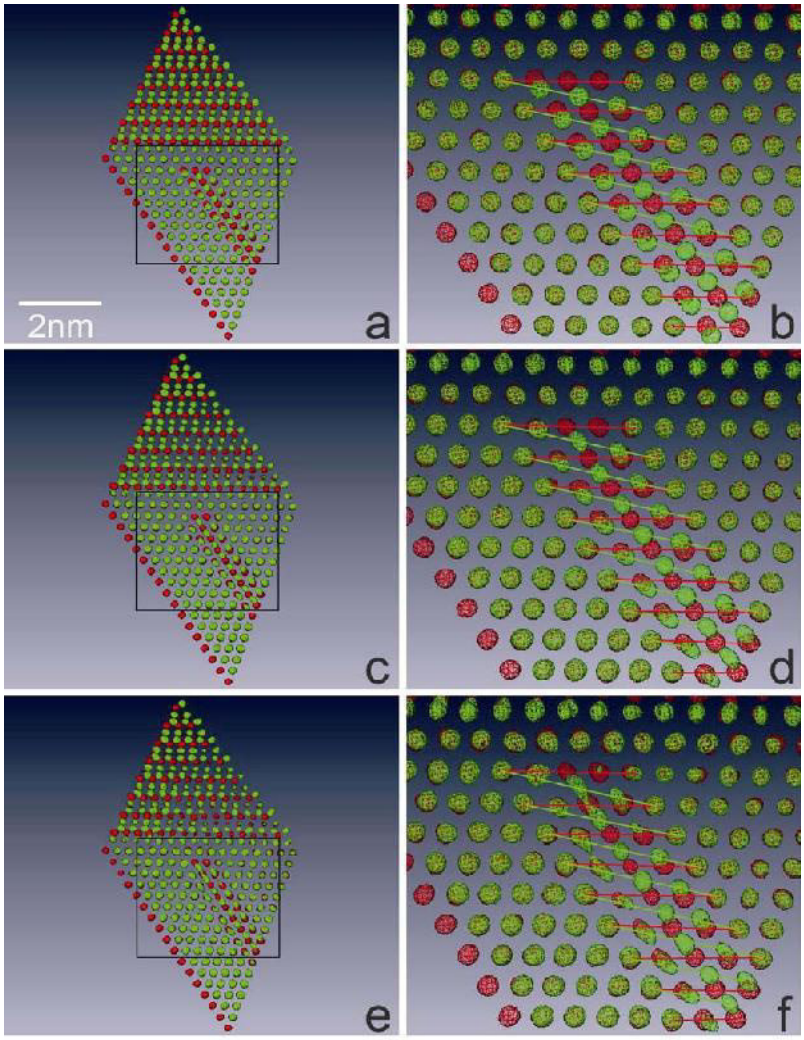


**Supplementary Figure 7.** Multislice simulations on 3D imaging of a screw dislocation at atomic resolution. **a**, A 4.8 Å thick slice (about two atomic layers) of the simulated Pt nanoparticle. **b**, Zoomed view of a screw dislocation, in which the zigzag pattern, a characteristic feature of a screw dislocation, is visible. **c** and **d**, The corresponding 4.8 Å thick slice and zoomed view of the screw dislocation after applying a 3D Bragg peak filter to the EST reconstruction with $R_{noise}$ = 10%. **e** and **f**, The corresponding 4.8 Å thick slice and zoomed view of the screw dislocation after applying a 3D Bragg peak filter to the reconstruction with $R_{noise}$ = 20%. In both reconstructions, the 3D core structure of the screw dislocation is visible (**d** and **f**) and consistent with the model (**b**).

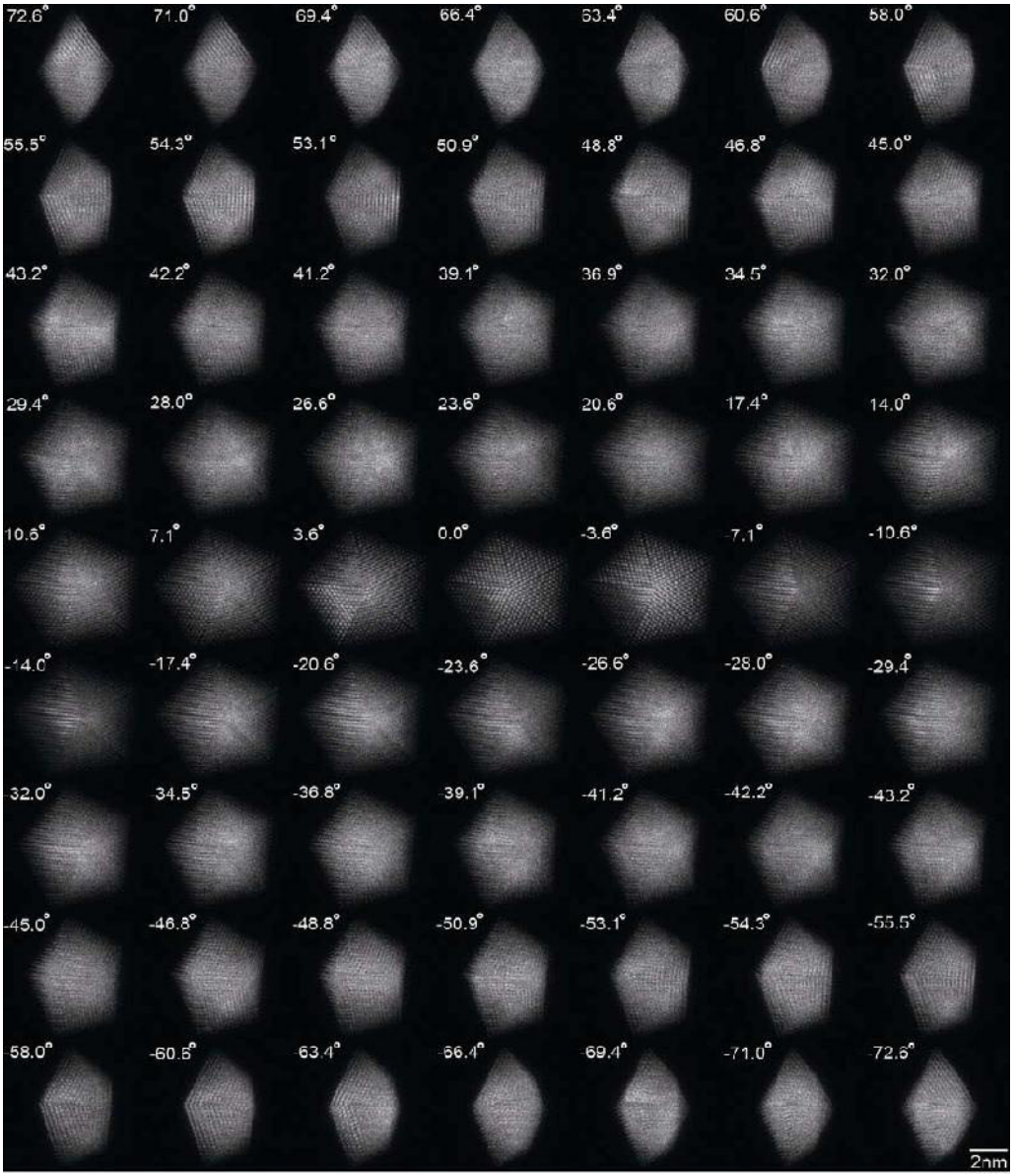


**Supplementary Figure 8.** Multislice calculations of the simulated Pt nanoparticle, shown in Supplementary Fig. 6 (energy: 200 keV, spherical aberration: 1.2 mm, illumination semi-angle: 10.7 mrad, defocus: 54.86 nm, detector inner and outer angles: 35.2 and 212.3 mrad, pixel size: 0.35 Å). A tilt series of 63 projections was calculated with a tilt range of ±72.6° and equal slope increments. To avoid the zone axis orientations and reduce the non-linear effects, the nanoparticle was rotated by 1° each around the horizontal (X) and tilt (Y) axes. Poisson noise was added to the tilt series with a total electron dose of $5.67\times10^{4}$ e/Å$^{2}$ and $R_{noise}$ = 20%.

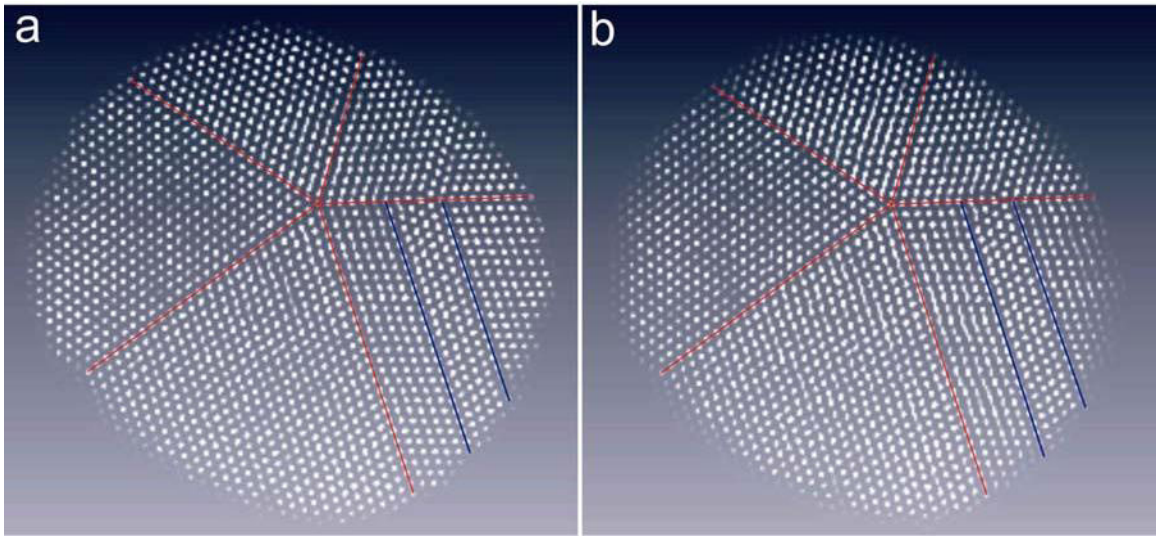


**Supplementary Figure 9**. Grain boundary comparison between experimental (**a**) and calculated (**b**) projections, in which the twin boundaries (red lines) and subgrain boundaries (blue lines) are consistent. (**a**) is the same as Fig. 2a, and (b) was obtained by reprojecting the EST reconstruction in the XY plane. 2D Bragg peak filtering was applied to the projections to better visualize the twin and subgrain boundaries. Some of the differences between (**a**) and (**b**) are caused by 2D Bragg peak filtering, which, according to our numerical simulations, is not as accurate as the 3D case.

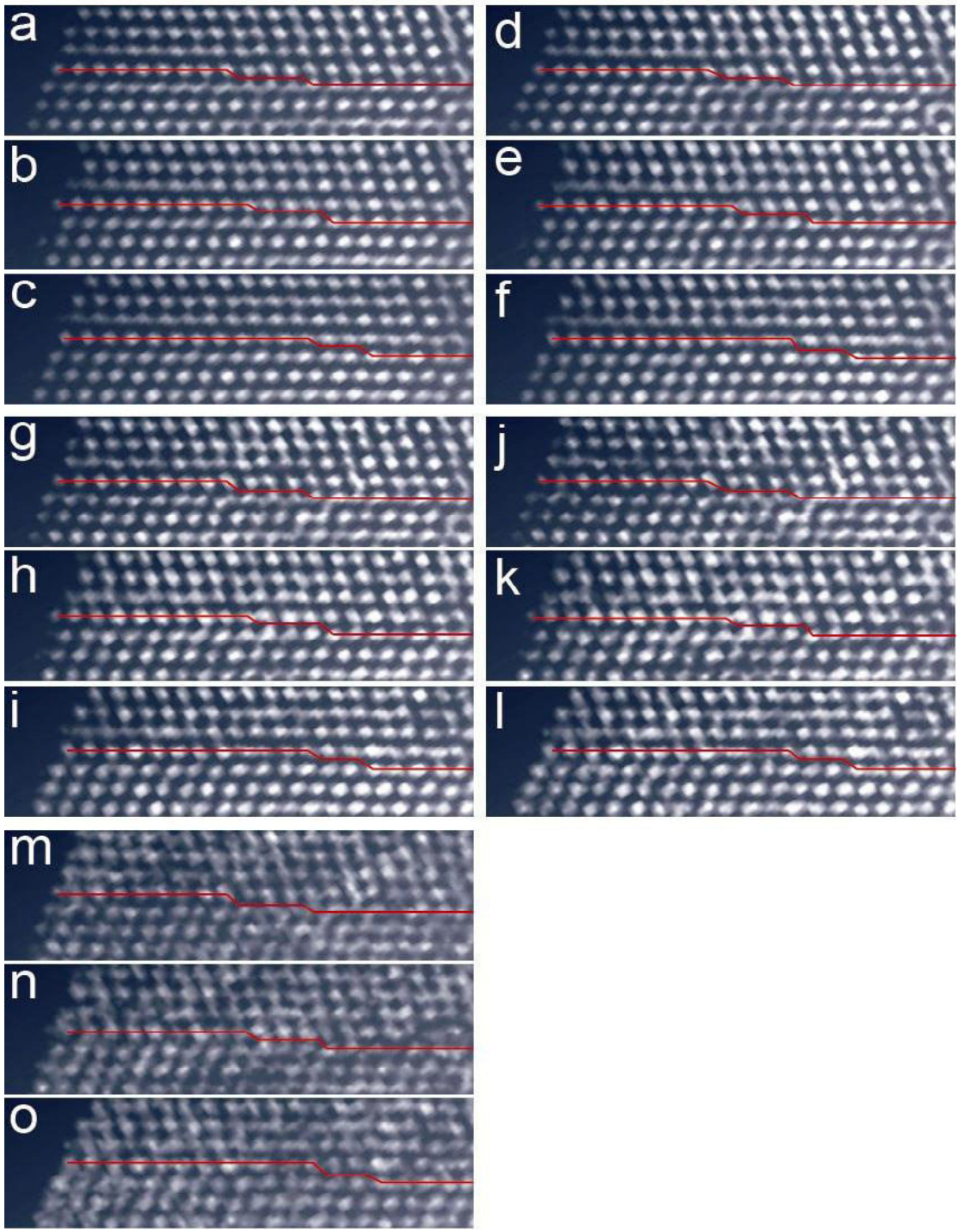


**Supplementary Figure 10. a-c**, Three consecutive 2.6 Å thick slices across a twin boundary after 3D Bragg peak filtering with a threshold of 10% (i.e. the same as Fig. 2c-e). The same three consecutive slices after 3D Bragg peak filtering with a threshold of 7% (**d-f**), and after 3D Wiener filtering with  = 1 (**g-i**),  = 2 (**j-l**) and  = 3 (**m-o**). The atomic steps at the twin boundary (red lines) are consistent in all five cases.

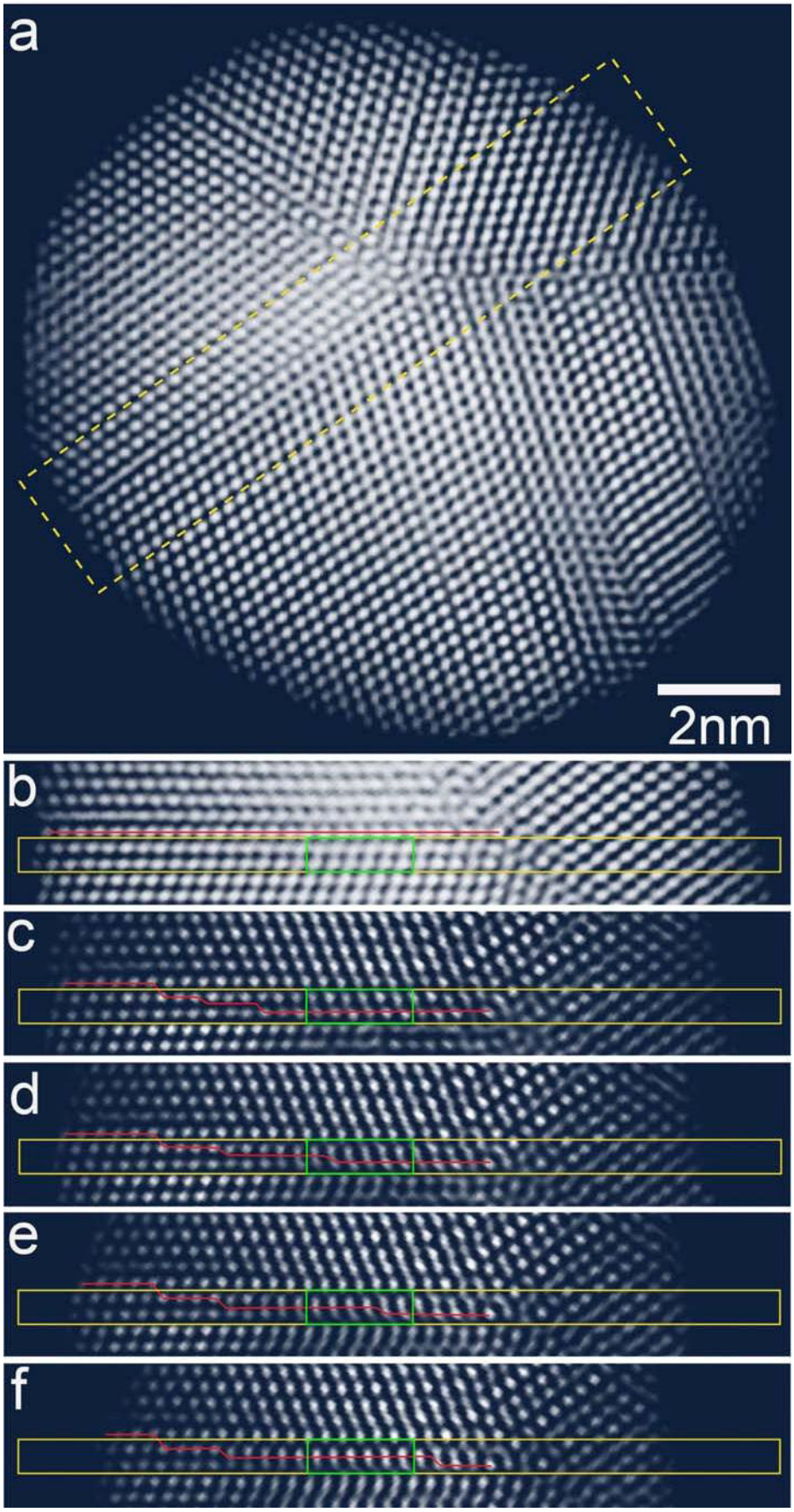
a
2nm
b
c
d
e
f

**Supplementary Figure 11.** Association of a screw dislocation with atomic steps at a twin boundary. **a**, 3D volume rendering of the reconstructed Pt nanoparticle viewed along the [110] (Z-axis) direction. **b**, Zoomed view of the screw dislocation and twin boundary. The yellow rectangle shows a 5.3 Å thick slice in the $(\bar{1}11)$ plane (left grain) used for generating Fig. 4. The green rectangle indicates the location of the screw dislocation in the [110] direction, and the twin boundary is labeled with a red line. **c-f**, Four consecutive internal slices each with 2.6 Å thick. The positions of the atoms inside the green rectangles gradually change in (**c-f**) suggesting that the screw dislocation is associated with atomic steps at the twin boundary. The association of the dislocations with the atomic steps at the boundary accounts for the strain relaxation for the multiply-twinned particle. Note that the twin boundary inside the green rectangles (*i.e*. the screw dislocation area) is not well defined.

# CHAPTER 4

# 3D Imaging of a Phase Object from a Single Sample Orientation Using an Optical Laser

Chien-Chun Chen,[1] Huaidong Jiang,[2] Lu Rong,[1] Sara Salha,[1] Rui Xu,[1] Thomas G. Mason,[1,3] and Jianwei Miao[1*]

[1]*Department of Physics & Astronomy and California NanoSystems Institute, University of California, Los Angeles, CA 90095, USA.*

[2]*State Key Laboratory of Crystal Materials, Shandong University, Jinan 250100, People's Republic of China.*

[3]*Department of Chemistry and Biochemistry, University of California, Los Angeles, CA 90095, USA.*

Published in *Phys. Rev. B*, **84**, 224104 (2011).

**Ankylography is a new 3D imaging technique which under certain circumstances enables to reconstruct a 3D object from a single sample orientation. Here, we provide matrix rank analysis to explain the principle of ankylography. We then present an ankylography experiment on a microscale phase object using an optical laser. Coherent diffraction patterns were acquired from the phase object with a planar CCD detector and were projected onto a spherical shell. The 3D structure of the object was directly reconstructed from the spherical diffraction pattern. This work may potentially open a door of a new method for the 3D imaging of phase objects in the visible light region. Finally, the extension of ankylography to more complicated and larger objects is suggested.**

# Introduction

Lens-based microscopy such as light, phase-contrast, fluorescence, confocal, x-ray and electron microscopy has made important contributions to a broad range of fields in both physical and life sciences. In 1999, a new form of microscopy was developed, termed lenless imaging or coherent diffraction microscopy [1], in which the diffraction pattern of a non-crystalline specimen was first measured and then directly phased to obtain an image. The well-known phase problem was solved by oversampling the diffraction intensity [2,3] in combination of iterative algorithms [4-7]. Using synchrotron radiation, high harmonic generation, soft x-ray laser sources and free electron lasers, coherent diffraction imaging (CDI) has been applied to conduct structure studies of a wide range of samples in materials science, nanoscience and biology [8-31]. To perform 3D CDI, a sequence of 2D diffraction patterns has to be acquired by either tilting a sample at multiple orientations or using many identical copies of the sample [9,12,15,25,30]. In some application, however, it is very

desirable to obtain the 3D structure of an object without the requirement of sample tilting or identical copies of the object. To achieve this challenging goal, ankylography has recently been developed [32], which under certain circumstances allows for 3D imaging of an object from a single sample orientation. Subsequently, two imaging methods somewhat related to ankylography have been demonstrated. The first is super-resolution biomolecular crystallography [33], which under some conditions can determine the high-resolution 3D structure of macromolecules from low-resolution data. The other is discrete tomography [34], which enables the 3D atomic reconstruction of a small crystalline nanoparticle by only using two projections, combined with prior knowledge of the particle's lattice structure. Compared to conventional 3D structure and imaging methodology, these three methods are mathematically ill-posted problems, but represent a new and important direction in structural determination – retrieving 3D structural information from a portion of Fourier magnitudes or coefficients.

In this paper, we first provide a matrix rank analysis to explain why ankylography under certain circumstances can be used to determine the 3D structure from a single sample orientation. We then perform the ankylographic reconstruction of a phase object using an optical laser. There are thee significant implications of this experiment. First, it extends ankylography to the 3D imaging of phase objects in the visible light region that is currently dominated by confocal microscopy. Second, compared to the previous result that is somewhat controversial due to the use of a transparent sample on an opaque substrate [35,36], this work represents the first ankylographic reconstruction of a phase object on a transparent substrate. Finally, using X-ray free electron lasers, ankylography may be applied to determine the 3D structure of certain classes of samples without the need of identical copies.

# Matrix Rank Analysis of Ankylography

We provide a matrix rank analysis to explain why ankylography under certain circumstances can be used to determine the 3D structure from a single view. Let us assume that a coherent wave illuminates a 3D real object, $\rho(x,y,z)$. The far-field diffracted wave, $F(k_x,k_y,k_z)$, is oversampled on a spherical shell. We separate $F(k_x,k_y,k_z)$ into cosines and sines,

$$
\begin{aligned}
&F(k_x,k_y,k_z) = A_{k_x,k_y,k_z}\exp(i\phi_{k_x,k_y,k_z}) \\
&= \sum_{x=-M}^{M}\sum_{y=-M}^{M}\sum_{z=-M}^{M}\rho(x,y,z)\exp\left[\frac{-2\pi i(k_x\cdot x+k_y\cdot y+k_z\cdot z)}{2N+1}\right] \\
&\Rightarrow \begin{cases} A_{k_x,k_y,k_z}\cos(\phi_{k_x,k_y,k_z}) = \sum_{x=-M}^{M}\sum_{y=-M}^{M}\sum_{z=-M}^{M}\rho(x,y,z)\cos\left[\frac{2\pi(k_x\cdot x+k_y\cdot y+k_z\cdot z)}{2N+1}\right] \\ iA_{k_x,k_y,k_z}\sin(\phi_{k_x,k_y,k_z}) = -i\sum_{x=-M}^{M}\sum_{y=-M}^{M}\sum_{z=-M}^{M}\rho(x,y,z)\sin\left[\frac{2\pi(k_x\cdot x+k_y\cdot y+k_z\cdot z)}{2N+1}\right] \end{cases} \quad (1) \\
&\forall\, k_x,k_y,k_z: \quad \left(N-\frac{1}{2}\right)^2 \le k_x^2+k_y^2+(k_z+N)^2 < \left(N+\frac{1}{2}\right)^2
\end{aligned}
$$

where $(2M+1)^3$ is the size of the 3D object (*i.e.* support size), $(2N+1)^3$ is the size of the reciprocal-space array in which the two hemi-spherical shells are located, $A_{k_x,k_y,k_z}$ and $\phi_{k_x,k_y,k_z}$ are the magnitudes and phases of $F(k_x,k_y,k_z)$, and the diffraction angle is assumed to be 90°. In Eq. (1), we chose the spherical shell to be one voxel thick, which is a reasonable assumption as the thickness of the spherical shell is determined by the experimental parameters such as the energy resolution, divergence and convergence angle of the incident beam. Note that Eq. (1) is not the discrete Fourier transform relation as the reciprocal-space vectors on the spherical shell ($k_x$, $k_y$, $k_z$) are not independent, but related via $(N-1/2)^2 \le k_x^2+k_y^2+(k_z+N)^2 < (N+1/2)^2$. We rewrite Eq. (1) into the matrix form,

$$BX = A$$

$$B = \begin{pmatrix} \cos\left[\frac{2\pi(k_{x_1}\cdot x_1 + k_{y_1}\cdot y_1 + k_{z_1}\cdot z_1)}{2N+1}\right] & \cdots & \cos\left[\frac{2\pi(k_{x_1}\cdot x_{(2M+1)^3} + k_{y_1}\cdot y_{(2M+1)^3} + k_{z_1}\cdot z_{(2M+1)^3})}{2N+1}\right] \\ \vdots & \vdots & \vdots \\ \cos\left[\frac{2\pi(k_{x_L}\cdot x_1 + k_{y_L}\cdot y_1 + k_{z_L}\cdot z_1)}{2N+1}\right] & \cdots & \cos\left[\frac{2\pi(k_{x_L}\cdot x_{(2M+1)^3} + k_{y_L}\cdot y_{(2M+1)^3} + k_{z_L}\cdot z_{(2M+1)^3})}{2N+1}\right] \\ 1 & \cdots & 1 \\ -\sin\left[\frac{2\pi(k_{x_1}\cdot x_1 + k_{y_1}\cdot y_1 + k_{z_1}\cdot z_1)}{2N+1}\right] & \cdots & -\sin\left[\frac{2\pi(k_{x_1}\cdot x_{(2M+1)^3} + k_{y_1}\cdot y_{(2M+1)^3} + k_{z_1}\cdot z_{(2M+1)^3})}{2N+1}\right] \\ \vdots & \vdots & \vdots \\ -\sin\left[\frac{2\pi(k_{x_L}\cdot x_1 + k_{y_L}\cdot y_1 + k_{z_L}\cdot z_1)}{2N+1}\right] & \cdots & -\sin\left[\frac{2\pi(k_{x_L}\cdot x_{(2M+1)^3} + k_{y_L}\cdot y_{(2M+1)^3} + k_{z_L}\cdot z_{(2M+1)^3})}{2N+1}\right] \end{pmatrix} \quad (2)$$

$$X = \begin{pmatrix} \rho(x_1, y_1, z_1) \\ \vdots \\ \rho(x_{(2M+1)^3}, y_{(2M+1)^3}, z_{(2M+1)^3}) \end{pmatrix} \qquad A = \begin{pmatrix} A_1\cos(\phi_1) \\ \vdots \\ A_L\cos(\phi_L) \\ A_0 \\ A_1\sin(\phi_1) \\ \vdots \\ A_L\sin(\phi_L) \end{pmatrix}$$

$$\forall\, k_{x_i}, k_{y_i}, k_{z_i} \quad x_i, y_i, k_i \in [-N, N]: \quad \left(N-\frac{1}{2}\right)^2 \le k_{x_i}^2 + k_{y_i}^2 + (k_{z_i}+N)^2 < \left(N+\frac{1}{2}\right)^2$$

where $B$, $X$ and $A$ are $(2L+1)\times(2M+1)^3$, $(2M+1)^3\times 1$ and $(2L+1)\times 1$ matrices, respectively, $(2L+1)$ is the number of non-centro-symmetrical grid points on the spherical shell, and the row of (1 … 1) in matrix $B$ and $A_0$ in matrix $A$ correspond to the centro-voxel. To facilitate our quantitative analysis, we generate two new matrices $B'$ and $X'$ by expanding $B$ and padding zeros to $X$,

$$B' = \begin{pmatrix} \cos\left[\dfrac{2\pi(k_{x_1}\cdot x_1 + k_{y_1}\cdot y_1 + k_{z_1}\cdot z_1)}{2N+1}\right] & \cdots & \cdots\cos\left[\dfrac{2\pi(k_{x_1}\cdot x_{2L+1} + k_{y_1}\cdot y_{2L+1} + k_{z_1}\cdot z_{2L+1})}{2N+1}\right] \\ \vdots & B & \vdots \\ -\sin\left[\dfrac{2\pi(k_{x_L}\cdot x_1 + k_{y_L}\cdot y_1 + k_{z_L}\cdot z_1)}{2N+1}\right]\cdots & & \cdots -\sin\left[\dfrac{2\pi(k_{x_L}\cdot x_{2L+1} + k_{y_L}\cdot y_{2L+1} + k_{z_L}\cdot z_{2L+1})}{2N+1}\right] \end{pmatrix}$$

$$X' = \begin{pmatrix} 0 \\ \vdots \\ 0 \\ X \\ 0 \\ \vdots \\ 0 \end{pmatrix} \qquad \textit{such that} \qquad B'X' = A \tag{3}$$

where $B'$ is defined as the sampling matrix, $B'$ and $X'$ are $(2L+1)\times(2L+1)$ and $(2L+1)\times 1$ matrices, respectively. Mathematically, Eq. (3) is equivalent to Eq. (2).

To give some specific examples on the matrix rank analysis, we first calculated the rank of $B'$ by using a 7×7×7 voxel array (*i.e.* $M = 3$). The spherical shell is embedded inside a 17×17×17 voxel array (*i.e.* $N = 8$). The number of non-centro-symmetrical grid points on the spherical shell of 1 voxel thick is 393 (*i.e.* $L = 392$) with the oversampling degree ($O_d$ = 1.14), defined as[32]

$$O_d = \frac{\textit{Number of voxels within one of the spherical shell}}{\textit{Number of voxels within the support}}. \tag{4}$$

The rank of $B'$ is determined to be 785 (*i.e.* matrix $B'$ has full rank) with tolerance of $10^{-3}$. In this case, the number of unknown variables of the 3D object is 343 (*i.e.* $7^3$), and the number of unknown variables for the phases in Eq. (3) is 392. Therefore the total number of unknown variables is smaller than the rank of $B'$ , suggesting that the 3D object can in principle be obtained by solving Eq. (3). We also calculate the rank of $B'$ for a 14×14×14 voxel object with $O_d$ = 2.06. In this case, the rank of $B'$ is larger than the number of unknown variables with tolerance of $10^{-6}$, but smaller with tolerance of $10^{-3}$. When $O_d$ is

increased to be ~4.0, the rank of B (with tolerance of $10^{-3}$) is larger than the number of unknown variables. The matrix rank analysis suggests that when the object array is larger, the tolerance becomes smaller in order to maintain full rank of the sampling matrix and the ankylographic reconstruction becomes more challenging without additional constraints and information, which is consistent with the numerical simulation results [32]. To facilitate interested readers to conduct ankylographic reconstructions, several Matlab source codes have been posted on a public website and can be freely downloaded to test this method [37].

# Ankylography Experiment and Reconstruction

Next, we present an ankylographic experiment on a phase object with an optical laser. Figure 1 shows the schematic layout of the experimental setup. An optical laser with $\lambda$ = 543 nm was collimated by a compound lens system, consisting of two converging lenses and producing a parallel beam with a diameter of ~200 μm. An aperture was placed 15 mm upstream of the sample to block the unwanted scattering from the lenses. The object to be imaged in 3D is a dielectric phase pattern made up of non-absorbing SU-8 epoxy photoresist that had been cross linked by using an Ultratech XLS stepper. Figure 2(a) shows a differential-interference-contrast (DIC) microscope image of the phase object, which consists of a dense arrangement of four alphabet letters (WWWA) in close proximity; as fabricated, the letters have about 1 μm thickness. As the sample is a weak phase object, the phase shift within a 3D resolution volume can be approximately represented as

$$e^{i\varphi(x,y,z)} \approx 1 + i\varphi(x,y,z), \qquad (5)$$

The Fourier transform of the term "1" in Eq. (5) is concentrated at the center voxel in reciprocal space (*i.e.* the direct wave) and is blocked by a beamstop, while the Fourier modulus of $i\varphi(x,y,z)$ is centro-symmetrical. Compared to conventional 2D exit wave

where the phase shift may not be small after propagating through a whole object, $\phi(x, y, z)$ represents the phase shift within 1 voxel in ankylography and is thus small for a weak phase object. The sample was supported on a silicon nitride membrane of 100 nm thick. To increase the depth of the sample along the Z (beam) axis, the silicon nitride membrane was tilted about 45° relative to the incident beam. Coherent diffraction patterns were recorded by a liquid-nitrogen-cooled CCD camera with 1340×1300 pixels and a pixel size of 20 m × 20 m, positioned at a distance of 31.5 mm from the sample. The distance between the sample and the detector could not be further reduced due to the geometry of the commercial CCD camera. A beamstop was positioned in front of the CCD camera to block the direct beam.

To obtain coherent diffraction patterns at highest possible resolution, we moved the CCD camera both horizontally and vertically, and measured a diffraction pattern at each of the four quadrants. The four diffraction patterns were tiled together to form a high spatial resolution (HSR) pattern. To ensure the missing center confined within the centro-speckle [38], we took an additional low spatial resolution (LSR) diffraction pattern by moving the CCD camera further downstream at a distance of 108 mm to the sample. To remove the background scattering and readout noise of the CCD, we measured two sets of diffraction patterns at each position with the sample in and out of the laser beam. Table 1 shows the experimental parameters used to measure the diffraction patterns. The HSR and LSR diffraction patterns after background subtraction are shown in Figs. 2(b) and (c), which were combined to assemble a diffraction pattern of 2001×2001 pixels with a small missing center.

Because the CCD is a 2D planar detector, the assembled diffraction pattern has to be projected onto a spherical surface. As the solid angle subtended by each CCD pixel varies with the diffraction angle, the diffraction intensity was normalized by

$$I_N\left(k_x^d, k_y^d\right) = \frac{\Delta\Omega(0,0)}{\Delta\Omega\left(k_x^d, k_y^d\right)} I_M\left(k_x^d, k_y^d\right) \qquad (6)$$

where $I_N(k_x^d, k_y^d)$ and $I_M(k_x^d, k_y^d)$ are the normalized and measured diffraction intensities, $(k_x^d, k_y^d)$ is the pixel position of the planar CCD, $\Delta\Omega(0,0)$ and $\Delta\Omega\left(k_x^d, k_y^d\right)$ are the solid angle subtended by the central pixel and pixel $(k_x^d, k_y^d)$, respectively. $\Delta\Omega(k_x^d, k_y^d)$ is determined by,

$$\Delta\Omega\left(k_x^d, k_y^d\right) = R\int_{k_x^d-\delta/2}^{k_x^d+\delta/2}\int_{k_y^d-\delta/2}^{k_y^d+\delta/2} \frac{dk_x^d dk_y^d}{[(k_x^d)^2 + (k_y^d)^2 + R^2]^{3/2}} \qquad (7)$$

where $R$ is the distance from the sample to the CCD camera and $\delta$ is the CCD pixel size.

The normalized diffraction intensity was then projected on the spherical surface on a Cartesian grid. To perform more accurate interpolation, we first located the Cartesian grid points, $(k_x^c, k_y^c, k_z^c)$, within a spherical shell of 1 voxel thick and then projected the grid points onto the planar CCD by

$$k_x^{d\prime} = R\frac{k_x^c}{R - k_z^c} \qquad k_y^{d\prime} = R\frac{k_y^c}{R - k_z^c}. \qquad (8)$$

where $(k_x^{d\prime}, k_y^{d\prime})$ are the X and Y coordinates on the detector plane and are not necessary an integer number of pixels. We calculated $I_N(k_x^{d\prime}, k_y^{d\prime})$ by using the Spline interpolation with the neighboring pixels, and then assigned $I_N(k_x^{d\prime}, k_y^{d\prime})$ to the Cartesian grid point, $I_N(k_x^c, k_y^c, k_z^c)$. Figure 2(d) shows the diffraction intensity distributed within two spherical shells on a 3D Cartesian grid. The centro-symmetry of the diffraction intensity is because the sample is a weak phase object (Eq. (5)). The array size of the 3D Cartesian grid is 1691×1691×491 voxels with a diffraction angle of 32.3°.

To perform the ankylographic reconstruction, we first roughly estimated a loose support for the phase object. The algorithm was then iterated back and forth between real and reciprocal space with a random phase set as an initial input. In real space, the electron density outside the support and the negative density inside the support were slowly pushed close to zero [6]. In reciprocal space, the Fourier magnitudes within the spherical shell were updated with the measure ones while other Fourier magnitudes remained unchanged in each iteration. The convergence of the algorithm was monitored by an $R_{sphere}$ defined as,

$$R_{sphere} = \frac{\sum \left| |F^{M}_{sphere}(\vec{k})| - |F^{C}_{sphere}(\vec{k})| \right|}{\sum |F^{M}_{sphere}(\vec{k})|} \qquad (9)$$

where $|F^{M}_{sphere}(\vec{k})|$ and $|F^{C}_{sphere}(\vec{k})|$ are the measured and calculated Fourier modulus within a spherical shell. Compared to the phase retrieval in coherent diffraction imaging, the convergence speed in ankylographic reconstruction is slower and more iteration is required. To make ankylographic reconstructions more efficient, we performed ~10 independent reconstructions each with a random phase seed. After 5000 iteration, we chose the best 3D reconstruction with the smallest $R_{sphere}$. By convolving the reconstruction with a Gaussian filter and choosing a cutoff value, we determined an updated support. After running another 500 iteration, we reconstructed a 3D object from which a final tight support was determined. Figure 3 shows the supports used from loose to tight during ankylographic reconstructions. The oversampling degree ($O_d$) for the final support is 2062 [32]. A large oversampling degree in the reconstruction is because the final support used is very tight. After another 5000 iteration, a final 3D reconstruction was obtained with $R_{sphere}$ = 0.36. According to our experience, a correct, tight support is important to the ankylographic reconstruction. In addition, a larger oversampling degree ($O_d$) is also helpful in the reconstruction of experimental data.

# Results

The resolution in ankylography is determined by $d_t = \lambda / \sin(2\theta)$ and $d_l = \lambda / (2\sin^2\theta)$, where $d_t$ and $d_l$ represent the transverse and longitudinal resolution (*i.e.* perpendicular and parallel to the incident beam), $\lambda$ is the wavelength and $2\theta$ is the diffraction angle. In this experiment, the transverse and longitudinal resolution was estimated to be ~1.0 μm and ~3.5 μm, respectively. Figures 4(a-c) show 3 projections of the final reconstruction along the X, Y, and Z (beam) axes. Based on the achieved resolution of ~1.0 μm along the X and Y axes and ~3.5 μm along the Z axis, we determined the projection length of the object in the X, Y and Z axes to be ~19 μm, ~23 μm and ~23, respectively. Figures 4(d-f) show the central slices of the final reconstruction along the X, Y and Z axes. According to Figs. 4(d) and (e), the thickness of the object is about 1 – 2 voxels which is consistent with the known value. Figure 5(a) shows iso-surface renderings of the ankylographic reconstruction. The orientation of the phase object relative to the beam is illustrated in Fig. 5(a). To verify the reconstruction, we tilted the reconstruction to the same orientation (Fig. 5b) as the DIC image (Fig. 2a). The 3 letters "WWW" are clearly visible and consistent with the DIC image, while the letter "A" is a bit too small to be resolved in the reconstruction. To further quantify the ankylographic reconstruction, we did a line scan across the reconstruction (Fig. 5b). The blue curve in Fig. 5(c) shows the reconstructed density of the phase object, which is in reasonably good agreement with the DIC curve (the red curve). The discrepancy is because ankylography produces a quantitative reconstruction of the phase object, but not the DIC image.

# Conclusion

In this article, we first present matrix rank analysis to explain why ankylography under certain circumstances enables to reconstruct a 3D object from a single spherical diffraction pattern. We then present an ankylography experiment on a phase object with an optical laser. Coherent diffraction patterns were measured from the phase object, projected onto a spherical surface and directly phased to obtain the 3D structure of the object. Transverse and longitudinal resolutions of 1.0 μm and 3.5 μm, respectively, were achieved in the experiment. While the resolution is currently limited by the experimental set-up (*i.e.* the distance between the sample and the CCD could not be set smaller than 31.5 mm due to the geometry of the commercial CCD camera), the ultimate resolution is set by the wavelength of the incident beam. Compared to conventional coherent diffraction imaging [8-31], the ankylographic reconstruction not only requires a tight support with a large oversampling degree, but also becomes more challenging for larger objects. In order to apply ankylography to large objects, three different approaches are envisioned. First, our numerical simulations suggest that increasing the thickness of the spherical shell can distinctly improve the ankylographic reconstruction of large objects. Experimentally, this may be realized by using an incident wave with an energy bandwidth, coupled with an energy-resolved detector [39]. Second, more real-space constraints can facilitate the ankylographic reconstruction of large objects. One way to achieve this is to position a 3D object with a known structure close to an unknown one, which is somewhat related to molecular replacement and holography [40]. Based on our numerical simulations, the combination of the known part and a spherical diffraction pattern is more effective to reconstruct a large 3D object. Finally, by acquiring several spherical diffraction patterns at different sample orientations with each having a large oversampling degree, our numerical

simulations indicate that ankylography can be extended to larger objects. Compared to conventional tomography, the number of projections required in ankylography will likely be smaller due to the utilization of spherical diffraction patterns.

# References


1. J. Miao, P. Charalambous, J. Kirz and D. Sayre, Nature **400**, 342 (1999).
2. D. Sayre, Acta Crystallogr. **5**, 843 (1952).
3. J. Miao, D. Sayre and H.N. Chapman, J. Opt. Soc. Am. A**. A** 15, 1662 (1998).
4. J. R. Fienup, Appl. Opt. **21**, 2758 ((1982)
5. V. Elser, Acta Cryst. A **59**, 201 (2003).
6. C. C. Chen, J. Miao, C. W. Wang, and T. K. Lee, Phys. Rev. B **76**, 064113 (2007).
7. S. Marchesini, J. Opt. Soc. Am. A **24**, 3289 (2007).
8. I. K. Robinson, I. A. Vartanyants, G. J. Williams, M. A. Pfeifer, and J. A. Pitney, Phys. Rev. Lett. **87**, 195505 (2001).
9. J. Miao, T. Ishikawa, B. Johnson, E. H. Anderson, B. Lai, and K. O. Hodgson, Phys. Rev. Lett. **89**, 088303 (2002).
10. J. Miao, K. O. Hodgson, T. Ishikawa, C. A. Larabell, M. A. LeGros, and Y. Nishino, Proc. Natl. Acad. Sci. USA, **100**, 110 (2003).
11. D. Shapiro et al., Proc. Natl. Acad. Sci. USA **102**, 15343 (2005).
12. M. A. Pfeifer, G. J. Williams, I. A. Vartanyants, R. Harder, and I. K. Robinson, Nature **442**, 63 (2006).
13. H. M. Quiney, A. G. Peele, Z. Cai, D. Paterson, and K. A. Nugent, Nature Phys. **2** 101 (2006).
14. H. N. Chapman et al., Nature Phys. **2**, 839 (2006).

15. J. Miao, C. C. Chen, C. Song, Y. Nishino, Y. Kohmura, T. Ishikawa, D. R. Johnson, T. K. Lee, and S. H. Risbud, Phys. Rev. Lett. **97**, 215503 (2006).

16. G. J. Williams, H. M. Quiney, B. B. Dhal, C. Q. Tran, K. A. Nugent, A. G. Peele, D. Paterson, and M. D. de Jonge, Phys. Rev. Lett. **97**, 025506 (2006)

17. J. M. Rodenburg, A. C. Hurst, A. G. Cullis, B. R. Dobson, F. Pfeiffer, O. Bunk, C. David, K. Jefimovs, and I. Johnson, Phys. Rev. Lett. **98**, 034801 (2007).

18. R. L. Sandberg et al., Phys. Rev. Lett. **99**, 098103 (2007).

19. B. Abbey, K. A. Nugent, G. J. Williams, J. N. Clark, A. G. Peele, M. A. Pfeifer, M. de Jonge, and I. McNulty, Nature Phys. **4**, 394-398 (2008).

20. H. Jiang, D. R. Johnson, C. Song, B. Amirbekian, Y. Kohmura, Y. Nishino, Y. Takahashi, T. Ishikawa, and J. Miao, Phys. Rev. Lett. **100**, 038103 (2008).

21. P. Thibault, M. Dierolf, A. Menzel, O. Bunk, C. David, and F. Pfeiffer , Science, **321**, 379 (2008).

22. C. Song et al., Phys. Rev. Lett. **101,** 158101 (2008).

23. R. L. Sandberg et al., Proc. Natl. Acad. Sci. USA, **105**, 24 (2008).

24. A. Barty et al., Nature Photon, **2**, 415 (2008).

25. Y. Nishino, Y. Takahashi, N. Imamoto, T. Ishikawa, and K. Maeshima, Phys. Rev. Lett. **102**, 018101 (2009).

26. X. Huang et al., Phys. Rev. Lett. 103, 198101 (2009).

27. E. Lima, L. Wiegart, P. Pernot, M. Howells, J. Timmins, F. Zontone, and A. Madsen, Phys. Rev. Lett. **103**, 198102 (2009).

28. A. Ravasio et al., Phys. Rev. Lett. **103**, 028104 (2009).

29. A. P. Mancuso et al., Phys. Rev. Lett. **102**, 035502 (2009).

30. H. Jiang et al., Proc. Natl. Acad. Sci. USA, **107**, 11234 (2010).

31. M. M. Seibert et al., Nature **470**, 78 (2011).

32. K. S. Raines, S. Salha, R. L. Sandberg, H. Jiang, J. A. Rodríguez, B. P. Fahimian, H. C. Kapteyn, J. Du, and J. Miao, Nature **463**, 214 (2010).

33. G. F. Schroder, M. Levitt and A. T. Brunger. Nature **464**, 1218 (2010).

34. S. V. Aert, K. J. Batenburg, M. D. Rossell, R. Erni, and G. V. Tendeloo, Nature **470**, 374 (2011).

35. P. Thibault, Preprint at (http://arXiv.org/abs/0909.1643v1) (2009).

36. J. Miao, Preprint at (http://arXiv.org/abs/0909.3500v1) (2009).

37. www.physics.ucla.edu/research/imaging/Ankylography.

38. J. Miao, Y. Nishino, Y. Kohmura, B. Johnson, C. Song, S. H. Risbud, and T. Ishikawa, Phys. Rev. Lett. **95**, 085503 (2005).

39. A. S. Hoover *et al*., J. Radioanal. Nucl. Chem. **282**, 227 (2009).

40. M. G. Rossman and D. M. Blow, Acta Cryst. **15**, 24 (1962).

41. S. Eisebitt, J. Lüning, W. F. Schlotter, M. Lörgen, O. Hellwig, W. Eberhardt, and J. Stöhr, Nature **432**, 885 (2004).

| | | Sample (exposure time × number of frames) | Background (exposure time × number of frames) | Distance from sample to CCD |
|---|---|---|---|---|
| HSR | Center | 0.17 s × 1000 | 0.17 s × 500 | 3.15 cm |
| | Lower-Left | 0.18 s × 1000 | 0.18 s × 500 | |
| | Lower-Right | 0.45 s × 1000 | 0.45 s × 500 | |
| | Upper-Left | 0.2 s × 1000 | 0.2 s × 500 | |
| | Upper-Right | 0.16 s × 1000 | 0.16 s × 500 | |
| LSR | | 0.25 s ×1000 | 0.25 s × 500 | 10.80 cm |

**Tab. 1** Experimental parameters used to measure the high spatial resolution (HSR) and low spatial resolution (LSR) diffraction patterns with an optical laser.

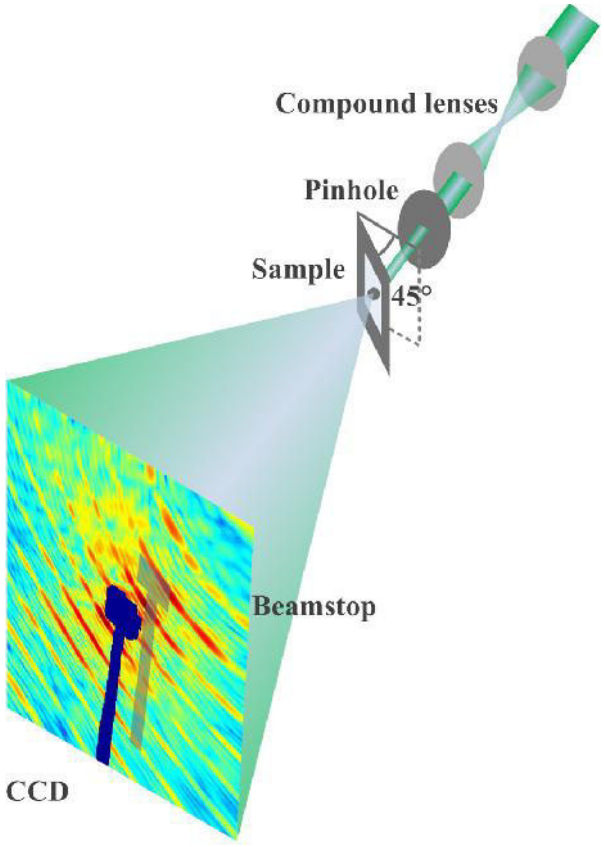


**Figure 1** Schematic layout of the experimental set-up. A compound lens system, consisting of two converging lenses, was used to collimate the incident laser beam with a wavelength of 543 nm. An aperture was placed 15 mm upstream of the sample to block the unwanted scattering from the lenses. A phase object made up of SU-8 epoxy photoresist was supported on a silicon nitride membrane of 100 nm thick. To increase the depth of the sample along the beam axis, the silicon nitride membrane was tilted about 45° relative to the incident beam. Coherent diffraction patterns were recorded by a liquid-nitrogen-cooled CCD camera with 1340×1300 pixels and a pixel size of 20 m×20 m, placed at a distance of 31.5 mm from the sample. A beamstop was positioned in front of the CCD camera to block the direct beam.

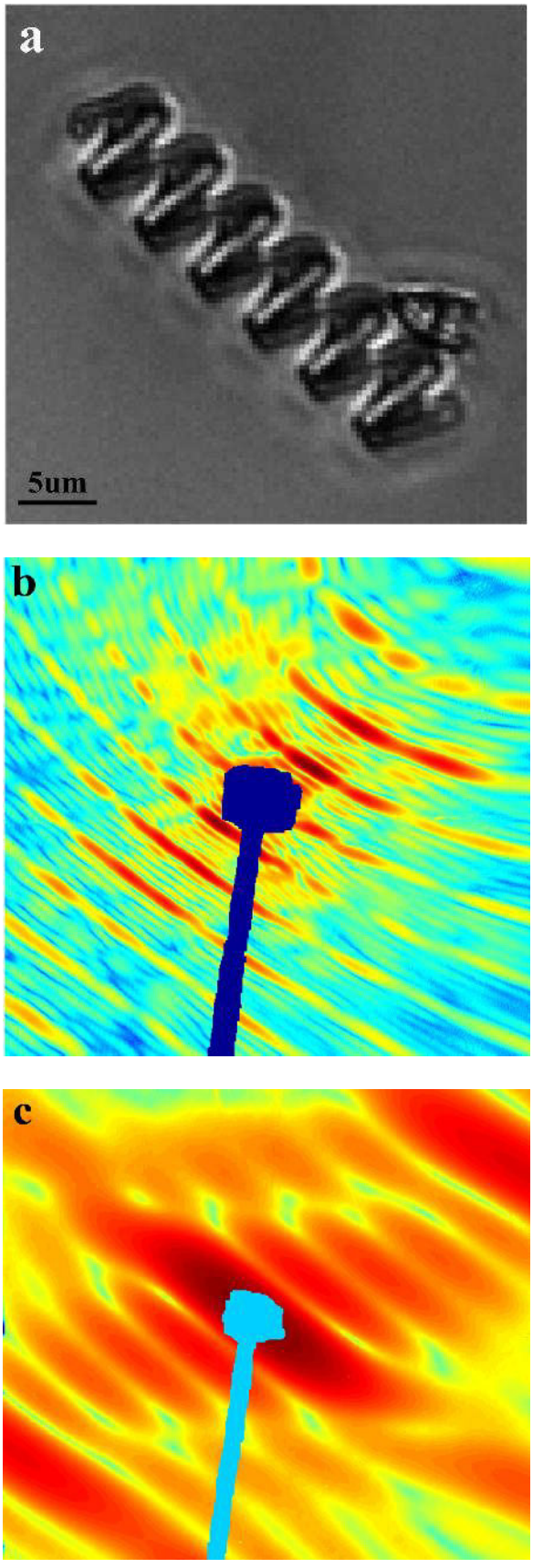
a
5um
b
c

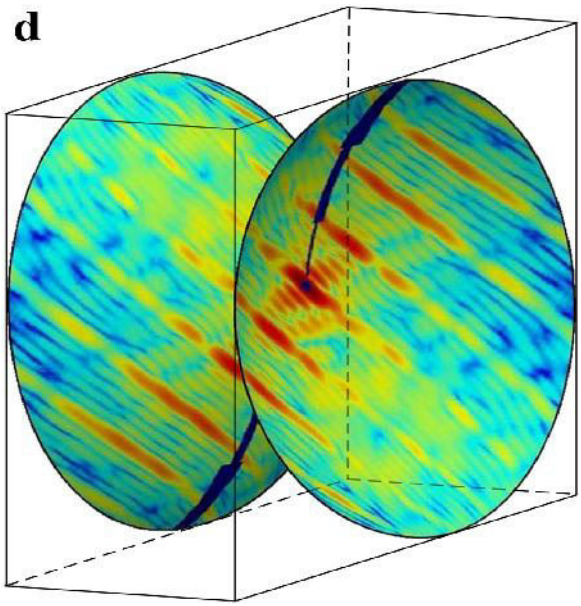


**Figure 2** (**a**) DIC microscope image of the phase object, consisting of four alphabet letters (WWWA). (**b**), (**c**) The high and low spatial resolution diffraction patterns acquired by a planar CCD detector. The low spatial resolution pattern was used to reduce the missing center. (**d**) Two spherical diffraction patterns on a 3D Cartesian grid. The centro-symmetry of the two spherical patterns is because the sample is a weak phase object. The size of the 3D array is 1691×1691×491 voxels with a diffraction angle of 32.3°.

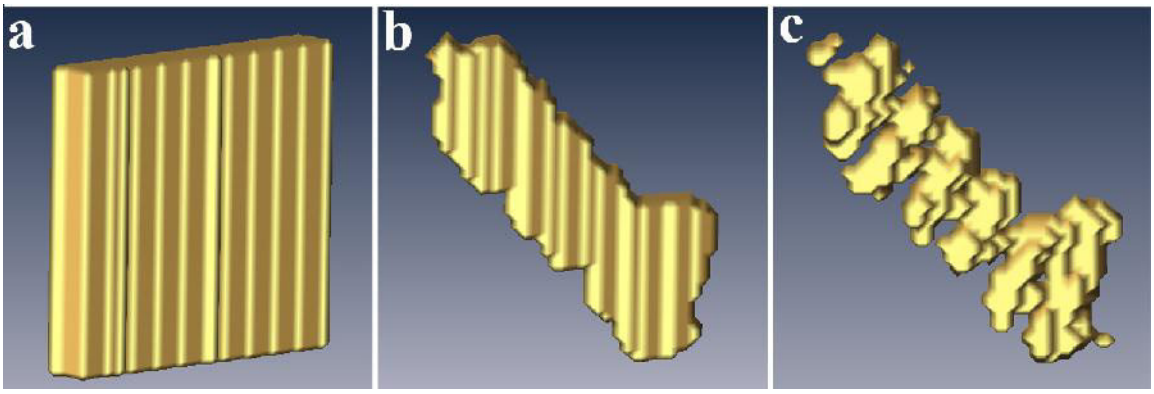


**Figure 3** Supports from loose (**a**) to tight (**c**) used for the ankylographic reconstructions. (**a**) Initial loose support. (**b**) Updated support, (**c**) Final tight support.

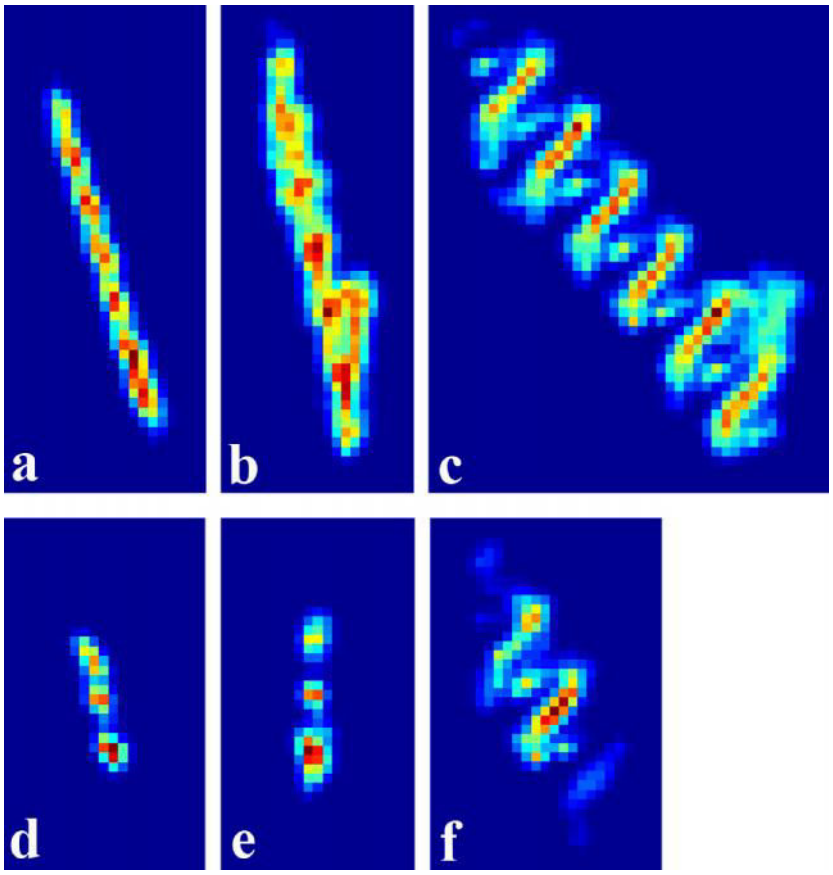


**Figure 4** . (**a-c**) Three projections of the final reconstruction along the X, Y, and Z (beam) axes. Based on the achieved resolution of ~1.0 μm along the X and Y axes and ~3.5 μm along the Z axis, the projection length of the object in the X, Y and Z axes was estimated to be ~19 μm, ~23 μm and ~23, respectively. (**d-f**) Central slices of the final reconstruction along the X, Y and Z axes. The thickness of the phase object is about 1 – 2 voxels which is consistent with the known value.

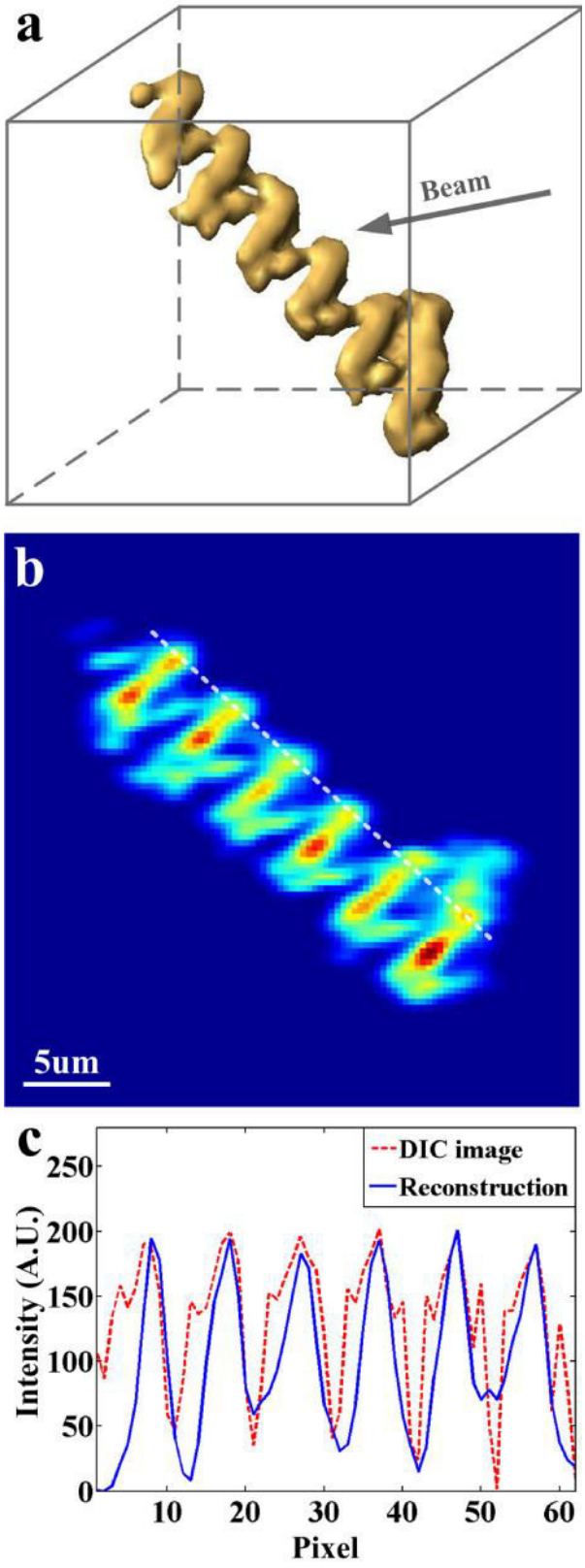


**Figure 5** (**a**) Iso-surface rendering of the ankylographic reconstruction of the phase object where the relative orientation of the incident beam to the object position is illustrated. (**b**)

The reconstruction is tilted to the same orientation as the DIC image (Fig. 2a). Although the resolution of the reconstruction is lower than the DIC image, the two images are in good agreement. (**c**) Line scans across the reconstruction and the DIC image. The two curves agree reasonably well. The discrepancy is ankylography produces a quantitative reconstruction of the phase object, but not the DIC image.